Development of a 6DOF Nonlinear Simulation Model Enhanced with Fine Tuning Procedures

BY

Hou In (Edmond) Leong

Submitted to the graduate degree program in Aerospace Engineering and the Graduate Faculty of the University of Kansas in partial fulfillment of the requirements for the degree of Master of Science.

_____

Dr. Richard Colgren, Chairperson

Committee Members: _____

Dr. David Downing

_____

Dr. Shahriar Keshmiri

Date Defended: Nov. 19, 2008

The Thesis Committee of Hou In (Edmond) Leong certifies that this is the approved version of the following thesis:

Development of a 6DOF Nonlinear Simulation Model Enhanced with Fine Tuning Procedures

_____

Dr. Richard Colgren, Chairperson

Committee Members: _____

Dr. David Downing

_____

Dr. Shahriar Keshmiri

Date Approved: _____Dec. 8, 2008_____

Abstract

This document describes the study of a conventional parametric modeling technique to be used for aircraft simulation in support of an Unmanned Aerial Vehicle (UAV) development program for glacial ice research funded by the National Science Foundation (NSF). A low cost, one-third scale Yak-54 RC plane is used as the research platform throughout this evaluation process.

Using this geometric based modeling method, the aerodynamic derivatives are generated and are used to develop two state space linear models for both longitudinal and lateral dynamics so that the eigenvalue analysis can be performed. Parameter identification flight tests are conducted to identify the true open loop dynamics of the Yak-54, and the results are then used to evaluate the accuracy of the analysis results.

A six-degrees of freedom (6DOF) nonlinear model is also developed using the derivative values, and its validity is investigated with the flight test data. The validation results reveal estimation errors in some of the predicted derivative values. A derivative tuning procedure is then introduced to refine the aircraft dynamics for each mode. The final results demonstrate that the derivative tuning technique is capable of improving the accuracy of the 6DOF simulation model, which gives very promising performance to duplicate the aircraft dynamics.

Acknowledgement

First of all, I would like to express my great appreciation to Dr. Shahriar Keshmiri for all his support, inspiration, and guidance throughout my work. Your trust and friendship will never be forgotten. Thanks to my team partner, Rylan Jager, for leading me to many American adventures like football and hunting and being my English tutor.

I would like to thank Dr. Hale for giving me this great opportunity to be part of this team that allows me to build up my professional skills on this unprecedented project. Thanks to my adviser, Dr. Colgren, for his extensive review and valuable inputs to the writing of my thesis. Thanks to Dr. Downing for giving me much valuable advice on this research. Thanks to Dr. Lan for being my adviser and fully supporting me in my first year when I first arrived in the US. Thanks also go to Andy Pritchard for his endless patience and love for students like me and for teaching me English slang that I would not learn in school. Your attitude demonstrates the perfect paragon of a passionate aircraft mechanic that I truly admire.

Thanks to all my family for their continuous support, patience, and encouragement thorough my life of adventure, even though I have not been at home at all over the last thirteen years. Finally, I want to express my deep appreciation to my girl friend, Winnie Wu, for her unconditional love and support to me from the other side of the world and her immeasurable patience as she waits for my return. Without her, all of my work would become worthless.

Table of Contents

List of Figures

List of Tables

Nomenclature

Symbol	***Description***	***Units***
A_x	X axis Acceleration	ft/sec^2
A_y	Y axis Acceleration	ft/sec^2
A_z	Z axis Acceleration	ft/sec^2
AR	Aspect Ratio	----
b	Span	ft
c	Chord	ft
$\bar{c}$	Mean geometric chord	ft
C_D	Airplane drag coefficient	----
C_{D_0}	Airplane drag coefficient for zero angle of attack	----
C_{D_1}	Airplane trim drag coefficient	----
C_{D_α}	Variation in the airplane drag coefficient with angle of attack	1/rad
C_{D_u}	Variation in the airplane drag coefficient with dimensionless speed	1/rad
C_l	Airplane rolling moment coefficient	----
C_{l_β}	Variation in the airplane rolling moment coefficient with angle of sideslip	1/rad
$C_{l_{\delta_a}}$	Variation in the airplane rolling moment coefficient with aileron deflection angle	1/rad
$C_{l_{\delta_r}}$	Variation in the airplane rolling moment coefficient with rudder deflection angle	1/rad
C_{l_p}	Variation in the airplane rolling moment coefficient with dimensionless rate of change of roll rate	1/rad

Symbol	***Description***	***Units***
C_{l_r}	Variation in the airplane rolling moment coefficient with dimensionless rate of change of yaw rate	1/rad
C_L	Airplane lift coefficient	----
C_{L_0}	Airplane lift coefficient for zero angle of attack	----
C_{L_1}	Airplane trim lift coefficient	----
C_{L_α}	Variation in the airplane lift coefficient with angle of attack	1/rad
$C_{L_{\dot{\alpha}}}$	Variation in the airplane lift coefficient with dimensionless rate of change of angle of attack	1/rad
$C_{L_{\delta_e}}$	Variation in the airplane lift coefficient with elevator deflection angle	1/rad
C_{L_q}	Variation in the airplane lift coefficient with dimensionless pitch rate	1/rad
C_{L_u}	Variation in the airplane lift coefficient with dimensionless speed	----
C_m	Airplane pitching moment coefficient	----
C_{m_0}	Airplane pitching moment coefficient for zero angle of attack	----
C_{m_1}	Airplane trim pitching moment coefficient	----
C_{m_α}	Variation in the airplane pitching moment coefficient with angle of attack	1/rad
$C_{m_{\dot{\alpha}}}$	Variation in the airplane pitching moment coefficient with dimensionless rate of change of angle of attack	1/rad
C_{m_q}	Variation in the airplane pitching moment coefficient with pitch rate	1/rad

Symbol	***Description***	***Units***
C_{m_u}	Variation in the airplane pitching moment coefficient with dimensionless speed	----
C_{m_T}	Airplane pitching moment due to thrust	----
$C_{m_{T_1}}$	Airplane trim pitching moment due to thrust	----
$C_{m_{T_\alpha}}$	Variation in the airplane pitching moment coefficient due to thrust with angle of attack	1/rad
$C_{m_{T_u}}$	Variation in the airplane pitching moment coefficient due to thrust with dimensionless speed	----
$C_{m_{\delta_e}}$	Variation in the airplane pitching moment coefficient with elevator deflection angle	1/rad
C_n	Airplane yawing moment coefficient	----
C_{n_β}	Variation in the airplane yawing moment coefficient with angle of sideslip	1/rad
$C_{n_{\delta_a}}$	Variation in the airplane yawing moment coefficient with aileron deflection	1/rad
$C_{n_{\delta_r}}$	Variation in the airplane yawing moment coefficient with rudder deflection	1/rad
C_{n_p}	Variation in the airplane yawing moment coefficient with dimensionless rate of change of roll rate	1/rad
C_{n_r}	Variation in the airplane yawing moment coefficient with dimensionless rate of change of yaw rate	1/rad
$C_{n_{T_\beta}}$	Variation in the airplane yawing moment coefficient due to thrust with sideslip angle	1/rad
C_P	Power coefficient	----

Symbol	***Description***	***Units***
C_T	Thrust coefficient	----
C_{Tx_1}	Trim thrust coefficient in the X-axis direction	----
C_{Tx_u}	Variation in the airplane thrust coefficient in the X-axis direction w.r.t. dimensionless speed	----
C_x	Cosine function of variable x	----
C_y	Airplane side force coefficient	----
C_{y_β}	Variation in the airplane side force coefficient with sideslip angle	1/rad
$C_{y_{\delta_a}}$	Variation in the airplane side force coefficient with aileron angle	1/rad
$C_{y_{\delta_r}}$	Variation in the airplane side force coefficient with rudder angle	1/rad
C_{y_p}	Variation in the airplane side force coefficient with dimensionless rate of change of roll rate	1/rad
C_{y_r}	Variation in the airplane side force coefficient with dimensionless rate of change of yaw rate	1/rad
C_θ	Cosine function of the pitch angle	rad
C_ϕ	Cosine function of the bank angle	rad
C_ψ	Cosine function of the heading angle	rad
$C_{\theta/2}$	Cosine function of half of the pitch angle	rad
$C_{\phi/2}$	Cosine function of half of the bank angle	rad
$C_{\psi/2}$	Cosine function of half of the heading angle	rad
d	Propeller diameter	ft
D	Airplane drag	lbs
e	Oswald's efficiency factor	----
$\overline{E}$	Euler Axis	----

Symbol	***Description***	***Units***
E_x, E_y, E_z	Vector components of Euler Axis	----
F_{Ax}, F_{Ay}, F_{Az}	Aerodynamic force components along XYZ axes	----
h	Altitude	ft
g	Acceleration due to gravity	ft/sec^2
I_{xx}, I_{yy}, I_{zz}	Airplane moments of inertia about XYZ axes	slug ft^2
I_{xy}, I_{yz}, I_{xz}	Airplane moments of inertia about XYZ axes	slug ft^2
J	Propeller advance ratio	----
L	Airplane lift	lbs
L_A, M_A, N_A	Aerodynamic moment components about XYZ axes	ft-lbs
L_β	Roll angular acceleration per unit sideslip angle	(rad/sec^2)/rad
L_p	Roll angular acceleration per unit roll rate	1/sec
L_r	Roll angular acceleration per unit yaw rate	1/sec
L_{δ_a}	Roll angular acceleration per unit aileron angle	(rad/sec^2)/rad
L_{δ_r}	Roll angular acceleration per unit rudder angle	(rad/sec^2)/rad
m	Airplane mass	slugs
M	Mach number	----
M_α	Pitch angular acceleration per unit angle of attack	1/sec^2
M_{T_α}	Pitch angular acceleration per unit angle of attack due to thrust	1/sec^2
M_u	Pitch angular acceleration per unit change in speed	(rad/sec^2)/(ft/sec)
M_{T_u}	Pitch angular acceleration per unit change in	(rad/sec^2)/(ft/sec)

Symbol	***Description***	***Units***
	speed due to thrust	
$M_{\dot{\alpha}}$	Pitch angular acceleration per unit rate of change of angle of attack	1/sec
M_q	Pitch angular acceleration per unit pitch rate	1/sec
M_{δ_e}	Pitch angular acceleration per unit elevator angle	$1/sec^2$
n	Propeller rotational speed per second	rev/min
N_β	Yaw angular acceleration per unit sideslip angle	$(rad/sec^2)/rad$
N_{T_β}	Yaw angular acceleration per unit sideslip angle due to thrust	$(rad/sec^2)/rad$
N_p	Yaw angular acceleration per unit roll rate	1/sec
N_r	Yaw angular acceleration per unit yaw rate	1/sec
N_{δ_a}	Yaw angular acceleration per unit aileron deflection angle	$(rad/sec^2)/rad$
N_{δ_r}	Yaw angular acceleration per unit rudder deflection angle	$(rad/sec^2)/rad$
p , q , r	Perturbed values of P, Q and R	rad/sec
P , Q , R	Airplane angular velocity components about XYZ	rad/sec
$\overline{q}$	Dynamic pressure	lbs/ft^2
S	Area	ft^2
S_x	Sine function of variable x	----
S_θ	Sine function of the pitch angle	rad
S_ϕ	Sine function of the bank angle	rad
S_ψ	Sine function of the heading angle	rad

Symbol	***Description***	***Units***
$S_{\theta/2}$	Sine function of half of the pitch angle	rad
$S_{\phi/2}$	Sine function of half of the bank angle	rad
$S_{\psi/2}$	Sine function of half of the heading angle	rad
t	Thickness	ft
t also:	Time	sec
T	Thrust	lbs
u , v , w	Perturbed values of U, V, and W	ft/sec
U , V , W	Components of V_a along XYZ	ft/sec
V_a	True airspeed	ft/sec
V_g	Ground speed	ft/sec
W	Airplane weight	lbs
x_{ac}	Airplane aerodynamic center location along the X axis	ft
x_b, y_b ,z_b	X, Y, Z components in body fixed coordinates	----
x_{cg}	Airplane center of gravity location along the X axis	ft
x_f, y_f ,z_f	X, Y, Z components in Earth fixed coordinates	----
X_α	Forward acceleration per unit angle of attack	$(ft/sec^2)/rad$
X_u	Forward acceleration per unit change in speed	1/sec
X_{T_u}	Forward acceleration per unit change in speed due to thrust	1/sec
X_{δ_e}	Forward acceleration per unit elevator deflection angle	$(ft/sec^2)/rad$
Y_β	Lateral acceleration per unit sideslip angle	$(ft/sec^2)/rad$
Y_p	Lateral acceleration per unit roll rate	$(ft/sec^2)/(rad/sec)$

Symbol	***Description***	***Units***
Y_r	Lateral acceleration per unit yaw rate	$(ft/sec^2)/(rad/sec)$
Y_{δ_a}	Lateral acceleration per unit aileron deflection angle	$(ft/sec^2)/rad$
Y_{δ_r}	Lateral acceleration per unit rudder deflection angle	$(ft/sec^2)/rad$
Z_α	Vertical acceleration per unit angle of attack	$(ft/sec^2)/rad$
Z_u	Vertical acceleration per unit change in speed	$(ft/sec^2)/(ft/sec)$
$Z_{\dot{\alpha}}$	Vertical acceleration per unit rate of change of angle of attack	$(ft/sec^2)/(rad/sec)$
Z_q	Vertical acceleration per unit pitch rate	$(ft/sec^2)/(rad/sec)$
Z_{δ_e}	Vertical acceleration per unit elevator deflection angle	$(ft/sec^2)/rad$

Greek		
α	Angle of attack	deg or rad
$\dot{\alpha}$	Rate of change of angle of attack	rad/sec
β	Angle of sideslip	deg or rad
δ	Control surface deflection angle	deg or rad
Δ	Increment of a parameter	----
θ	Perturbed value of Θ	deg or rad
Θ	Airplane pitch attitude angle	deg or rad
λ	Taper ratio	----
Λ	Sweep angle	deg or rad
ξ	Damping ratio	----
π	3.14	----
ρ_∞	Air density	$slug/ft^3$

Symbol	***Description***	***Units***
τ	Time constant	sec
ϕ	Perturbed value of Φ	deg or rad
Φ	Airplane bank angle	deg or rad
ψ	Perturbed value of Ψ	deg or rad
Ψ	Airplane heading angle	deg or rad
ω_n	Undamped natural frequency	rad/sec
ω_d	Damped natural frequency	rad/sec

Subscripts

a	Aileron
alt	Altitude
body	Body Axis
c/4	Quarter Chord
cg	Center of Gravity
cmd	Command
e	Elevator
ht	Horizontal Tail
max	Maximum
min	Minimum
r	Rudder
r also:	Roll Mode
ref	Reference Area
s	Spiral Mode
ss	Steady State
t	Throttle
vt	Vertical Tail
x, y or z	In the x, y or z direction

Abbreviations

Abbreviation	***Description***
6DOF	Six Degrees of Freedom
ac	Aerodynamic Center
AAA	Advanced Aircraft Analysis
AGL	Above Ground Level
ALT	Altitude
ASL	Above Sea Level
AVL	Athena Vortex Lattice
C.G.	Center of Gravity
CFD	Computational Fluid Dynamics
COESA	Committee on Extension to the Standard Atmosphere
COTS	Commercial Off The Shelf
CReSIS	Center for Remote Sensing of Ice Sheets
DATCOM	Data Compendium
ECEF	Earth-Center Earth-Fixed
ECI	Earth-Centered Inertial
EFBF	Earth-Fixed Body-Fixed
EOM	Equations Of Motion
FADEC	Full Authority Digital Electrical Control
GPS	Global Positioning System
GUI	Graphical User Interface
HIL	Hardware-in-the-loop
IAS	Indicated airspeed
ICAO	International Civil Aviation Organization
IPCC	Intergovernmental Panel on Climate Change
ISO	International Organization for Standardization
KU	The University of Kansas

Abbreviation	***Description***
LAT	Latitude
LON	Longitude
LUT	Look Up Table
MS	Maximum Slope
NACA	National Advisory Committee for Aeronautics
NASA	National Aeronautics and Space Administration
NED	North-East-Down
NOAA	National Oceanic and Atmospheric Administration
NSF	National Science Foundation
PC	Personal Computer
RC	Remote Control
RPM	Rotational Speed Per Minute
SCCS	Standard Cloud Cap Simulation
SIL	Software-in-the-loop
TPR	Transient Peak Ratio
TR	Time Ratio
UAV	Unmanned Aerial Vehicle
WGS	World Geodetic System
w.r.t.	with respect to

1 Introduction

The Department of Aerospace Engineering at the University of Kansas is actively engaged in research that enables the design and operation of advanced Unmanned Aerial Vehicles (UAVs). A prodigious UAV development program, the Meridian UAV, was launched in 2006 in support of the CReSIS (Center for Remote Sensing of Ice Sheets) research program [1]. CReSIS is a science and technology center established by the National Science Foundation (NSF) in response to the ongoing climate change challenges [2].

The design of Meridian UAV [3] [4] features a 26 foot wing span, low wing, V-tail configuration with 1,000 pound take-off weight. It is powered by the Centurion 2.0 diesel engine equipped with the FADEC (Full Authority Digital Electrical Control) system. This multidisciplinary development program not only fortifies the research activity of aircraft design in this department, but also enhances the department's diversity in different fields of research for UAVs' systems, including integration of the propulsion system [5], development of avionics systems [6], test and evaluation of the autopilot system [7], and flight test programs for UAVs [8].

Another essential technology to support the development of a UAV program is an aircraft simulation platform, which would allow rapid development of aircraft modeling and simulations delivered with high fidelity and accuracy. Many available simulation products in the market have been studied and the

results show that none of the existing tools satisfy the requirements to support these simulation activities [7] [9].

This thesis describes a complete process, leading from modeling, simulation, flight testing to validation, for an in-home developed simulation platform. This low cost, high fidelity simulation technique features a six-degrees-of-freedom (6DOF) nonlinear model built on MATLAB/Simlink. The validity of the simulation model is investigated using flight test data, and a derivative tuning technique is introduced to refine the precision of the dynamics model.

2 Modeling and Simulation Development and Evaluation Process

As mentioned in the introduction, a through modeling, simulation, flight testing, and validation process is developed to enable the research of simulation activities. A one-third scale Yak-54 RC plane is chosen as the platform to be developed and tested in this study. The details of each step in this process are presented in this chapter.

2.1 Step 1: Develop Aircraft Dynamics Model

The first step of the process is to choose an appropriate method to estimate the preliminary aerodynamic model of the vehicle. Much literature is available on this subject, but few address modeling details for the aerodynamic derivatives for small UAVs.

Wind tunnel testing [10] can be utilized to determine the derivatives, but it is labor intensive and costly. Computational Fluid Dynamics (CFD) [11] [12] could be an alternative way to determine these parameters. With help from contemporary computational technologies, CFD has been successfully applied to full size aircraft [13] [14]. However, it still requires great effort to develop a good CFD model with high fidelity, and its application to small size UAVs is rare.

Methods for system identification using actual flight test data to identify the stability and control derivatives are widely used today. This subject of

research has been of interest to the Aerospace community for a long time [15]. Two major techniques have been widely studied and are well developed. They are: 1) time domain identification [16], and 2) frequency domain identification [17]. Reference [18] presents results using the time domain identification technique to determine the aerodynamic derivatives for UAVs. Frequency domain methods have also been successfully applied. They are more suitable for helicopters [19] [20] as they require a long flight time (30 seconds to few minutes) to complete a test maneuver, which is difficult for a remote pilot to perform on fixed wing UAVs within limited visual range. To utilize either the time domain or system domain method, many flight tests are required to gather sufficient data for system identification. This has a negative impact on the development program, not only regarding cost and schedule but also because of the risk involved in flight testing.

Another approach not based on flight testing is to use the geometric parametric principle to estimate the derivatives. Although this technique tends to be low fidelity and cannot replace wind tunnel experiments, it provides a rapid method at low cost that allows users to perform a preliminary analysis with some level of confidence. This approach has been successfully applied to several UAV research programs [21] [22]. Reference [23] conducted research similar to work presented in this document; however, only the longitudinal dynamics were studied. In this research, the Advanced Aircraft Analysis (AAA) [24] software using the

conventional parametric method is utilized to estimate the aerodynamic derivatives of the Yak-54 RC airplane.

2.2 Step 2: Mathematics Based Mode Dynamics Analysis

Once the stability and control derivatives are available, a mathematical approach using the state space model can be applied to perform a preliminarily analysis. Various mathematical techniques to develop the state space model are found in textbooks [25] [26] [27]. Herein, the method outlined by Roskam [28] is used. Once the state space model is developed, the eigenvalues of the state space model are calculated. These show the dynamic characteristics of each mode. Through this analysis, users can quickly examine the stability of the vehicle.

2.3 Step 3: Open Loop Dynamics Identification from the Time Domain Response

To evaluate the accuracy of the results from a mathematical approach, the true open loop dynamics of the vehicle need to be determined. For this purpose, a mode identification flight test [29] is performed. The different dynamics modes are excited by using singlet or doublet inputs on different control surfaces. The time domain responses are then analyzed using a data reduction method [29] to estimate the dynamic characteristics of each mode. The final results from flight tests are then compared with the preliminary analysis results given in Step 2.

2.4 Step 4: Development of the 6DOF Nonlinear Model using MATLAB/Simulink

Though the state space model developed in Step 2 can be used for simulation activities, there are many drawbacks to this method. First, this state space model is a simplified linear model. Second, it ignores the coupling effects between longitudinal and lateral dynamics. Third, it uses an Earth-Fixed Body-Fixed (EFBF) coordinate system [28], which does not consider the rotation of the earth. In addition, this model assumes a constant engine power output when it is linearized. Finally, the state space model does not provide full state outputs and thus cannot be used for navigation mode simulation.

A solution to address these concerns is to use a 6DOF nonlinear simulation model. The aerodynamic derivatives from Step 1 are used for the 6DOF model's construction which is hosted on the MATLAB/Simulink platform [30].

2.5 Step 5: Validation and Matching of 6DOF Nonlinear Models and Simulations using Flight Test Data

The accuracy of the 6DOF nonlinear model needs to be validated. Its responses are studied with the flight test data using the side-by-side comparison technique. Through these comparisons, the discrepancies in each mode between the simulation and the flight test data can be clearly seen. A derivative tuning technique is then introduced that allows users to refine the simulation model by

tuning the derivatives that have the greatest impact on that specific dynamic response. In some cases more than one derivative must be adjusted, so iterative procedures are required to tune the values. The new simulation responses are compared with the flight test data during each tuning cycle until a satisfactory result is achieved. This procedure is illustrated in Figure 2-1.

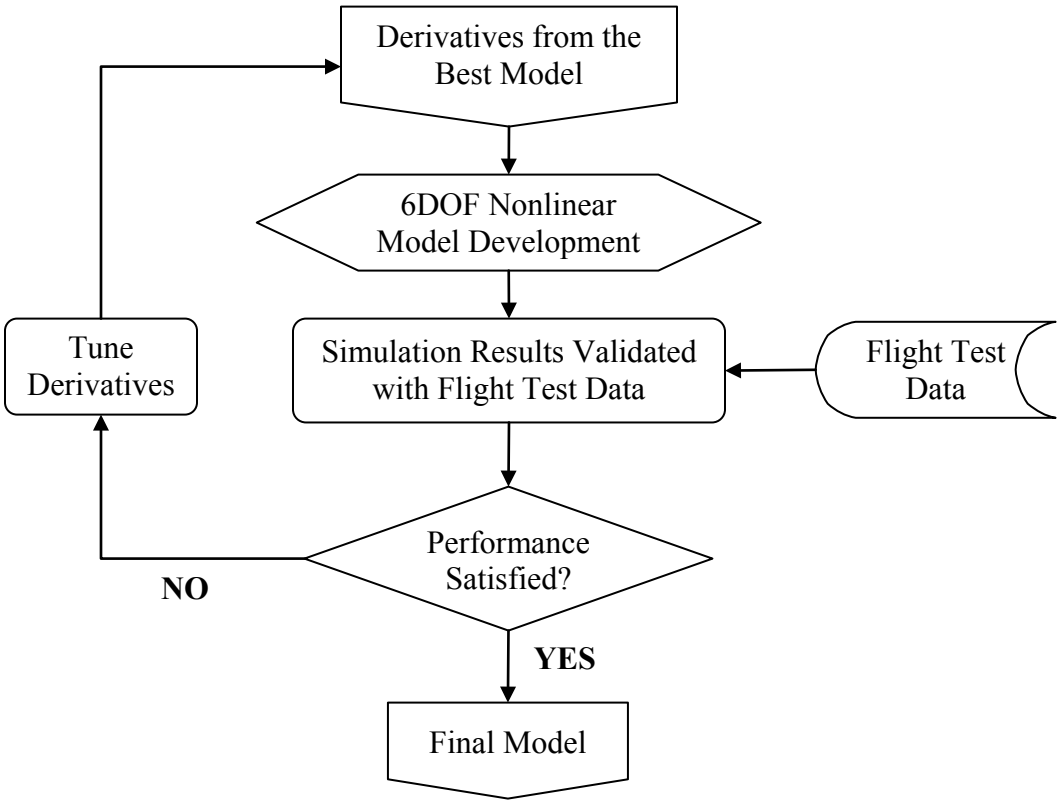

Figure 2-1. Procedure for Tuning Derivatives

3 Yak-54 Aircraft Dynamic Model Development

As previously described, a parametric modeling method is utilized to compute the aerodynamic derivatives for the Yak-54. The derivative values are then used to compose two linear state space models for the longitudinal and the lateral-directional dynamics. In this chapter, the modeling procedures are presented, and the state space model techniques are discussed in detail.

3.1 Advanced Aircraft Analysis Based Simulation Model

AAA [24] is an aircraft design program developed by DAR Corporation [31]. It has a built-in aerodynamic database for different types of aircraft models. This database was created based on the Digital DATCOM [32] program, which is an open source computer program based on the United States Air Force stability and control data compendium (DATCOM) that calculates stability and control derivatives for any given aircraft configuration. The AAA modeling process is mainly based on geometric parameters and the given trim condition. For a given set of aircraft geometry data, AAA extrapolates the aerodynamic derivatives of the aircraft from its historic based database. This provides a rapid method to conduct a preliminary aircraft performance and stability analysis.

The AAA model of the Yak-54 was developed using the geometry data directly measured from the physical aircraft model as listed in Table 3-1 [7]. The trim condition is set at a straight and level flight condition with trim speed and altitude captured from previous flight test data. This trim condition is 1,200 feet

ASL (above sea level) and 0.106 Mach number. The resulting derivatives for this condition are listed in Table 3-2 and Table 3-3.

Table 3-1. Yak-54 Lifting Surfaces

Wing		
Area (S_w)	10.90	ft^2
Span (b_w)	7.90	ft
Mean Aerodynamics Chord ($\bar{c}_w$)	1.45	ft
Aileron Mean Aerodynamic Chord ($\bar{c}_a$)	4.90	in
Quarter Chord Sweep Angle ($\Lambda_{(c/4)_w}$)	-2.00	deg
Aspect Ratio (AR_w)	5.77	~
Taper Ratio (λ_w)	0.46	~
Root Airfoil	NACA 0016	~
Tip Airfoil	NACA 0017	~
Horizontal Tail		
Area (S_{ht})	2.30	ft^2
Span (b_{ht})	3.00	ft
Mean Aerodynamics Chord ($\bar{c}_{ht}$)	9.20	in
Elevator Mean Aerodynamic Chord ($\bar{c}_e$)	4.20	in
Quarter Chord Sweep Angle ($\Lambda_{(c/4)_{ht}}$)	12.60	deg
Aspect Ratio (AR_{ht})	3.91	~
Taper Ratio (λ_{ht})	0.81	~
Root Airfoil	NACA 0015	~
Tip Airfoil	NACA 0012	~
Vertical Tail		
Area (S_{vt})	1.60	ft^2
Span (b_{vt})	1.42	ft
Mean Aerodynamics Chord ($\bar{c}_{vt}$)	14.56	in
Rudder Mean Aerodynamic Chord ($\bar{c}_r$)	8.50	in
Quarter Chord Sweep Angle ($\Lambda_{(c/4)_{vt}}$)	12.70	deg
Aspect Ratio (AR_{vt})	1.25	~
Taper Ratio (λ_{vt})	0.35	~
Root Airfoil	NACA 0009	~
Tip Airfoil	NACA 0010	~

Table 3-2. AAA Dimensionless Stability Derivatives for the Yak-54

Longitudinal Derivatives (rad^{-1})		***Lateral-Directional Derivatives (rad^{-1})***	
C_{D_u}	0.0011	C_{y_β}	-0.3602
C_{D_α}	0.0863	C_{y_p}	0.0085
$C_{T_{x_u}}$	-0.1546	C_{y_r}	0.2507
C_{L_u}	0.0017	C_{l_β}	-0.0266
C_{L_α}	4.5465	C_{l_p}	-0.3819
$C_{L_{\dot{\alpha}}}$	1.8918	C_{l_r}	0.0514
C_{L_q}	5.5046	C_{n_β}	0.1022
C_{m_u}	0.0002	$C_{n_{T_\beta}}$	-0.0045
C_{m_α}	-0.3937	C_{n_p}	-0.0173
$C_{m_{\dot{\alpha}}}$	-4.3787	C_{n_r}	-0.1270
C_{m_q}	-8.0532	$C_{y_{\delta a}}$	0.0000
$C_{m_{T_u}}$	0.0000	$C_{y_{\delta r}}$	0.1929
$C_{m_{T_\alpha}}$	0.0275	$C_{l_{\delta a}}$	0.3490
$C_{D_{\delta e}}$	0.0000	$C_{l_{\delta r}}$	0.0154
$C_{L_{\delta e}}$	0.3792	$C_{n_{\delta a}}$	-0.0088
$C_{m_{\delta e}}$	-0.8778	$C_{n_{\delta r}}$	-0.0996

Table 3-3. AAA Steady State Coefficients for the Yak-54

Steady State Coefficients	
C_{L_1}	0.1470
C_{D_1}	0.0422
$C_{T_{x_1}}$	0.0515
C_{m_1}	0.0001
$C_{m_{T_1}}$	0.0009

3.2 State Space Model Development

A state space modeling technique, as described by Roskam [28], is employed here to make use of the AAA derivatives. In this state space model, the assumption is made to ignore the coupling effect between the longitudinal and lateral dynamics. A linearization technique is applied that assumes the variations in the model's states are linear around the trim point. This simplification makes the state space model valid only when it is close to the trim condition.

3.2.1 Dimensional Stability Derivatives

The dimensional stability derivatives are calculated using the dimensionless stability derivatives listed in Table 3-2. The details of these calculations can be found in Reference [28]. The results are shown in Table 3-4 and Table 3-5 for the longitudinal and lateral-directional models respectively.

To construct the state space model, the moment of inertia is required. The moment of inertia for the Yak-54 is approximated using a component build-up method. The aircraft model is first disassembled into small components: left and right wings, left and right tails, wing and horizontal tail spars, propeller, spinner, engine, batteries, and the Piccolo control unit. Then, each component is weighed individually. The position of each component is measured relative to the engine firewall. These measurements are then used to calculate the moment of inertia of the Yak-54 about the X-axis, Y-axis and Z-axis in the body coordinate system. The Yak-54 is a symmetric aircraft, and the weight distribution on the left and

right wings is almost symmetric, so the moment of inertia about the XZ plane is assumed to be zero. Appendix A displays the spreadsheets used to compute the moment of inertia. The results are summarized in Table 3-6.

Table 3-4. Dimensional Longitudinal Stability Derivatives

X_u	-0.1481	$\left(\frac{ft/\sec^2}{ft/\sec}\right)$	Z_{δ_e}	-77.5853	$\left(\frac{ft/\sec^2}{rad}\right)$
X_{T_u}	-0.0894	$\left(\frac{ft/\sec^2}{ft/\sec}\right)$	M_u	0.0004	$\left(\frac{rad/\sec^2}{ft/\sec}\right)$
X_α	12.4194	$\left(\frac{ft/\sec^2}{rad}\right)$	M_{T_u}	0.0019	$\left(\frac{rad/\sec^2}{ft/\sec}\right)$
X_{δ_e}	0.0	$\left(\frac{ft/\sec^2}{rad}\right)$	M_α	-48.2908	$\left(\frac{rad/\sec^2}{rad}\right)$
Z_u	-0.5121	$\left(\frac{ft/\sec^2}{ft/\sec}\right)$	M_{T_α}	3.3731	$\left(\frac{rad/\sec^2}{rad}\right)$
Z_α	-938.8597	$\left(\frac{ft/\sec^2}{rad}\right)$	$M_{\dot{\alpha}}$	-3.2870	$\left(\frac{rad/\sec^2}{rad/\sec}\right)$
$Z_{\dot{\alpha}}$	-2.3689	$\left(\frac{ft/\sec^2}{rad/\sec}\right)$	M_q	-6.0454	$\left(\frac{rad/\sec^2}{rad/\sec}\right)$
Z_q	-6.8927	$\left(\frac{ft/\sec^2}{rad/\sec}\right)$	M_{δ_e}	-107.6699	$\left(\frac{rad/\sec^2}{rad}\right)$

Table 3-5. Dimensional Lateral-Directional Stability Derivatives

Y_β	-73.6978	$\left(\frac{ft/\sec^2}{rad}\right)$	L_{δ_a}	453.1837	$\left(\frac{rad/\sec^2}{rad}\right)$
Y_p	0.0583	$\left(\frac{ft/\sec^2}{rad/\sec}\right)$	L_{δ_r}	19.9972	$\left(\frac{rad/\sec^2}{rad}\right)$
Y_r	1.7208	$\left(\frac{ft/\sec^2}{rad/\sec}\right)$	N_β	47.6850	$\left(\frac{rad/\sec^2}{rad}\right)$
Y_{δ_a}	0.0	$\left(\frac{ft/\sec^2}{rad}\right)$	N_{T_β}	-2.0996	$\left(\frac{rad/\sec^2}{rad}\right)$
Y_{δ_r}	39.4678	$\left(\frac{ft/\sec^2}{rad}\right)$	N_p	-0.2708	$\left(\frac{rad/\sec^2}{rad/\sec}\right)$
L_β	-34.5407	$\left(\frac{rad/\sec^2}{rad}\right)$	N_r	-1.9879	$\left(\frac{rad/\sec^2}{rad/\sec}\right)$
L_p	-16.6364	$\left(\frac{rad/\sec^2}{rad/\sec}\right)$	N_{δ_a}	-4.1060	$\left(\frac{rad/\sec^2}{rad}\right)$
L_r	2.2391	$\left(\frac{rad/\sec^2}{rad/\sec}\right)$	N_{δ_r}	-46.4719	$\left(\frac{rad/\sec^2}{rad}\right)$

Table 3-6. Vehicle Mass Properties

Symbol	***Description***	***Value***	***Units***
Wgross	Gross weight (full fuel)	28.12	lbs
Wempty	Empty weight (without fuel)	27.18	lbs
IXXb	Moment of Inertia about the X-Axis in Body Frame	1.0886	slug ft^2
IYYb	Moment of Inertia about the Y-Axis in Body Frame	2.1068	slug ft^2
IZZb	Moment of Inertia about the Z-Axis in Body Frame	3.0382	slug ft^2
IXYb	Moment of Inertia about the X-Y Axis in Body Frame	0.00	slug ft^2
IYZb	Moment of Inertia about the Y-Z Axis in Body Frame	0.00	slug ft^2
IXZb	Moment of Inertia about the X-Z Axis in Body Frame	0.00	slug ft^2

3.2.2 Longitudinal State Space Model and Analysis

According to the Roskam method [28], the perturbation equations for longitudinal motion are written as follows:

$$\begin{aligned} \dot{u} &= -g\theta\cos\Theta_1 + X_u u + X_{T_u} u + X_\alpha \alpha + X_{\delta_e}\delta_e \\ U_1\dot{\alpha} - U_1\dot{\theta} &= -g\theta\sin\Theta_1 + Z_u u + Z_\alpha \alpha + Z_{\dot{\alpha}}\dot{\alpha} + Z_q\dot{\theta} + Z_{\delta_e}\delta_e \\ \ddot{\theta} &= M_u u + M_{T_u} u + M_\alpha \alpha + M_{T_\alpha}\alpha + M_{\dot{\alpha}}\dot{\alpha} + M_q\dot{\theta} + M_{\delta_e}\delta_e \end{aligned} \qquad \textbf{Eq. 3-1}$$

For the straight and level flight conditions, $\dot{\theta} = q \;\; and \;\; \ddot{\theta} = \dot{q}$.

Rewriting Eq. 4-1 in state space format, yields:

$$\begin{bmatrix} 1 & 0 & 0 & 0 \\ 0 & (U_1 - Z_{\dot{\alpha}}) & 0 & 0 \\ 0 & -M_{\dot{\alpha}} & 1 & 0 \\ 0 & 0 & 0 & 1 \end{bmatrix} \begin{bmatrix} \dot{u} \\ \dot{\alpha} \\ \dot{q} \\ \dot{\theta} \end{bmatrix} = \begin{bmatrix} X_u + X_{T_u} & X_\alpha & 0 & -g\cos\Theta_1 \\ Z_u & Z_\alpha & U_1 + Z_q & -g\sin\Theta_1 \\ M_u + M_{T_u} & M_\alpha + M_{T_\alpha} & M_q & 0 \\ 0 & 0 & 1 & 0 \end{bmatrix} \begin{bmatrix} u \\ \alpha \\ q \\ \theta \end{bmatrix} + \begin{bmatrix} X_{\delta_e} \\ Z_{\delta_e} \\ M_{\delta_e} \\ 0 \end{bmatrix} \begin{bmatrix} \delta_e \end{bmatrix} \qquad \textbf{Eq. 3-2}$$

Substituting the dimensional derivatives into Eq. 3-2 and performing the necessary matrix algebra, the final longitudinal state space model is obtained:

$$\begin{bmatrix} \dot{u} \\ \dot{\alpha} \\ \dot{q} \\ \dot{\theta} \end{bmatrix} = \begin{bmatrix} -0.2374 & 12.4194 & 0.0000 & -32.1554 \\ -0.0042 & -7.7904 & 0.9232 & -0.0091 \\ 0.0163 & -19.3108 & -9.0798 & 0.0299 \\ 0.0000 & 0.0000 & 1.0000 & 0.0000 \end{bmatrix} \begin{bmatrix} u \\ \alpha \\ q \\ \theta \end{bmatrix} + \begin{bmatrix} 0.0000 \\ -0.6438 \\ -105.5538 \\ 0.0000 \end{bmatrix} \begin{bmatrix} \delta_e \end{bmatrix} \qquad \textbf{Eq. 3-3}$$

Applying eigenvalue analysis to the state space model, the dynamic characteristic of the system can be calculated. The results are presented below.

Table 3-7. AAA Longitudinal Directional Mode Analysis for the Yak-54

Eigenvalues	*Damping Ratio*	*Frequency (rad/sec)*	*Period (sec)*	*Mode*
-0.114 ± 0.248i	0.42	0.27	23.27	Phugoid
-8.440 ± 4.18i	0.90	9.42	0.67	Short Period

The analysis reveals that the Yak-54 model has two complex conjugated roots for its longitudinal dynamics, the Phugoid and short period modes. Both modes exhibit a highly damped response. This is especially true for the short period mode. This result will be validated using flight test data in Chapter 5.

3.2.3 Lateral State Space Model and Analysis

The perturbation equations of motion for the lateral-directional dynamics are shown below, according to Roskam [28]:

$$\begin{aligned} U_1\dot{\beta} + U_1\dot{\psi} &= g\phi\cos\Theta_1 + Y_\beta\beta + Y_p\dot{\phi} + Y_r\dot{\psi} + Y_{\delta_a}\delta_a + Y_{\delta_r}\delta_r \\ \ddot{\phi} - \bar{A}_1\ddot{\psi} &= L_\beta\beta + L_p\dot{\phi} + L_r\dot{\psi} + L_{\delta_a}\delta_a + L_{\delta_r}\delta_r \\ \ddot{\psi} - \bar{B}_1\ddot{\phi} &= N_\beta\beta + N_{T_\beta}\beta + N_p\dot{\phi} + N_r\dot{\psi} + N_{\delta_a}\delta_a + N_{\delta_r}\delta_r \end{aligned} \qquad \textbf{Eq. 3-4}$$

$$where: \quad \bar{A}_1 = \frac{I_{xz}}{I_{xx}} \quad and \quad \bar{B}_1 = \frac{I_{xz}}{I_{zz}}$$

For the straight and level flight conditions, it satisfies: $p = \dot{\phi}$; $\dot{p} = \ddot{\phi}$ *and* $r = \dot{\psi}$; $\dot{r} = \ddot{\psi}$.

Rewriting Eq. 4-4 into a state space format, yields:

$$\begin{bmatrix} 1 & 0 & 0 & -\overline{A}_1 \\ 0 & 1 & 0 & 0 \\ 0 & 0 & U_1 & 0 \\ -\overline{B}_1 & 0 & 0 & 1 \end{bmatrix} \begin{bmatrix} \dot{p} \\ \dot{\phi} \\ \dot{\beta} \\ \dot{r} \end{bmatrix} = \begin{bmatrix} L_p & 0 & L_\beta & L_r \\ 1 & 0 & 0 & 0 \\ Y_p & g\cos\Theta_1 & Y_\beta & (Y_r - U_1) \\ N_p & 0 & (N_\beta + N_{T_\beta}) & N_r \end{bmatrix} \begin{bmatrix} p \\ \phi \\ \beta \\ r \end{bmatrix} + \begin{bmatrix} L_{\delta_a} & L_{\delta_r} \\ 0 & 0 \\ Y_{\delta_a} & Y_{\delta_r} \\ N_{\delta_a} & N_{\delta_r} \end{bmatrix} \begin{bmatrix} \delta_a \\ \delta_r \end{bmatrix} \quad \textbf{Eq. 3-5}$$

Substitute the dimensional derivative values from Table 3-5 into Eq. 4-5. The state space model for the lateral-directional modes can be obtained as follows:

$$\begin{bmatrix} \dot{p} \\ \dot{\phi} \\ \dot{\beta} \\ \dot{r} \end{bmatrix} = \begin{bmatrix} -16.6421 & 0.0000 & -37.3608 & 2.3631 \\ 1.0000 & 0.0000 & 0.0000 & 0.0000 \\ 0.0005 & 0.2722 & -0.6238 & -0.9854 \\ 0.0926 & 0.0000 & 46.4013 & -2.0395 \end{bmatrix} \begin{bmatrix} p \\ \phi \\ \beta \\ r \end{bmatrix} + \begin{bmatrix} 454.0359 & 22.8520 \\ 0.0000 & 0.0000 \\ 0.0000 & 0.3341 \\ -14.0214 & -46.9710 \end{bmatrix} \begin{bmatrix} \delta_a \\ \delta_r \end{bmatrix} \quad \textbf{Eq. 3-6}$$

Using the eigenvalue analysis technique, the mode characteristics of the lateral-directional dynamics can be analyzed and are summarized below.

Table 3-8. AAA Lateral-Directional Mode Analysis for the Yak-54

Eigenvalues	*Damping Ratio*	*Frequency (rad/sec)*	*Period (sec)*	*Time Constant (sec)*	*Mode*
0.0115	----	----	----	86.96	Spiral
-16.7	----	----	----	0.06	Roll
-1.32 ± 6.75i	0.19	6.88	0.91	----	Dutch Roll

The result shows a typical lateral-directional dynamic response for the Yak-54 characterized by a very fast roll mode, a low damped Dutch roll mode, and an unstable spiral mode with a large time constant.

4 Data Analysis Methods

Using the state space model eigenvalue analysis method as described in Section 3.2, the dynamic modes of the aircraft can be estimated. When performing the flight tests, however, the open loop dynamics are described as time domain responses, and thus a data analysis method is needed to identify the dynamic characteristics from these time domain results.

The purpose of this chapter is to introduce a data processing technique that can be used to identify second order system dynamics from a time domain response history. This process is applied to analyze the flight test results as presented in Chapter 5.

4.1 Basic Data Reduction Methods

The data analysis method described here is called the data reduction method [29]. This technique was developed by engineers who work in the field of flight test engineering. This technique is confined to simple methods and is also called "hand-calculations." Much of the material presented in this section is adapted from Reference [29].

Five different basic data reduction techniques are discussed in Reference [29]. Each of them is designed for specific problems. All of them give estimates for the damping ratio and natural frequency for a second order system. These can be used to form a quadratic characteristic equation. Three of the methods are introduced in this chapter. The choice of method is driven by the damping ratio

of the response to be analyzed. Table 4-1 summarizes the applicability of these three methods for different ranges of damping ratio from an oscillatory response.

Table 4-1. Applicability of Different Methods for Determining Damping Ratio

Name of Method	*Range of Applicable Damping Ratio*
Transient Peak Ratio (TPR)	$-0.5 < \xi < 0.5$
Time Ratio (TR)	$0.5 < \xi < 1.2$
Maximum Slope (MS)	$0.5 < \xi < 1.2$

4.2 Transient Peak Ratio Method

The TPR method is one of the most commonly used methods, and is applicable for motions with damping ratios between –0.5 and 0.5. This is commonly seen in Phugoid and Dutch roll mode calculations. Both the basic TPR method and the modified TPR method (that does not require measuring the final steady state value) are shown in Figure 4-1 [29].

The transient peak ratio is first calculated from: $\frac{\Delta X_1}{\Delta X_0} = \frac{\Delta X_2}{\Delta X_1} = \frac{\Delta X_3}{\Delta X_2} = ...$

If the modified TPR method is used, it can be calculated from: $\frac{\Delta X_3}{\Delta X_2} = \frac{\Delta X_2}{\Delta X_1} = ...$

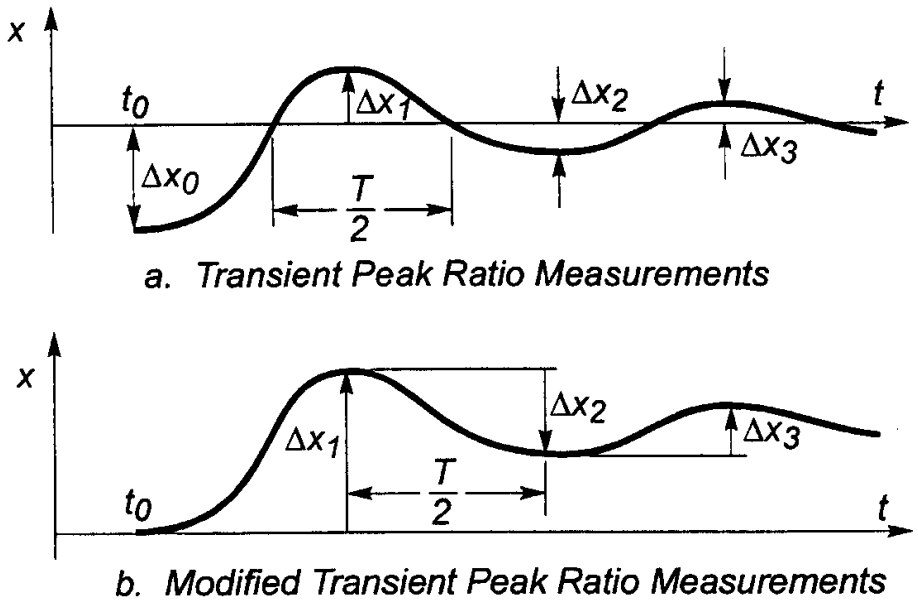

Figure 4-1. Transient Peak Ratio Method

Typically, the ratios are not identical for actual flight test measurements, so the average of the measurements is often used. When the average TPR is measured, the damping ratio can be obtained from the chart shown in Figure 4-2 [29]. The damped frequency (ω_d) of the response can be measured directly from the period T between each peak. The average of the period T measured from each peak will be the final estimation of the damped period. The damped frequency is the inverse of the period T. Finally, the natural frequency can be estimated from the damping ratio and the damping frequency using Eq. 4-1.

$$\omega_n = \frac{\omega_d}{\sqrt{1-\zeta^2}} \qquad \textbf{Eq. 4-1}$$

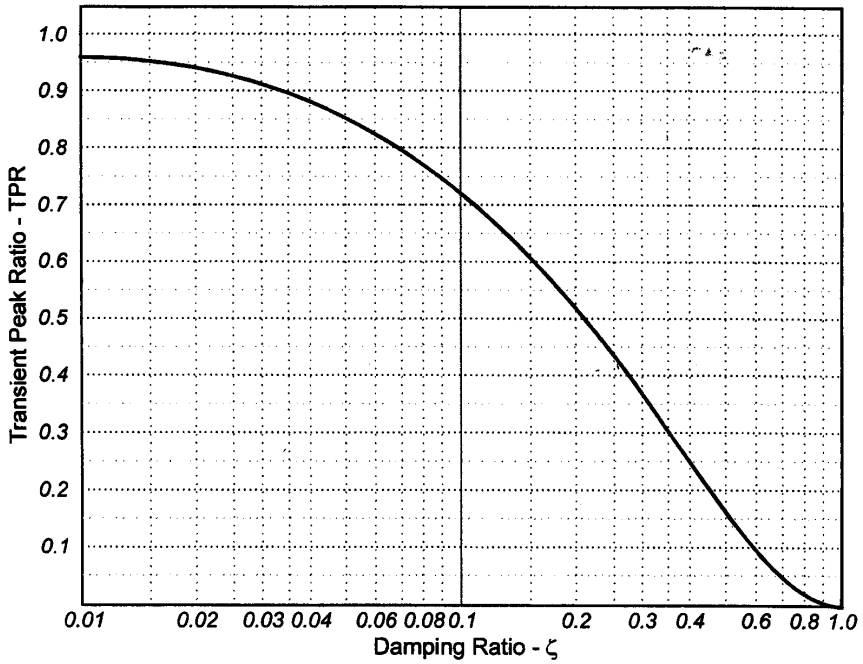

Figure 4-2. Damping Ratio Chart for the Transient Peak Ratio Method

4.3 Time Ratio Method

To apply this method, the user must be able to get the final steady state of the response after an oscillatory motion. It uses three specific values from the response to measure its relative response time. As shown in Figure 4-3 [29], the time history Δt_1, Δt_2 and Δt_3 is measured where the output response x reaches 0.736, 0.406, and 0.199 of the final steady state value Δx, respectively.

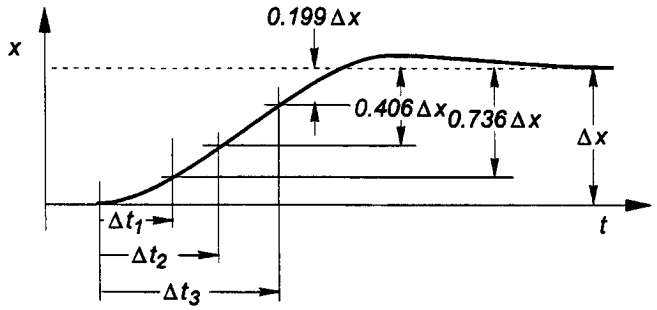

Figure 4-3. Time Ratio Method

The time ratios $\Delta t_2/\Delta t_1$, $\Delta t_3/\Delta t_1$ and $(\Delta t_3-\Delta t_2)/(\Delta t_2-\Delta t_1)$ are calculated and used to read the damping ratio from Figure 4-4 [29]. For instance, when using the time ratio term $\Delta t_3/\Delta t_1$ to read the damping ratio, the vertical axis of the chart is first used to locate the $\Delta t_3/\Delta t_1$ value. The damping ratio is read from the dashed line. Once the damping ratio is obtained, it is then used to assign the frequency time product value $\omega_n \Delta t_3$ from the solid line. The natural frequency ω_n is computed simply by dividing the $\omega_n \Delta t_3$ term by Δt_3. These procedures are then repeated for the time ratio terms $\Delta t_2/\Delta t_1$ and $(\Delta t_3-\Delta t_2)/(\Delta t_2-\Delta t_1)$ to read the other two sets of damping ratio and natural frequency data. The final estimated values are the average of those three measurements.

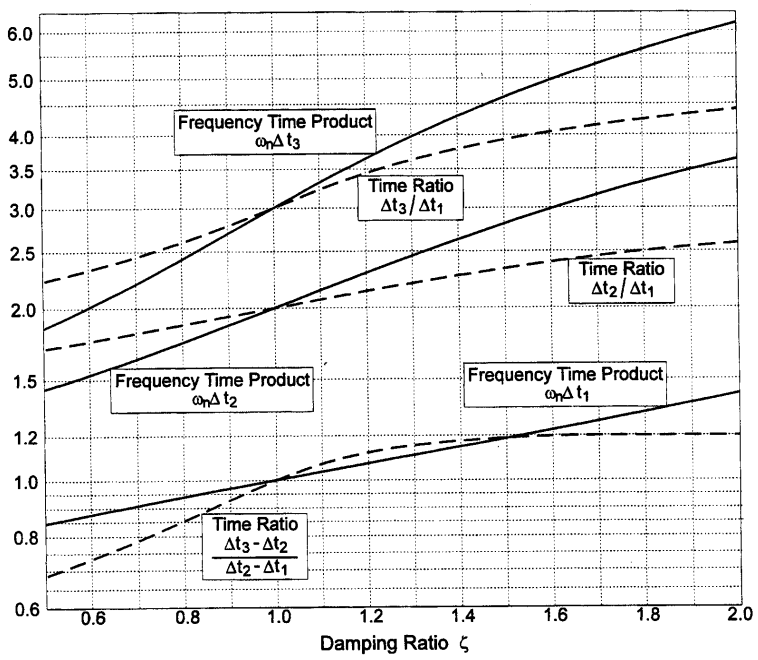

Figure 4-4. Damping Ratio Chart for the Time Ratio Method

4.4 Maximum Slope Method

The maximum slope method is suitable for a highly damped response with an overshoot. The parameters to be measured from the time domain response are illustrated in Figure 4-5 [29]. In this figure, Δx is the magnitude between the minimum and peak value of the response. Δx_1 is the magnitude between the maximum and final steady state value. Along the response curve, a tangent line is drawn to intersect two horizontal lines drawn from the maximum and minimum peak values. From the intersection points, draw two vertical lines to the time axis. The parameter Δt is the time increment between these two vertical lines. Then the ratio $\frac{\Delta x_1}{\Delta x}$ is calculated and used in Figure 4-6 [29] to measure the damping ratio. The natural frequency can be found by reading $\omega_n \Delta T$ from the previously estimated damping ratio value and is calculated simply from $\omega_n = \frac{\omega_n \Delta T}{\Delta T}$.

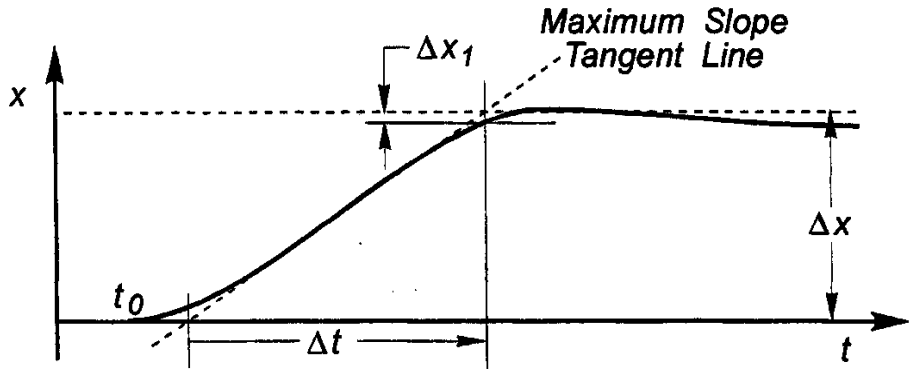

Figure 4-5. Maximum Slope Method

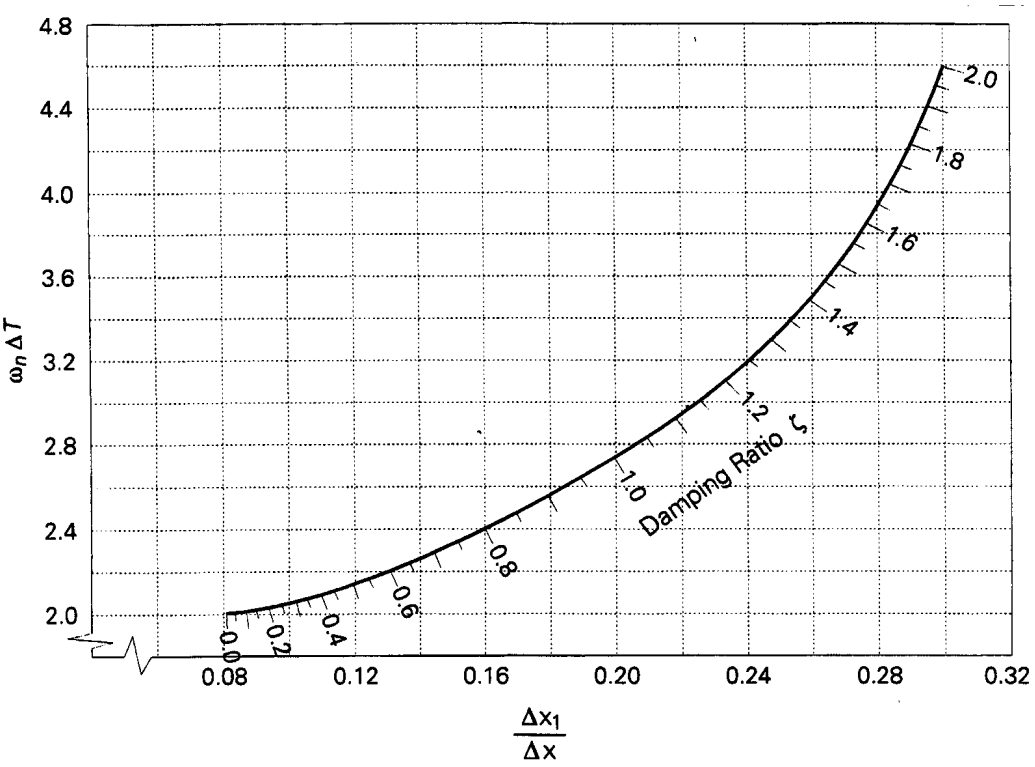

Figure 4-6. Damping Ratio Chart for the Maximum Slope Method

5 Open Loop Flight Testing of the Yak-54

The objective of the flight testing is to identify the true open loop dynamics of the Yak-54. This is done by using doublet control surface inputs to excite each mode's dynamics [29]. Data reduction is applied to the flight test data, and the final results are presented and compared with the analysis results from the previous state space model. The final comparison of the results are then discussed in detail.

5.1 Flight Test Procedure

For any flight test program, thorough flight test planning is required to ensure the safety of the flight test activities. A flight test document for the Yak-54 flight test program was established and is detailed in Reference [7].

5.2 Open Loop Dynamics Flight Test Results

In this section, the flight test data are presented for each mode starting with the lateral-directional dynamics and concluding with the longitudinal dynamics.

5.2.1 Dutch Roll Mode Flight Test Results

The Dutch roll mode test was conducted five times, and three sets of data with minimum disturbances were chosen for analysis; these are shown in Figure 5-1, Figure 5-2 and Figure 5-3. The TPR method is applied to estimate the

mode's dynamics. The data reduction analysis tables can be found in Appendix B and the final results are shown in Table 5-1.

Table 5-1. Summary of the Dutch Roll Mode Flight Test Analysis Results

	Test I	***Test II***	***Test III***	***Average***
Damping Ratio ξ	0.22	0.28	0.32	0.27
Natural Frequency ω_n (rad/sec)	6.04	5.95	5.10	5.70

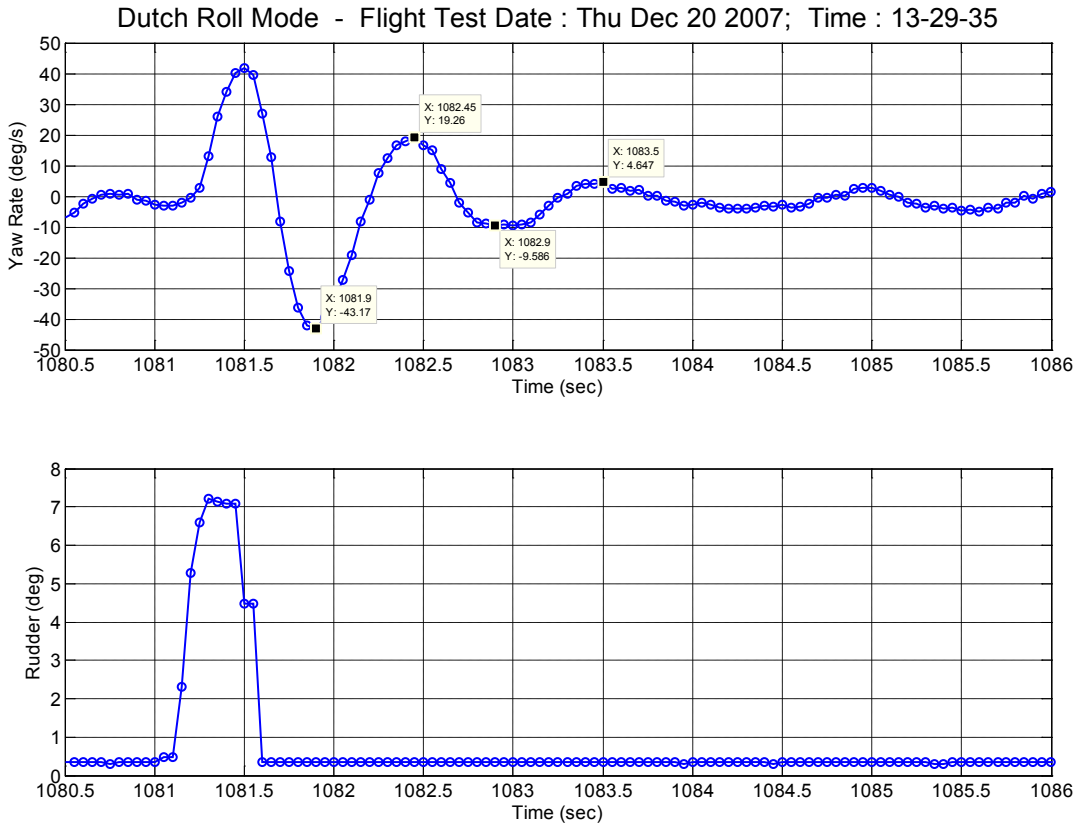

Figure 5-1. Dutch Roll Mode Flight Test Response - Test I

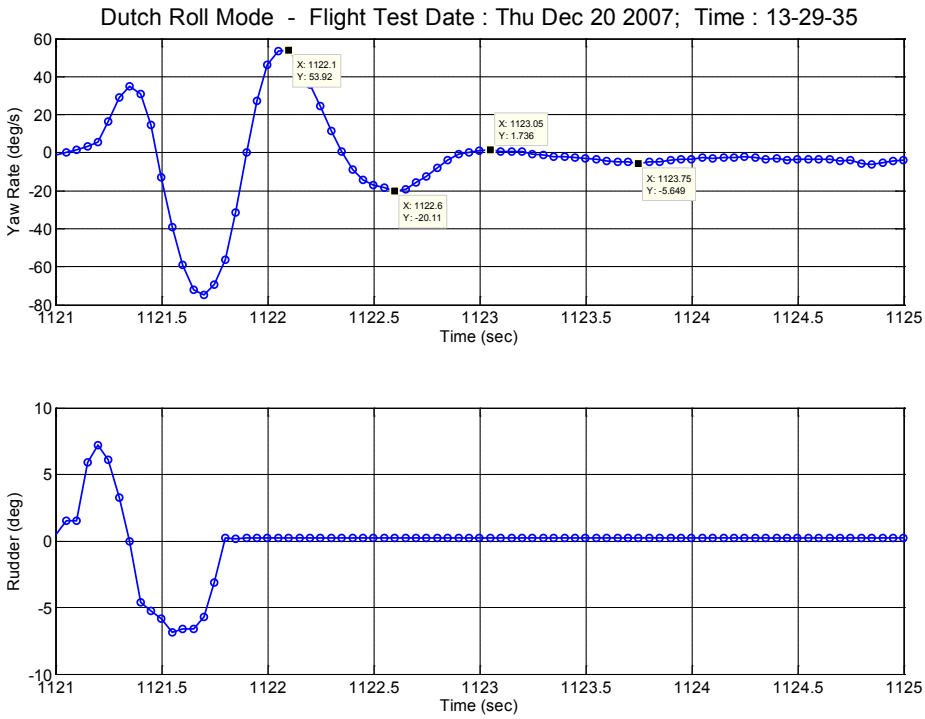

Figure 5-2. Dutch Roll Mode Flight Test Response - Test II

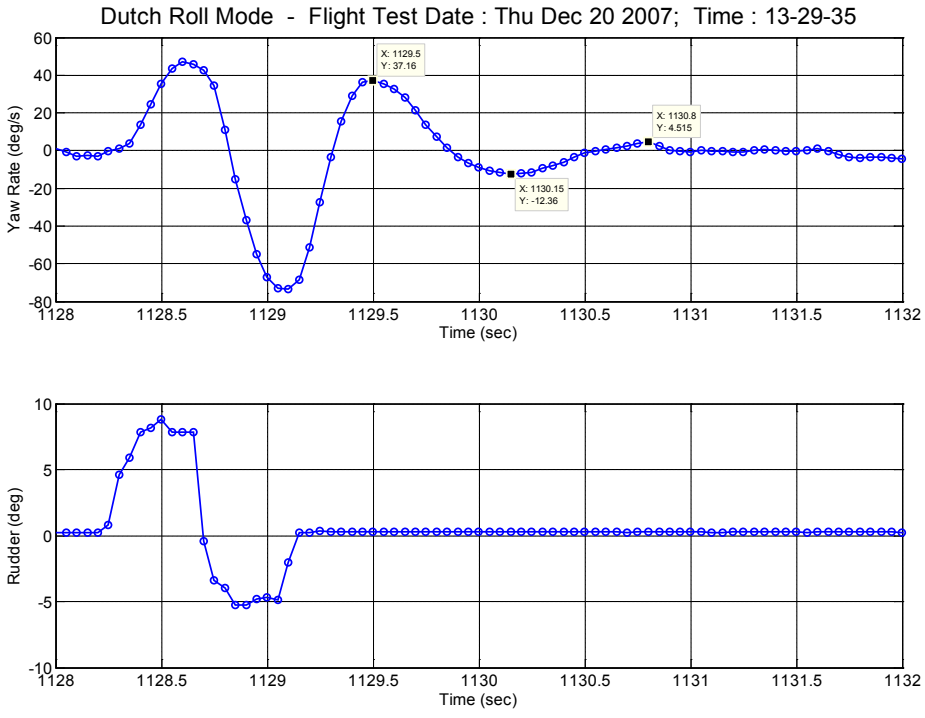

Figure 5-3. Dutch Roll Mode Flight Test Response - Test III

5.2.2 Roll Mode Flight Test Results

Three sets of roll mode flight test data are shown in Figure 5-4, Figure 5-5, and Figure 5-6. Since the roll mode is first order, the time constant (τ_{roll}) [33] is used to define the dynamics of this mode. As shown from the flight test, the Yak-54 demonstrates very fast roll dynamics. This increases the difficulty in using a graphical approach to accurately identify the time constant. For this reason, another method is used to provide an accurate comparison between the flight test data and the analysis results. This comparison technique will be discussed in Section 5.3.4.

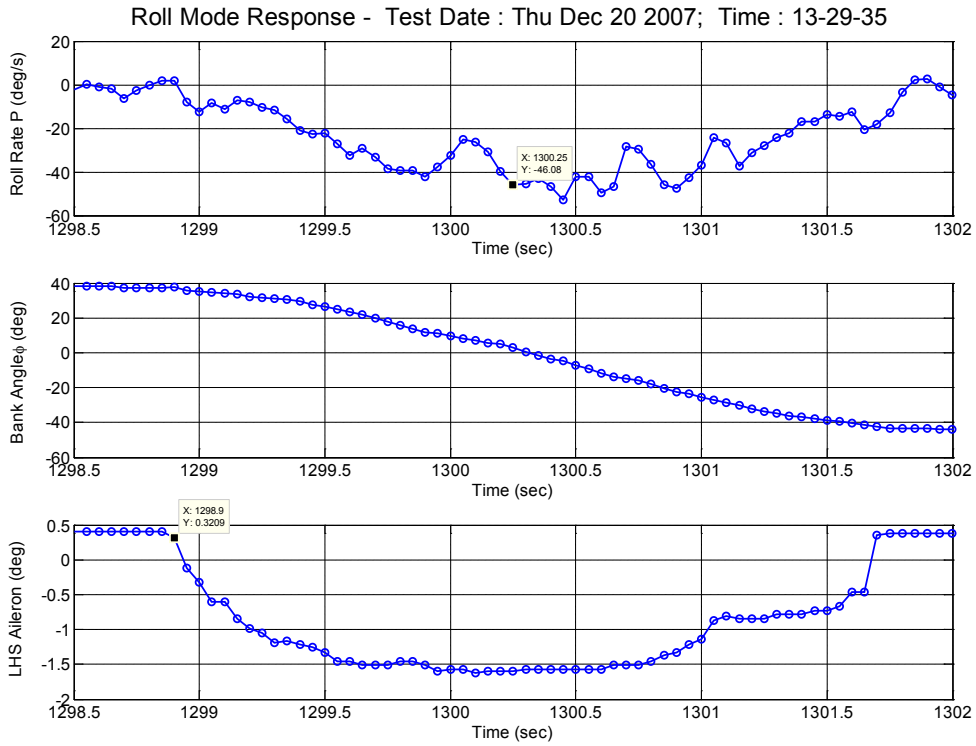

Figure 5-4. Roll Mode Flight Test Response - Test I

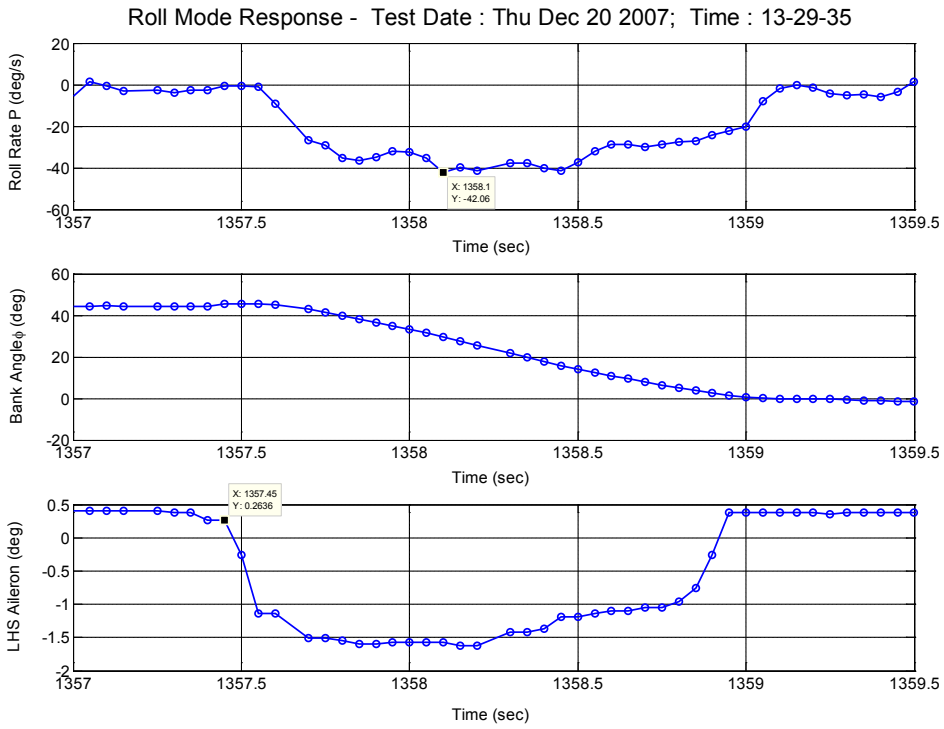

Figure 5-5. Roll Mode Flight Test Response - Test II

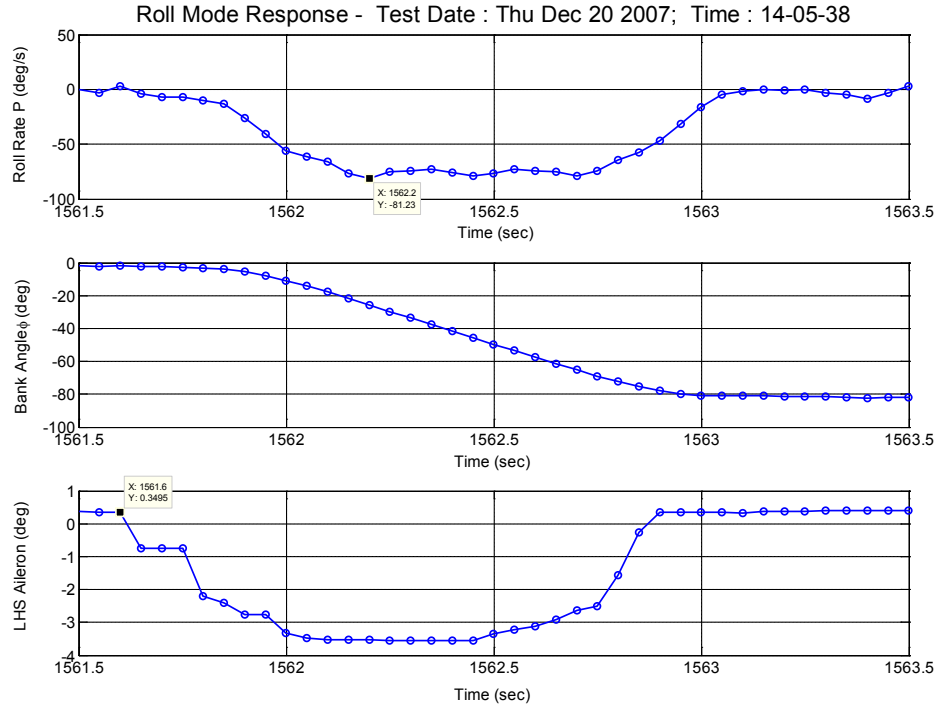

Figure 5-6. Roll Mode Flight Test Response - Test III

5.2.3 Short Period Mode Flight Test Results

Three sets of flight test data for the short period mode are illustrated in Figure 5-7, Figure 5-8, and Figure 5-9. Note that the short period mode experienced a highly damped response with no oscillation. The Time Ratio (TR) method is used to analyze the short period mode flight test data. Appendix C shows the data reduction analysis tables, and the summary of the analysis results is shown in Table 5-2.

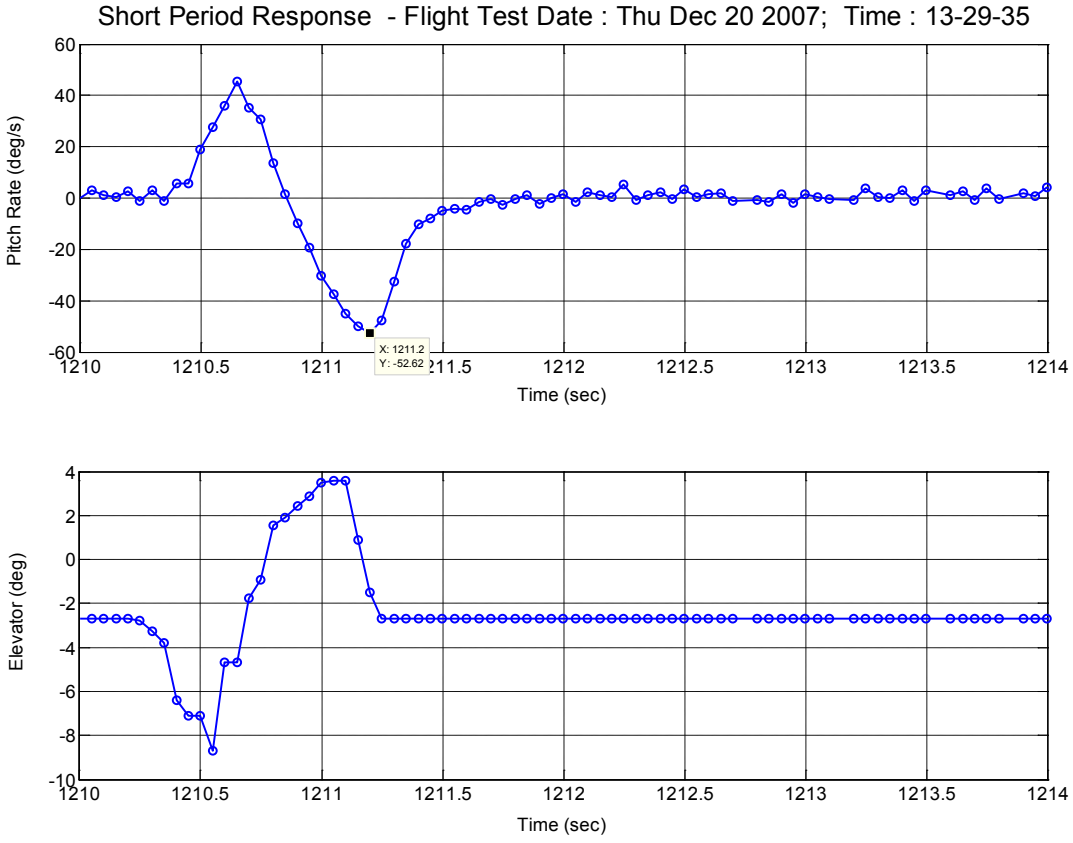

Figure 5-7. Short Period Mode Flight Test Response - Test I

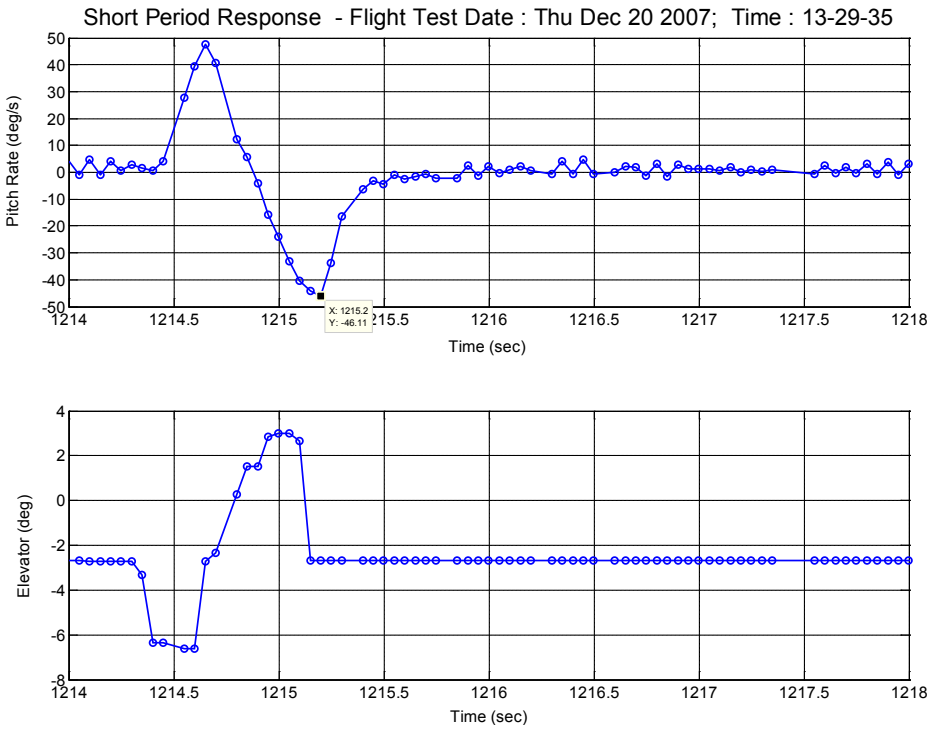

Figure 5-8. Short Period Mode Flight Test Response - Test II

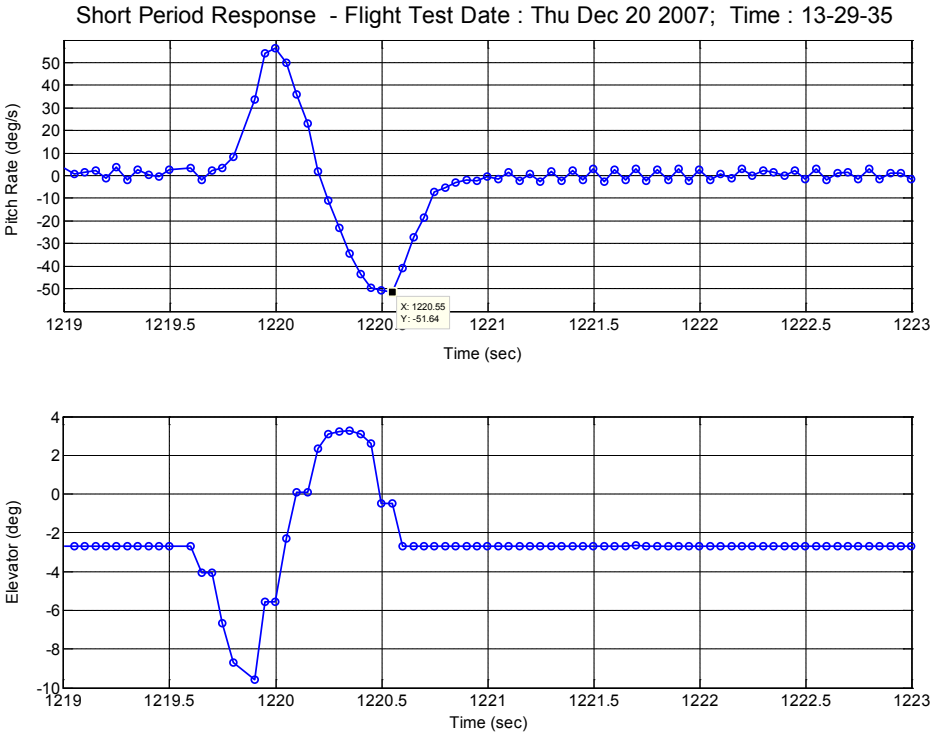

Figure 5-9. Short Period Mode Flight Test Response - Test III

Table 5-2. Summary of Short Period Mode Flight Test Analysis Results

	Test I	*Test II*	*Test III*	*Average*
Damping Ratio ξ	0.97	1.00	1.03	1.00
Natural Frequency ω_n ***(rad/sec)***	13.47	19.96	16.44	16.62

5.2.4 Phugoid Mode Flight Test Results

The Phugoid mode flight tests were performed twice. The mode was excited by an elevator step input to gain altitude until the airspeed dropped about 10 knots while the throttle remained constant. Once the airspeed dropped, the elevator input was released and the aircraft was allowed to oscillate freely.

During the flight test, it was realized that the Phugoid mode test is difficult for an RC pilot to conduct. This is due to the fact that the Phugoid mode has a very long oscillatory period. Before a full oscillation is completed, the RC pilot has to regain control of the aircraft before the aircraft flies outside of a safe visual range. From the flight test data shown in Figure 5-10 and Figure 5-11, the Phugoid mode test was not completed.

Due to the lack of sufficient data from these two incomplete tests, the data reduction method could not be used to determine the Phugoid mode dynamics. However, the Test II data reveals that the first peak of the oscillation did not occur within the initial eight seconds after the altitude began to increase. The time required to reach the first peak is a quarter of a complete period. Therefore, it can be anticipated that the period of the Phugoid mode should not be less than 32 seconds (a natural frequency < 0.19 rad/sec).

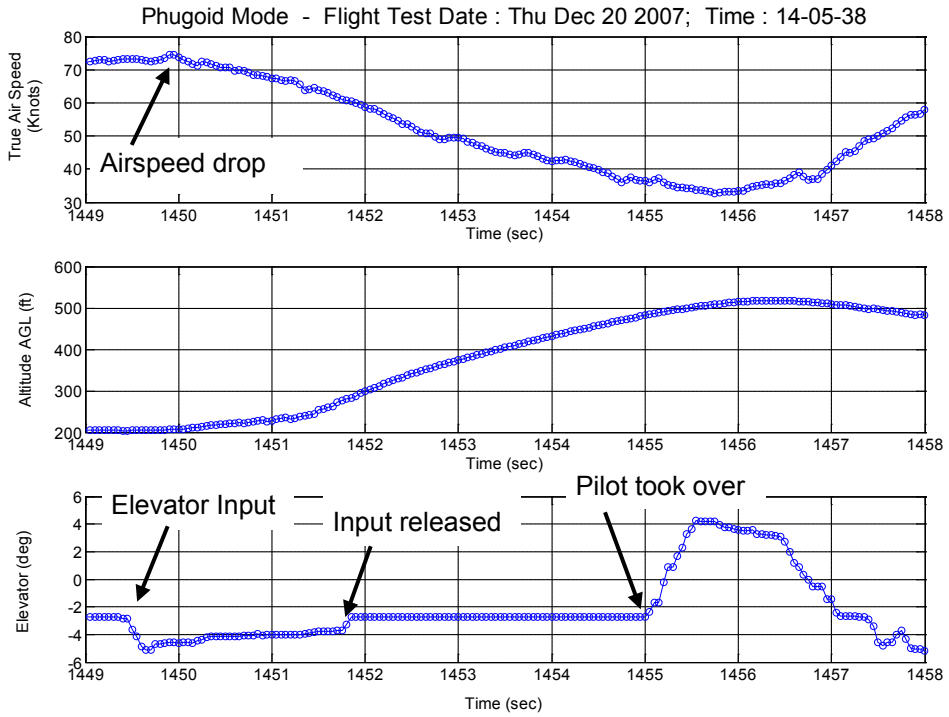

Figure 5-10. Phugoid Mode Flight Test Response - Test I

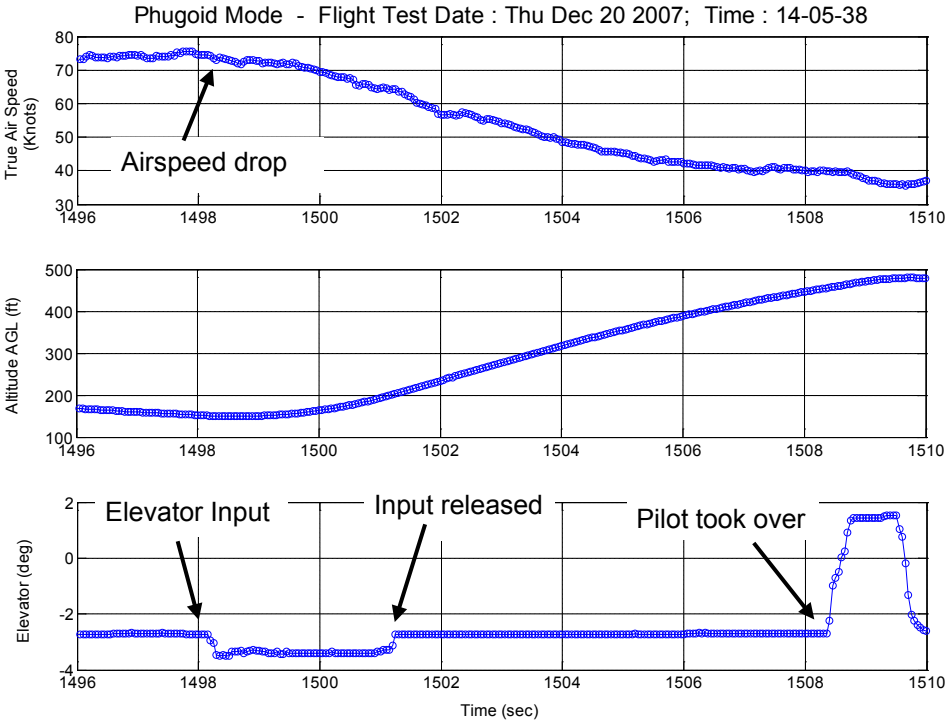

Figure 5-11. Phugoid Mode Flight Test Response - Test II

5.3 Comparison of Flight Test and Analysis Results

The flight test results are now compared with the analysis from the state space model using the AAA derivative values. The comparison is summarized in Table 5-3.

Table 5-3. Comparison of Flight Test and Simulation Model Dynamics

Model & Analysis Method	*Lateral-Directional Dynamics*				*Longitudinal Dynamics*			
	Spiral	*Roll*	*Dutch Roll*		*Short Period*		*Phugoid*	
	τ *(sec)*	τ *(sec)*	ξ	ω_n *(rad/s)*	ξ	ω_n *(rad/s)*	ξ	ω_n *(rad/s)*
AAA Model	86.96	0.06	0.19	6.88	0.90	9.42	0.42	0.27
Flight Test Results	----	0.45	0.27	5.70	1.00	16.62	----	< 0.19

5.3.1 Comparison of the Dutch Roll Mode

The Dutch roll mode dynamics comparison reveals that the AAA model slightly underestimates the damping ratio and predicts a higher natural frequency.

5.3.2 Comparison of the Short Period Mode

For the short period mode dynamics, Table 5-3 indicates that the damping ratio estimated from the AAA method closely matches the flight test data. Keep in mind that according to the flight test results, the aircraft demonstrated a very highly damped short period response with no oscillation. Therefore, the natural frequency is not reliable and should not be used to evaluate the results.

5.3.3 Comparison of the Phugoid Mode

The damping ratio of the Phugoid mode cannot be compared, due to the incomplete flight tests. For the natural frequency, it shows that the AAA model overestimates the value. However, since the flight test results are extrapolated from a one-quarter oscillatory cycle, errors may be involved in this estimation.

5.3.4 Comparison of the Roll Mode

As discussed before, the time constant for the roll mode should not be compared directly. The time constant calculated from the eigenvalue analysis refers to a singlet aileron step input, which is an instant input with no time delay. However, the actual pilot inputs from the flight test data take about 0.5 seconds to establish a constant aileron input, which is eight to twelve times longer than the calculated time constant given from the AAA model.

The roll mode time constant for the Yak-54 is very small, making it highly affected by the elapsed time of the aileron input. The only way to truly evaluate the results is to make a side-by-side comparison using identical aileron inputs. This can be done on the MATLAB/Simulink platform using the AAA based state space model.

The pilot commands used in the roll mode test are first extracted from the flight test data. These commands are then placed into the AAA state space models in MATLAB/Simulink to simulate the responses. The simulation results are then compared with the flight test data so that a side-by-side comparison can

be achieved based on identical inputs. Note that the trim values for the control surfaces are essential, as they will affect the dynamic responses of the aircraft about the trim condition. The pilot commands shown in the flight test data reflect the actual trim values set by the pilot. In the simulation, the aircraft state space model was trimmed at a predefined condition. Therefore, any control commands placed on the simulator are perturbation signals. To compensate, the trim value used for simulation input needs to be reset through the following equation:

$$\delta_{simulation} = \delta_{telemetry} - \delta_{actual\ \ trim} \qquad \textbf{Eq. 5-1}$$

The comparison of the results from the roll mode tests I, II and III are shown in Figure 5-12, Figure 5-13, and Figure 5-14, respectively. It clearly shows that the roll dynamics predicted by the AAA model is overestimated. In fact, if only the time constant characteristics are considered, the simulation results demonstrate similar performance with very fast responses that closely match the flight test data. This implies that the time constant estimate from the state space model is correct. The amplitude of the roll rate response, however, is overestimated and thus results in larger bank angle values than seen in the flight test results.

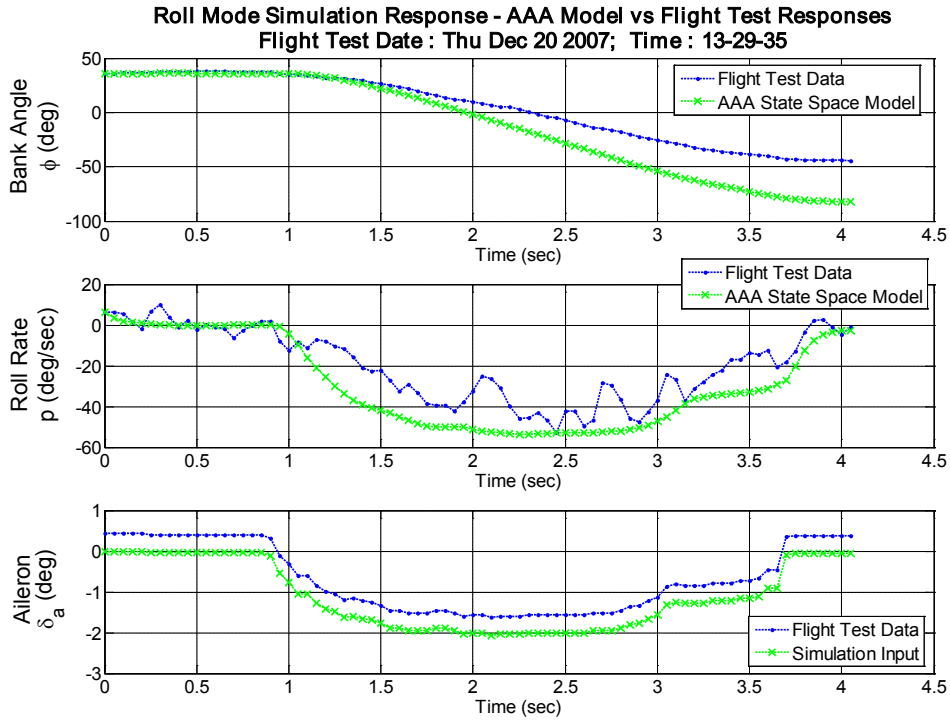

Figure 5-12. AAA vs Flight Test Response in Roll Mode Flight Test I

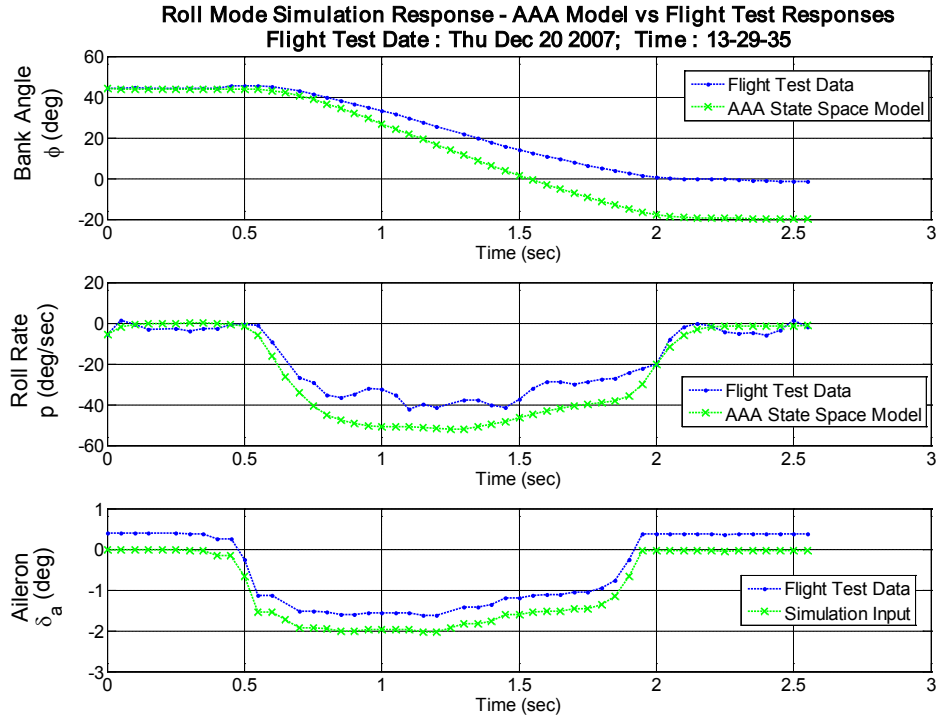

Figure 5-13. AAA vs Flight Test Response in Roll Mode Flight Test II

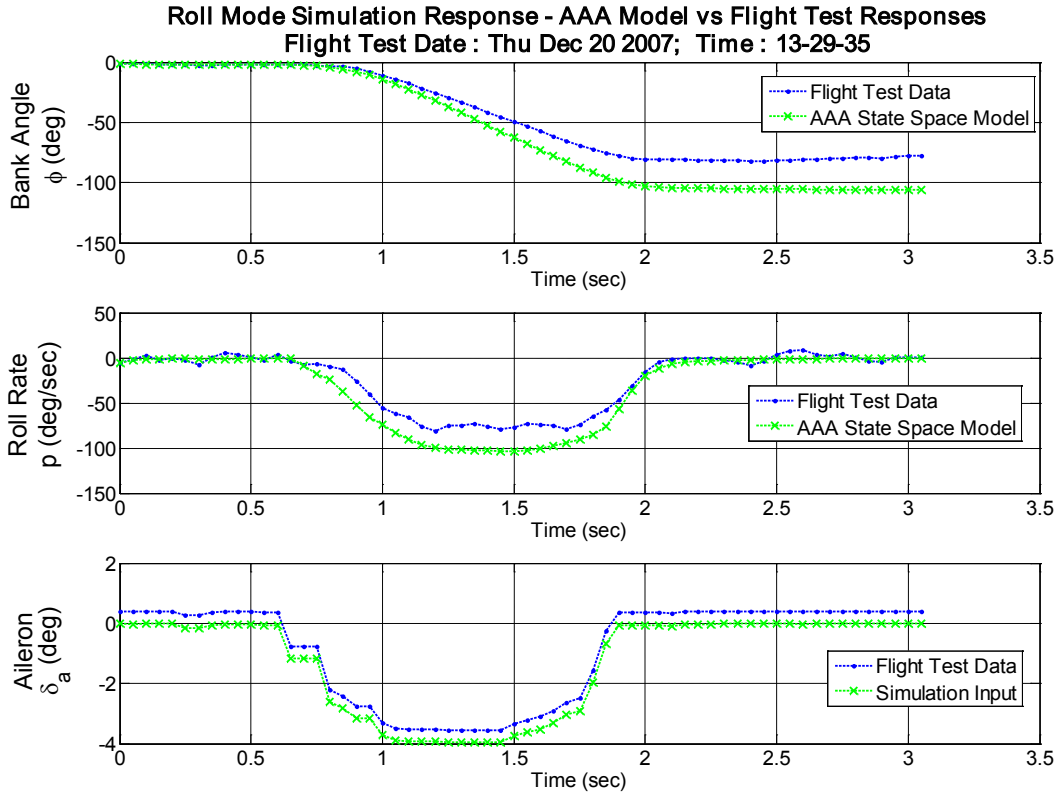

Figure 5-14. AAA vs Flight Test Response in Roll Mode Flight Test III

In addition to the AAA method, an investigation was conducted using another modeling method [9]. In this study, the Athena Vortex Lattice (AVL) method [34] was used to model the Yak-54 RC aircraft. The result reveals that the AVL method gives a better estimate than the AAA method of the lateral-directional derivatives, while the AAA method excels in modeling longitudinal dynamics. This finding led to the use of longitudinal derivatives from the AAA model and lateral-directional from the AVL model in the 6DOF nonlinear model. Table 5-4 shows the list of derivatives used to develop the 6DOF nonlinear model. Note that the power relevant derivatives, i.e. C_{Txu}, are not shown in Table 5-4 as

an engine model is used in the 6DOF model to simulate the thrust forces. Therefore, the power derivatives are not required for the 6DOF nonlinear model.

Table 5-4. Stability Derivatives used in the 6DOF Nonlinear Model

Coefficients for Zero Angle of Attack (rad^{-1})							
C_{L_0}	C_{D_0}	C_{m_0}					
0.0000	0.0513	0.0020					
Longitudinal Derivatives from the AAA Model (rad^{-1})							
C_{D_u}	C_{D_α}	C_{L_u}	C_{L_α}	$C_{L_{\dot{\alpha}}}$	C_{L_q}	C_{m_u}	C_{m_u}
0.0011	0.0863	0.0017	4.5465	1.8918	5.5046	0.0002	0.0002
C_{m_α}	$C_{m_{\dot{\alpha}}}$	C_{m_q}	$C_{D_{\delta e}}$	$C_{L_{\delta e}}$	$C_{m_{\delta e}}$		
-0.3937	-4.3787	-8.0532	0.00	0.3792	-0.8778		
Lateral-Directional Derivatives from the AVL Model (rad^{-1})							
C_{y_β}	C_{y_p}	C_{y_r}	C_{l_β}	C_{l_p}	C_{l_r}	C_{n_β}	C_{n_p}
-0.2707	0.0194	0.2531	-0.0314	-0.5858	0.0743	0.1052	-0.0387
C_{n_r}	$C_{y_{\delta a}}$	$C_{y_{\delta r}}$	$C_{l_{\delta a}}$	$C_{l_{\delta r}}$	$C_{n_{\delta a}}$	$C_{n_{\delta r}}$	
-0.1156	0.00	0.2228	0.3707	0.0219	-0.0088	-0.1003	

6 Development of the 6DOF Nonlinear Model in MATLAB/Simulink

In this chapter, the development of a 6DOF nonlinear model for a one-third scale Yak-54 RC plane is presented. This 6DOF nonlinear model is constructed using the derivatives shown in Table 5-4. This 6DOF model is built based on the MATLAB/Simulink platform [30]. The structure of the 6DOF model can be broken in several modules as illustrated in Figure 6-1. Discussions in this chapter are associated with each individual module. Appendix D shows the details of the 6DOF model's construction layer by layer.

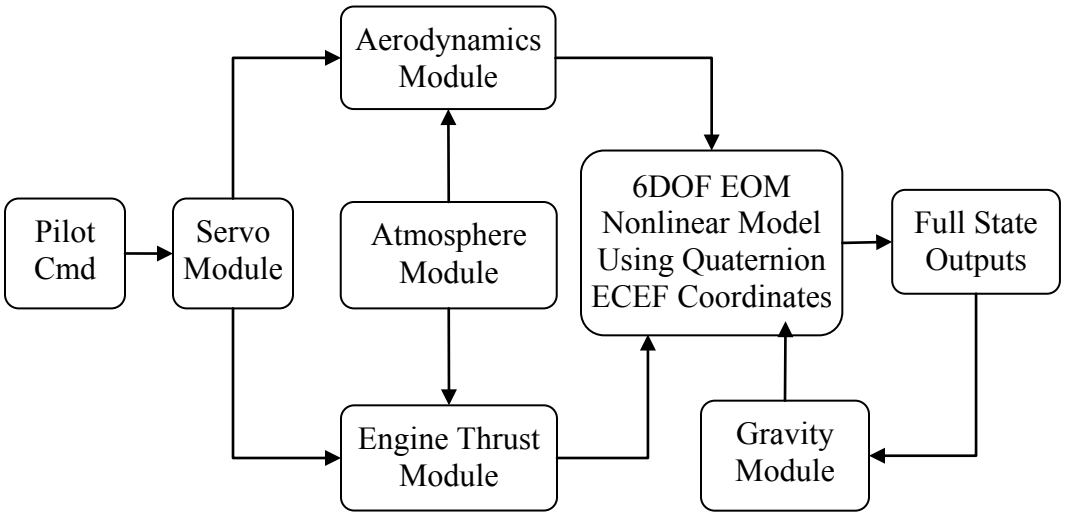

Figure 6-1. Block Diagram of the 6DOF Nonlinear Model

6.1 Coordinate System

The Earth-Centered Earth-Fixed (ECEF) coordinate system [35], [36] is used in constructing the 6DOF nonlinear model. Figure 6-2 [37] illustrates the ECEF coordinate system. The origin of the ECEF coordinate system is defined at the center of the Earth. This ECEF frame is rotating about the Earth-Centered Inertial (ECI) reference frame. The representation of the ECEF frame from the ECI frame is simplified by considering only a constant rotation about the Z-axis. The body of interest, the aircraft, is assumed to be rigid and is represented in the ECEF frame. The ECEF coordinate system is implemented in the "6DOF ECEF (Quaternion)" block from the Aerospace Blockset [37] in MATLAB/Simulink as shown on page 107 in Appendix D.

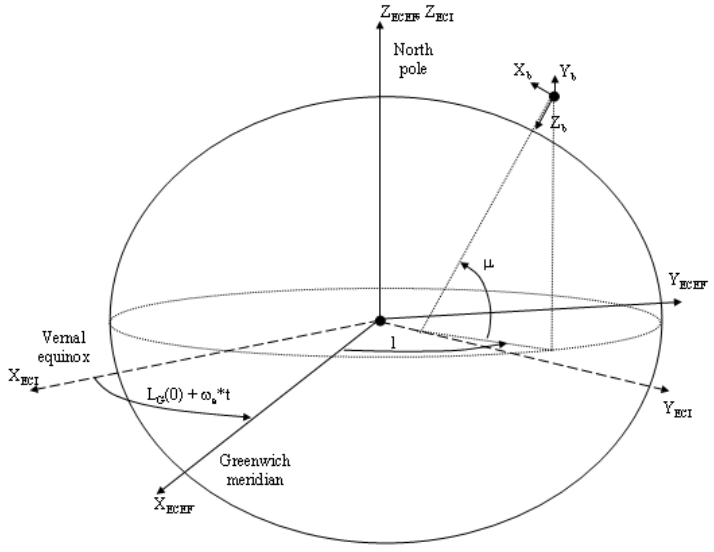

Figure 6-2. ECEF Coordinate System

6.2 Aircraft Attitude Representations

In aircraft simulations, there is a need for a mathematical technique to describe the position and orientation of the body of interest in both inertial and non-inertial coordinate systems. Various methods have been developed to determine the aircraft's attitude representation. These include the well-known Euler angles [38], the Euler-Axis rotation parameters [39], the direction cosines [40], [41], and the Euler-Rodrigus quaternions [42], [43], [44], [45]. Reference [46] gives an excellent detailed survey of these four different attitude representations with an emphasis on the quaternion method.

6.2.1 Euler Method

The Euler method is a well-known approach used for aircraft attitude representations and computations. The Euler method is defined based on the definition of Euler angle representations, which can be found in many texts such as References [25], [26], [27] and [28]. Using the Euler method, a vector transformation from the Earth-fixed axis to the Body-fixed axis and vice versa can be obtained through the transformation matrix shown in Eq. 6-1. The notations used in this equation are defined as follows: $S_x = Sin(x)$ and $C_x = Cos(x)$. The subscript "*b*" refers to the Body-fixed frames, and the subscript "*f*" refers to the Earth-fixed frame.

$$\begin{bmatrix} x_b \\ y_b \\ z_b \end{bmatrix} = \begin{bmatrix} C_\theta C_\psi & C_\theta S_\psi & -S_\theta \\ S_\phi S_\theta C_\psi - C_\phi S_\psi & S_\phi S_\theta C_\psi + C_\phi C_\psi & S_\phi C_\theta \\ C_\phi S_\theta C_\psi + S_\phi S_\psi & C_\phi S_\theta S_\psi - S_\phi C_\psi & C_\phi C_\theta \end{bmatrix} \begin{bmatrix} x_f \\ y_f \\ z_f \end{bmatrix} \quad \textbf{Eq. 6-1}$$

Since the Euler angles are functions of time, they need to be updated at each time step throughout the simulation process. The Euler kinematic equations are introduced for this purpose. Using the numerical integration method, the equations can be solved to compute the rate of change of the Euler angles in each given time step. The Euler kinematic equations are shown below.

$$\begin{bmatrix} \dot{\phi} \\ \dot{\theta} \\ \dot{\psi} \end{bmatrix} = \begin{bmatrix} 1 & S_\phi S_\theta / C_\theta & C_\phi S_\theta / C_\theta \\ 0 & C_\phi & -S_\phi \\ 0 & S_\phi / C_\theta & C_\phi / C_\theta \end{bmatrix} \begin{bmatrix} p \\ q \\ r \end{bmatrix} \quad \textbf{Eq. 6-2}$$

Note that when the pitch angle (θ) is equal to ±90 degrees, the kinematic equations cannot be defined and thus cannot be solved. This is known as the gimbal lock singularity problem.

6.2.2 Quaternion Method

The quaternion method is first defined based on the Euler-Axis [39] representation coordinate system, which is different from the Euler angle representation. In this section, the concept of the quaternion is presented briefly. The readers are strongly encouraged to read Reference [46] for an excellent background review of quaternions.

In the Euler-Axis representation, the orientation of the non-inertial frame (i.e. Body-fixed frame) relative to the inertial frame (i.e. Earth-fixed frame) can be described through a single total rotation angle Θ of the coordinate system with respect to a particular axis $\bar{E}$, which is defined as the Euler-Axis. The transformation is visualized in Figure 6-3.

In the Euler-Axis rotation, only one total rotation angle Θ and the Euler-Axis are needed to give the description of the new orientation. The Euler-Axis can be defined by three vector components E_x, E_y and E_z directed along the Euler-Axis with respect to a coordinate frame. As illustrated in Figure 6-3, the three vector components are defined in Eq. 6-3 [35].

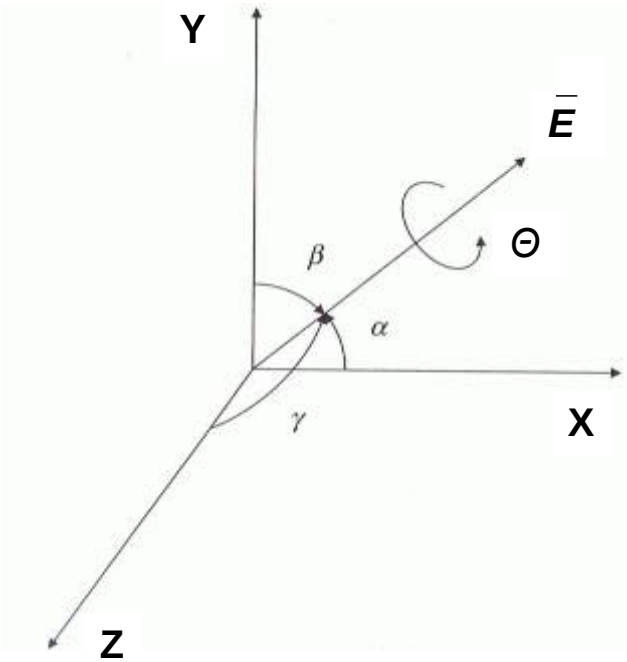

Figure 6-3. Representation of the Euler Axis

$$\begin{aligned} E_x &= Cos(\alpha) \\ E_y &= Cos(\beta) \\ E_z &= Cos(\gamma) \end{aligned} \qquad \textbf{Eq. 6-3}$$

The only purpose of the Euler-Axis is to give the definition of the rotational axis. Clearly, it could be of any arbitrary length. A constraint must be applied to fix the magnitude of the Euler-Axis vector. In general, the Euler-Axis is constrained as a unit vector as defined below:

$$\overline{E}^2 = E_x^2 + E_y^2 + E_z^2 = 1 \qquad \textbf{Eq. 6-4}$$

Now, the four quaternion terms are introduced as follows:

$$\begin{bmatrix} e_0 \\ e_x \\ e_y \\ e_z \end{bmatrix} = \begin{bmatrix} Cos(\Theta/2) \\ E_x Sin(\Theta/2) \\ E_y Sin(\Theta/2) \\ E_z Sin(\Theta/2) \end{bmatrix} \qquad \textbf{Eq. 6-5}$$

The quaternion terms also satisfies the property of orthogonality:

$$\begin{aligned} e_0^2 + e_x^2 + e_y^2 + e_z^2 &= Co^{\ 2}(\Theta/2) + \left(E_x^2 + E_y^2 + E_z^2\right) Sin^2(\Theta/2) \\ &= Cos^2(\Theta/2) + Sin^2(\Theta/2) \\ &= 1 \end{aligned} \qquad \textbf{Eq. 6-6}$$

Using these four quaternion terms, the transformation matrix between the inertial axis and the non-inertial axis are provided below.

$$\begin{bmatrix} x_b \\ y_b \\ z_b \end{bmatrix} = \begin{bmatrix} e_0^2 + e_x^2 - e_y^2 - e_z^2 & 2\left(e_x e_y + e_z e_0\right) & 2\left(e_x e_z + e_y e_0\right) \\ 2\left(e_x e_y - e_z e_0\right) & e_0^2 - e_x^2 + e_y^2 - e_z^2 & 2\left(e_y e_z + e_x e_0\right) \\ 2\left(e_x e_z - e_y e_0\right) & 2\left(e_y e_z - e_x e_0\right) & e_0^2 - e_x^2 - e_y^2 + e_z^2 \end{bmatrix} \begin{bmatrix} x_f \\ y_f \\ z_f \end{bmatrix} \quad \textbf{Eq. 6-7}$$

Similar to the Euler method, the quaternions need to be updated in each time step throughout the computational process. The kinematic equations for the quaternions are given in Eq. 6-8.

$$\begin{bmatrix} \dot{e}_0 \\ \dot{e}_x \\ \dot{e}_y \\ \dot{e}_z \end{bmatrix} = \frac{1}{2} \begin{bmatrix} 0 & -P & -Q & -R \\ P & 0 & R & -Q \\ Q & -R & 0 & P \\ R & Q & -P & 0 \end{bmatrix} \begin{bmatrix} e_0 \\ e_x \\ e_y \\ e_z \end{bmatrix} \quad \textbf{Eq. 6-8}$$

Note that the gimbal lock singularity problem that existed in the Euler method does not appear in the quaternion method. In addition, its transformation and kinematic matrices only require simple linear algebra computational steps, and no trigonometric steps are involved. This makes the quaternion method more efficient than the Euler method in terms of computational speed. In fact, many studies have been conducted which prove that the quaternion method provides the

greatest advantage for simulations in terms of computational efficiency. That becomes very important when a real-time simulation is required. Examples of these studies can be found in References [46], [47] and [48]. In this project, the quaternion method is used to develop the 6DOF nonlinear simulation model for the Yak-54.

6.2.3 Interpretation between Quaternion and Euler Angles

Although there are many advantages to using the quaternion method for an aircraft simulation, the physical interpretation of the quaternions is much less intuitive than the use of Euler angles. For this reason, it is convenient to correlate the results from quaternion based calculations with the Euler angles representation. This correlation can be generated by comparing Eq. 6-1 with Eq. 6-7.

$$\begin{bmatrix} e_0^2+e_x^2-e_y^2-e_z^2 & 2\left(e_xe_y+e_ze_0\right) & 2\left(e_xe_z+e_ye_0\right) \\ 2\left(e_xe_y-e_ze_0\right) & e_0^2-e_x^2+e_y^2-e_z^2 & 2\left(e_ye_z+e_xe_0\right) \\ 2\left(e_xe_z-e_ye_0\right) & 2\left(e_ye_z-e_xe_0\right) & e_0^2-e_x^2-e_y^2+e_z^2 \end{bmatrix} \quad \textbf{Eq. 6-9}$$

$$= \begin{bmatrix} C_\theta C_\psi & C_\theta S_\psi & -S_\theta \\ S_\phi S_\theta C_\psi - C_\phi S_\psi & S_\phi S_\theta C_\psi + C_\phi C_\psi & S_\phi C_\theta \\ C_\phi S_\theta C_\psi + S_\phi S_\psi & C_\phi S_\theta S_\psi - S_\phi C_\psi & C_\phi C_\theta \end{bmatrix}$$

Eq. 6-9 provides the relationship between the quaternions and the Euler angles. By comparing each matrix component one-by-one, the transformation between the quaternions and the Euler angles can be obtained as follows:

$$\begin{bmatrix} e_0 \\ e_x \\ e_y \\ e_z \end{bmatrix} = \begin{bmatrix} C_{\phi/2}C_{\theta/2}C_{\psi/2} + S_{\phi/2}S_{\theta/2}S_{\psi/2} \\ S_{\phi/2}C_{\theta/2}C_{\psi/2} - C_{\phi/2}S_{\theta/2}S_{\psi/2} \\ C_{\phi/2}S_{\theta/2}C_{\psi/2} + S_{\phi/2}C_{\theta/2}S_{\psi/2} \\ C_{\phi/2}C_{\theta/2}S_{\psi/2} - S_{\phi/2}S_{\theta/2}C_{\psi/2} \end{bmatrix} \quad \textbf{Eq. 6-10}$$

$$\begin{bmatrix} \phi \\ \theta \\ \psi \end{bmatrix} = \begin{bmatrix} aTan2\left[2\left(e_0e_x + e_ye_z\right), \left(e_0^2 + e_z^2 - e_x^2 - e_y^2\right)\right] \\ aSin\left[2\left(e_0e_y - e_xe_z\right)\right] \\ aTan2\left[2\left(e_0e_z + e_xe_y\right), \left(e_0^2 + e_x^2 - e_y^2 - e_z^2\right)\right] \end{bmatrix} \quad \textbf{Eq. 6-11}$$

The function aTan2 in Eq. 6-11 is a two argument arctangent function that determines the result in the proper quadrant by examining the signs of both arguments. The quaterion method is implemented in the "6DOF ECEF (Quaternion)" block from the Aerospace Blockset [37] in MATLAB/Simulink as shown on page 107 in Appendix D.

6.3 Servo Dynamics Module

The servo dynamics module simulates the dynamic characteristics of the actual servo movements from a given command. This refers to the response delay time between the command signals and the actual response time of the servos. To quantify the time delay of the servo, a servo delay tester, as shown in Figure 6-4, was designed for this purpose by the KU Aerospace Laboratory.

Figure 6-4. Servo Delay Tester

The servo delay tester is a device to measure the amount of time from when the command is sent from the joystick to the time when the servo actually reaches the commanded position. The tester consists of a 555 analog circuit timer that is triggered by the joystick command. The tested servo is mounted on the device and is attached with a small paddle that moves in the same direction the servo is to travel. This paddle makes contact with two micro switches that can be adjusted to set the desired travel angles required for the test. When a joystick command is given, it triggers the timer circuit and starts the timing cycle until the micro switch on the end side is actuated. The timer signal is displayed on an oscilloscope so that the servo travel dynamics after command triggering can be quantified.

On the Yak-54, a Hitec HS-5985MG servo [49] is used to actuate each control surface. It is a coreless digital servo driven by metal gears for high torque

delivery. The assumption is made that the servo dynamics behave as a first order system. For a first order system, the time constant [33] is used to describe the system response characteristics.

The micro switches were set 10 degrees apart so that the total elapsed time for 10 degrees of travel was measured. According to the test results, the average traveling time for 10 degrees of movement is 200 ms. Note that the result measured in this test is the total elapsed time to reach the final state, which differs from the definition of the time constant. According to Reference [33], for a first order system, the response time to reach the final value is about four times the time constant. Thus, the time constant for this servo can be approximated as $\tau \approx {}^{t_{ss}}\!/_{4} = {}^{0.2}\!/_{4} = 0.05\,\text{sec}$. Using this result, a first order transfer function, as expressed in Eq. 6-12, can be developed to simulate the dynamics of the servo response, and its implementation in MATLAB/Simulink is shown on page 106 in Appendix D.

$$T(s) = \frac{1}{\tau S + 1} = \frac{1}{0.05S + 1} = \frac{20}{S + 20} \qquad \text{Eq. 6-12}$$

6.4 The 6DOF Equations of Motion System

The core of the 6DOF nonlinear model are the EOM used in this simulation. In this 6DOF model, the standard six degrees of freedom nonlinear differential equations for a conventional fixed wing aircraft [25], [26], [27], [28] are used. These 6DOF nonlinear differential equations are written as Eq. 6-13 and Eq. 6-14.

Forces Equations:

$$\begin{aligned} m\left(\dot{U} - VR + WQ\right) &= mg_x + F_{A_x} + F_{T_x} \\ m\left(\dot{V} + UR - WP\right) &= mg_y + F_{A_y} + F_{T_y} \\ m\left(\dot{W} - UQ + VP\right) &= mg_z + F_{A_z} + F_{T_z} \end{aligned} \qquad \textbf{Eq. 6-13}$$

Moments Equations:

$$\begin{aligned} I_{xx}\dot{P} - I_{xz}\dot{R} - I_{xz}PQ + \left(I_{zz} - I_{yy}\right)RQ &= L_A + L_T \\ I_{yy}\dot{Q} + \left(I_{xx} - I_{zz}\right)PR + I_{xz}\left(P^2 - R^2\right) &= M_A + M_T \\ I_{zz}\dot{R} - I_{xz}\dot{P} + I_{xz}QR + \left(I_{yy} - I_{xx}\right)PQ &= N_A + N_T \end{aligned} \qquad \textbf{Eq. 6-14}$$

From a mathematical viewpoint, Eq. 6-13 and 6-14 form a set of six nonlinear differential equations with six unknown variables (*u, v, w, p, q, r)*. Each variable is presented in different equations and interacts with the others. Therefore, the equations cannot be solved individually. The total solution for the system can be obtained only by applying numerical integration to all equations for each given time step.

For the force equations, the inputs for the system are the three major forces applied to the aircraft. These are the aerodynamic forces, thrust forces, and gravity forces. These forces are nonlinear and time variant. The components of each force are broken down in detail and are discussed in Section 6.5, Section 6.6 and Section 6.7.

The inputs for the moment equation are the three moment terms applied to the three aircraft Body-fixed axes. These moments are generated from the aerodynamic and thrust forces with respect to the aircraft's center of gravity (C.G.). As the gravity forces are defined at the C.G. location, no moment is introduced by the gravity forces. In addition, when modeling the engine thrust forces for the Yak-54, the assumption is made that the thrust line passes through the C.G.. Therefore, the terms that contribute to the moment equations are only associated with the aerodynamic forces. These aerodynamic moment terms are broken down one-by-one and are presented in Section 6.5.

The variables *P, Q, R* from the 6DOF equations are applied to the quaternion kinematic equations Eq. 6-8 to update the quaternion terms. The updated quaternion terms are then used for vector coordinate transformations through Eq. 6-7. The updated orientation of the aircraft is provided from Eq. 6-11. The 6DOF nonlinear equations are implemented in the "6DOF ECEF (Quaternion)" block from the Aerospace Blockset [37] in MATLAB/Simulink as shown on page 107 in Appendix D.

6.5 Aerodynamics Module

As previously mentioned, the aerodynamics forces are one of the major forces applied to the aircraft, and these forces create aerodynamic moments that contribute to the moment equations. The main purpose of this aerodynamics module is to estimate the values of the aerodynamic forces and moments in the

aircraft body frame. A high level block diagram for this module can be simplified as seen in Figure 6-5.

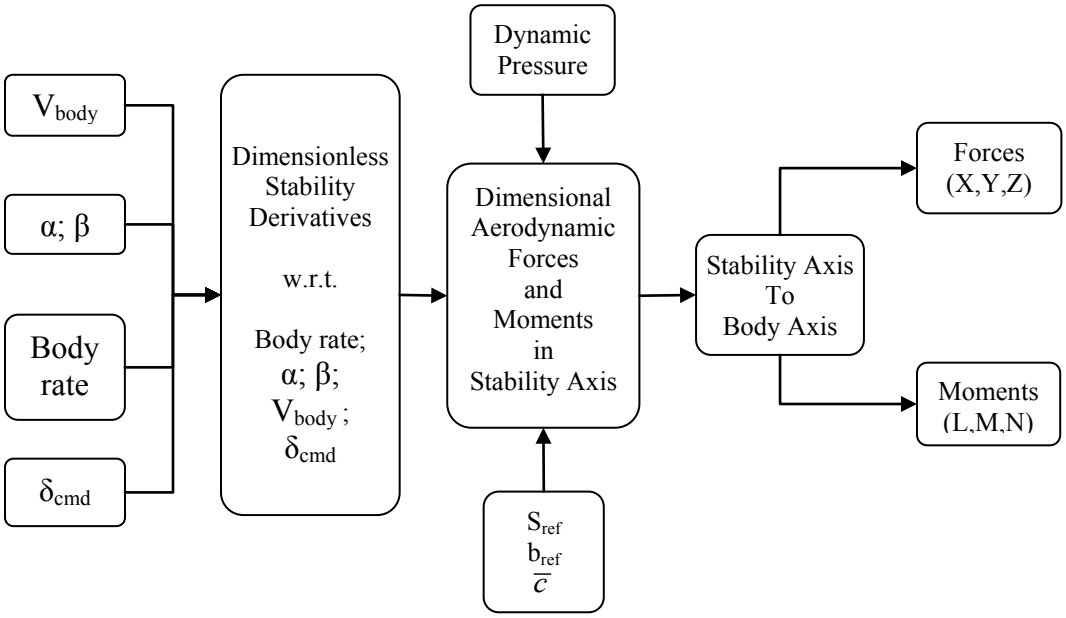

Figure 6-5. Block Diagram of Aerodynamics Module

The aerodynamic forces are composed of three forces, which are the lift, drag, and sideforce. These forces generate moments with respect to the center of gravity about the X, Y, Z-axis and are described as the rolling moment, pitching moment, and yawing moment. The component build-up method [25] [28] is used to generate the forces and moments. The total forces and moments that act on the aircraft are simply the summation of the forces and moments contributed by each component. This method has been widely used and found to be acceptable [21].

The aerodynamic forces and moments are first described as dimensionless coefficients, which are associated with the stability and control derivatives given

in the modeling results. Eq. 6-15 through Eq. 6-20 are used to implement the aerodynamic force and moment coefficients.

Lift coefficient:

$$C_L = C_{L_0} + C_{L_\alpha}\alpha + C_{L_u} \times \frac{u}{V_\infty} + C_{L_{\delta e}}\delta_e + \left(C_{L_q} q + C_{L_{\dot{\alpha}}}\dot{\alpha}\right) \times \frac{\overline{c}}{2V_\infty} \qquad \textbf{Eq. 6-15}$$

Drag coefficient:

$$C_D = C_{D_0} + \frac{C_L^2}{\pi e AR} + C_{D_\alpha}\alpha + C_{D_u} \times \frac{u}{V_\infty} + C_{D_{\delta e}}\delta_e \qquad \textbf{Eq. 6-16}$$

Sideforce coefficient:

$$C_Y = C_{Y_\beta}\beta + C_{Y_{\delta a}}\delta_a + C_{Y_{\delta r}}\delta_r + \left(C_{Y_p} p + C_{Y_r} r\right) \times \frac{b}{2V_\infty} \qquad \textbf{Eq. 6-17}$$

Pitch moment coefficient:

$$C_m = C_{m_0} + C_{m_\alpha}\alpha + C_{m_u} \times \frac{u}{V_\infty} + C_{m_{\delta e}}\delta_e + \left(C_{m_q} q + C_{m_{\dot{\alpha}}}\dot{\alpha}\right) \times \frac{\overline{c}}{2V_\infty} \qquad \textbf{Eq. 6-18}$$

Roll moment coefficient:

$$C_l = C_{l_\beta}\beta + C_{l_{\delta a}}\delta_a + C_{l_{\delta r}}\delta_r + \left(C_{l_p} p + C_{l_r} r\right) \times \frac{b}{2V_\infty} \qquad \textbf{Eq. 6-19}$$

Yaw moment coefficient:

$$C_n = C_{n_\beta}\beta + C_{n_{\delta a}}\delta_a + C_{n_{\delta r}}\delta_r + \left(C_{n_p} p + C_{n_r} r\right) \times \frac{b}{2V_\infty} \qquad \textbf{Eq. 6-20}$$

Note that when modeling the Yak-54 in this study, only one set of derivative values at the trim speed, as listed in Table 5-4, is implemented into the

above aerodynamic equations. Therefore, the equations are linear as they use linear aerodynamic derivatives. The exception is the drag coefficient equation. Also, the kinematics are nonlinear. However, if multiple sets of derivatives are available for different flight conditions, modeling changes in Mach number or angle of attack, those values can be used in the equations to capture nonlinear effects.

The six aerodynamic force and moment equations are implemented in the subsystem "Aerodynamics Coefficients" as shown on page 109 in Appendix D. This subsystem is broken down into four different subsystems shown on page 111. They are: 1) Coefficients w.r.t. Speed, 2) Coefficient w.r.t. Body Rate, 3) Coefficient w.r.t. Alpha and Beta Angles, and 4) Coefficient w.r.t. Deflection Angles for each Control Surface, which creates the inputs for Eq. 6-15 through Eq. 6-20.

For instance, the layout for the subsystem "Coef w.r.t. u" as shown on page 112 contains all the derivative coefficients related to the change in speed that contribute to Eq. 6-15 through Eq. 6-20. In this case, three derivatives contribute to portion of the system modeling the change in speed. They are C_{Du}, C_{Lu} and C_{mu}. These coefficients are implemented within a bus as six vector signals, which are tied to the six aerodynamic force and moment equations. Starting with the first vector, they are the drag coefficient, sideforce coefficient, lift coefficient, rolling moment coefficient, pitching moment coefficient, and yawing moment coefficient equations, respectively. Since there is no contribution to the sideforce, the

pitching moment and the yawing moment coefficient equations in the subsystem "Coeff w.r.t. u", they are connected to a zero value block.

Using the same construction technique, the rest of the derivative coefficients are implemented within the other three aforementioned subsystems to complete the construction of Eq. 6-15 through 6.20. They are illustrated on pages 111 through 119 in Appendix D.

The final dimensional values of the forces and moments are then computed from the dimensionless coefficients using the following equations.

Lift Forces:	$L = C_L \overline{q} S$	**Eq. 6-21**
Drag Forces:	$D = C_D \overline{q} S$	**Eq. 6-22**
Sideforces:	$F_{A_y} = C_Y \overline{q} S$	**Eq. 6-23**
Rolling Moment:	$L_A = C_l \overline{q} S b$	**Eq. 6-24**
Pitching Moment:	$M_A = C_m \overline{q} S \overline{c}$	**Eq. 6-25**
Yawing Moment:	$N_A = C_n \overline{q} S b$	**Eq. 6-26**

The force components shown in Eq. 6-21, 6-22, and 6-23 are defined in the stability axis. To make them useable within Eq. 6-13, which is defined in the Body-fixed axis, a coordinate frame transformation is needed to transfer the stability axis forces to Body-fixed axis forces using the equations expressed below.

$$\begin{bmatrix} F_{A_x} \\ F_{A_y} \\ F_{A_z} \end{bmatrix} = \begin{bmatrix} Cos(\alpha) & 0 & -Sin(\alpha) \\ 0 & 1 & 0 \\ Sin(\alpha) & 0 & Cos(\alpha) \end{bmatrix} \times \begin{bmatrix} -D \\ F_{A_y} \\ -L \end{bmatrix} \quad \textbf{Eq. 6-27}$$

The implementation of Eq. 6-21 through Eq. 6-27 is within the "Aerodynamic Forces and Moments" block from the Aerospace Blockset [37] in MATLAB/Simulink and is shown on page 109 in Appendix D.

6.6 Engine Dynamics and Thrust Force Module

Another major force applied to the aircraft system is the thrust force. In this section, the modeling techniques applied to generate the engine dynamics and the thrust forces are discussed. The objective of this module is to calculate the thrust forces for any given throttle position input.

The Yak-54 propulsion system uses a gasoline, single 3W 80cc XI CS engine [50] combined with a 26 x 10 propeller [50]. As no power measurement device is available to measure the engine power, a simplified method is used that assumes the engine RPM is only a function of the throttle position in any flight condition. An experiment was conducted on the ground to measure the thrust and RPM values with respect to the throttle positions; and the results are shown in Figure 6-6. Keep in mind that the thrust value shown here is the static thrust.

In order to simulate the thrust forces, it is necessary to use the dynamic thrust rather than the static thrust. The variation in dynamic thrust depends not only on the rotational speed of the propeller (RPM) but also on the forward flight speed (relative airspeed). For this reason, the advance ratio [26] [29] term *J*, as

shown in Eq. 6-28, is introduced. The advance ratio is a dimensionless term defined as a function of the forward airspeed (V_x) and the propeller rotational speed per second (n) as expressed below. The notation d refers to the diameter of the propeller.

$$J = \frac{V}{n \times d} \qquad \textbf{Eq. 6-28}$$

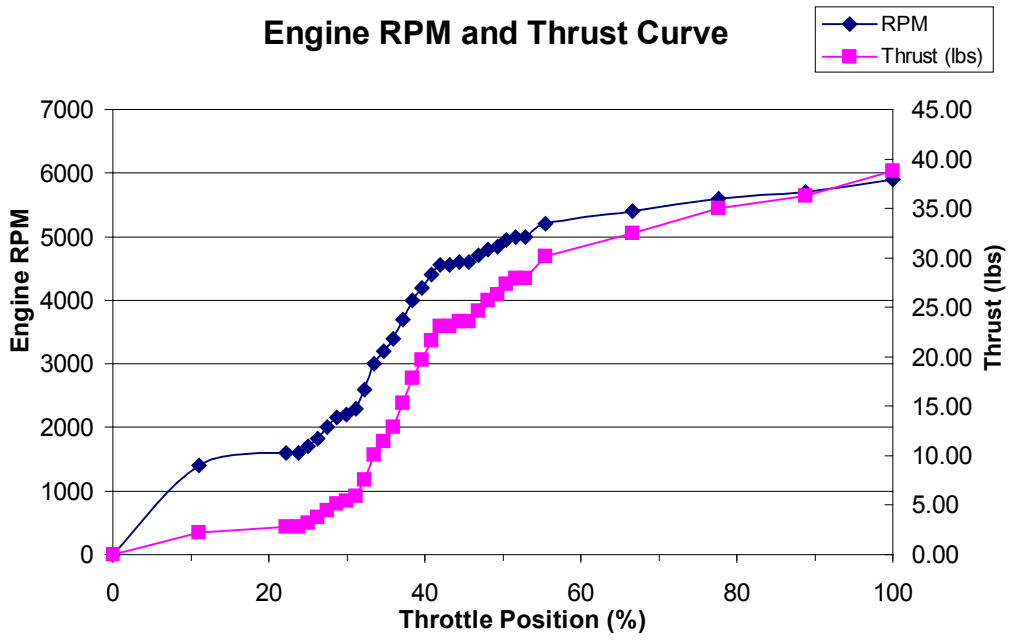

Figure 6-6. Engine RPM and Static Thrust Curve

Using blade element theory [26] [29], the thrust coefficient (C_T) and power coefficient (C_P) are defined and used to calculate the thrust forces and the power absorbed by the propeller as a function of advance ratio. The thrust and power coefficient curves depend mainly on the propeller diameters, number of

blades, airfoil shape, and pitch angle values. For industry standard products, the C_T and C_P coefficient data are available from the propeller manufacturer.

As the propeller used on the Yak-54 is a hobby grade product, no engineering data is available. Although a wind tunnel or a CFD method could be used to determine the C_T and C_P coefficients for the propeller, these methods are both time intensive and costly and are beyond the scope of this project. For these reasons, a computer program, JavaProp [51], is used to estimate these coefficients based on the configuration of the four propeller design parameters. The results are illustrated in Figure 6-7.

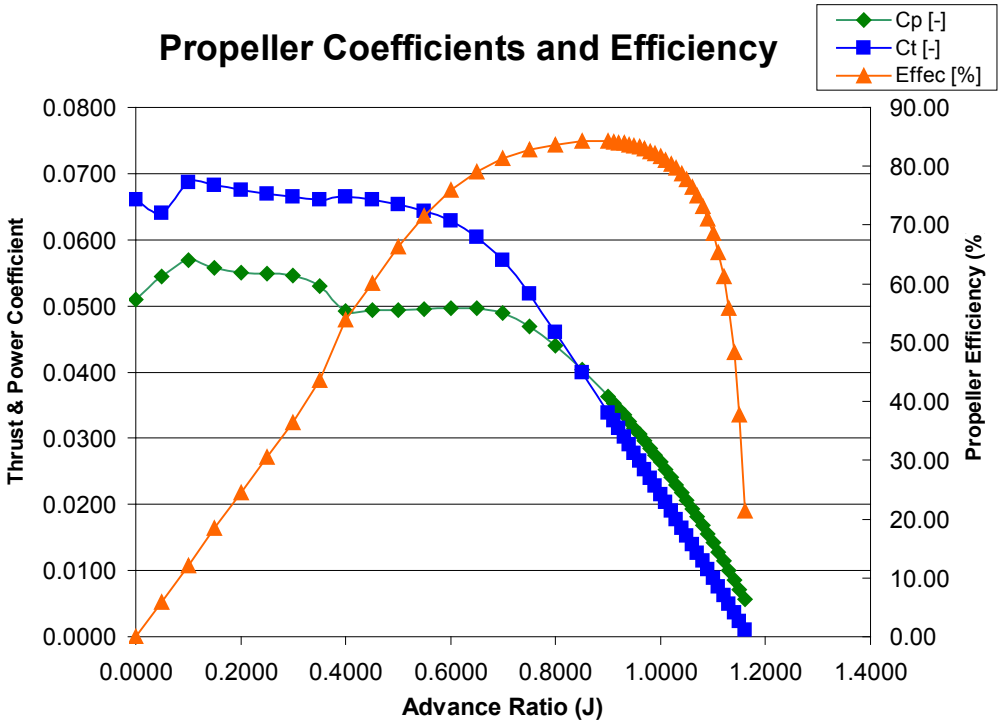

Figure 6-7. Thrust and Power Coefficients Curves for Propeller

The propeller coefficient curve demonstrates a typical performance chart for a fixed pitch propeller. As the advance ratio increases, the thrust coefficient decreases and thus less thrust force is generated. The generated thrust will become zero when it reaches a specific airspeed and RPM combination. Beyond this point, the sign of the thrust changes to the opposite direction denoting reversed thrust. This is known as the windmill effect [26]. The performance chart also reveals that this propeller provides its best efficiency when operated at the 0.85 advance ratio value.

The logic of the engine module is described as follows. For a given throttle input, the corresponding RPM output is determined according to the RPM curve. This RPM value is then used to calculate the advance ratio with the current airspeed feed back from the simulation model. The thrust coefficient can then be obtained from the thrust coefficient curve according to the calculated advance ratio value. Finally, the thrust force is computed using Eq. 6-29. These modeling steps are illustrated in Figure 6-8. The notation ρ_∞ used in Eq. 6-29 refers to the air density at the current altitude and is provided from the atmosphere module, which will be discussed shortly. The implementation of the engine module in MATLAB/Simulink is shown on page 108 in Appendix D.

$$T = \rho_\infty n^2 d^4 C_T \qquad \textbf{Eq. 6-29}$$

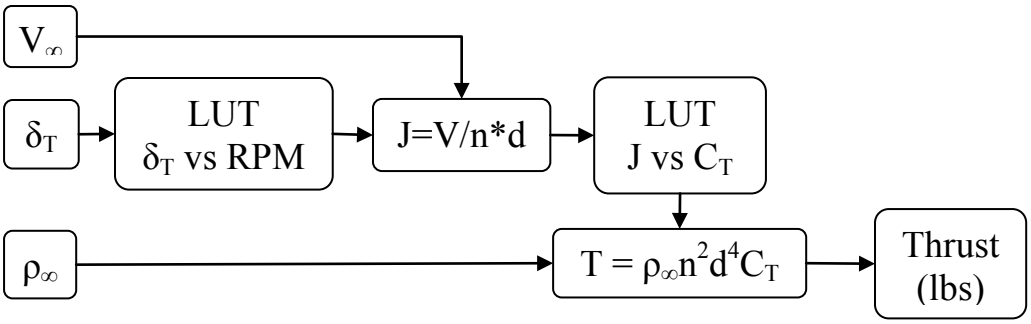

Figure 6-8. Block Diagram of the Engine and Thrust Module

The transient dynamics from the throttle input to the thrust output is simplified by using first order time delay dynamics. For this engine model, a 0.1 second time constant model is used to simulate these transient dynamics. The implementation equation is expressed in the transfer function Eq. 6-30, and its implementation in MATLAB/Simulink is shown on page 106 in Appendix D.

$$T(s) = \frac{1}{\tau S + 1} = \frac{1}{0.1S + 1} = \frac{10}{S + 10} \qquad \textbf{(Eq. 6-30)}$$

6.7 Gravity Module

Gravity is the last major force that is applied to the aircraft system. In most simple simulation models, gravity is always assumed to be constant regardless of the aircraft position and altitude with respect to the Earth. In this 6DOF nonlinear model, the World Geodetic System (WGS) is used to calculate the Earth's gravity at a specific location given from the inputs.

The concept of the WGS was first started during the late 1950s through the effort of United States Department of Defense, with the help of scientists from

other institutions and countries. It was motivated by the need for a unified WGS that could be used in geodesy and navigation worldwide. It was essential for global maps, navigation, aviation, and geography.

The WGS model was first developed in 1960 and was called WGS60. Since then, major updates have been made to improve the fidelity and the accuracy of the model using the latest technologies. The WGS72 was updated in 1972. The latest model is the WGS84 [52], which was published in the early 1980s. The WGS84 model is currently being used as the reference system for the Global Positioning System (GPS).

The "WGS84" model [37] is available from the Aerospace Blockset in MATLAB/Simulink. This model takes the input of the position in geodetic format (latitude, longitude, and altitude) and provides an output of three components of the gravity in the North-East-Down (NED) coordinate system [35].

A transformation is required from the NED frame to the body frame before applying the gravity values to Eq. 6-13 (force equations). This transformation is done through Eq. 6-7 using the quaternion method. The application of this "WGS84 Gravity"model in MATLAB/Simulink is illustrated on page 110 in Appendix D.

6.8 Atmosphere Module

During the simulation process, updated atmospheric data are frequently required to give feedback to some of the modules in order to provide the

necessary computational information. For this reason, an atmosphere module is required to provide the latest atmospheric data for the current altitude.

The 1976 COESA [53] (Committee on Extension to the Standard Atmosphere) atmospheric model is used here to fulfill this requirement. The work of the U.S. COESA was published in 1953, and major revisions were made in 1958, 1962, 1966, and 1976. Many U.S. government organizations contributed to this work, including NOAA (National Oceanic and Atmospheric Administration), NASA (National Aeronautics and Space Administration), and the U.S. Air Force. Various industries, research institutions, and universities also contributed. The COESA atmosphere model is identical to the Standard Atmosphere of the International Civil Aviation Organization (ICAO) up to 32 Km and the ISO (International Organization for Standardization) standard up to 50 Km.

The COESA 1976 is an idealized, steady-state representation of the earth's atmosphere from the surface to 1,000 km during moderate solar activity. The "COESA Atmosphere" model [37] is available in the MATLAB/Simulink Aerospace Blockset. This MATLAB/Simulink COESA model implements the mathematical representations of the 1976 COESA values and provides absolute temperature, pressure, density, and the speed of sound for a given geodetic altitude. The use of this "COESA Atmosphere" model is shown on page 110 in Appendix D.

7 Validation and Matching of the 6DOF Nonlinear Simulation Model with Flight Test Data

In this section, the flight test data are used to validate the simulation responses from the 6DOF nonlinear model. The side-by-side comparison technique, as introduced in Section 5.3.4, is used throughout this validation process.

The validation procedure is conducted through a complete set of comparisons for each individual mode's dynamics. This comparison is not limited to those responses related to each mode. For example, when evaluating the roll dynamics, the longitudinal responses are also compared so that a complete validation is studied. This process helps to provide useful insight for examining the coupling effect between the longitudinal and lateral responses for each mode's dynamics. The acceleration data on the body axes are also compared through this validation process.

7.1 Validation of Roll Mode Responses

Figure 7-1 shows the comparison of the roll dynamics between the flight test and simulation responses. The flight test data used here for comparison is the data set from the roll dynamics flight test II presented in Figure 5-5.

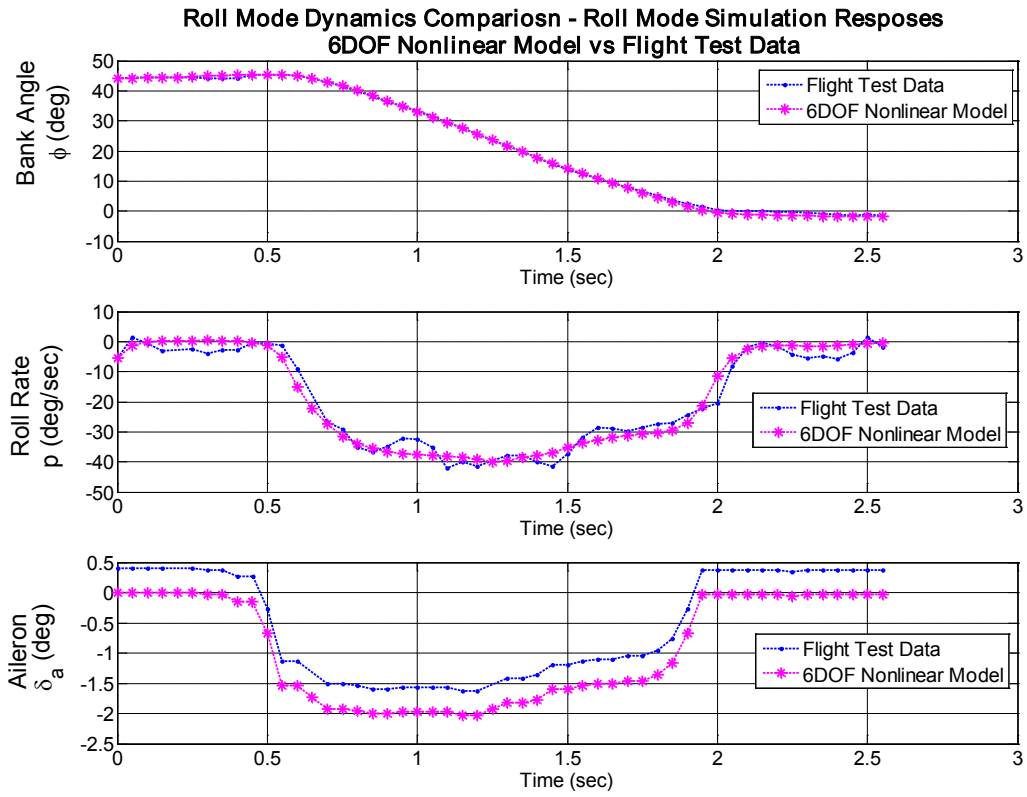

Figure 7-1. Roll Dynamics Comparison – Roll Axis Responses

Figure 7-1 shows that the roll dynamics simulation results closely match with the flight test data. The longitudinal responses are also compared in this roll dynamics test. Figure 7-2 and Figure 7-3 show the comparison results of the three axes body rate responses and the three axes Euler angle responses, respectively, using the identical set of roll dynamics flight data.

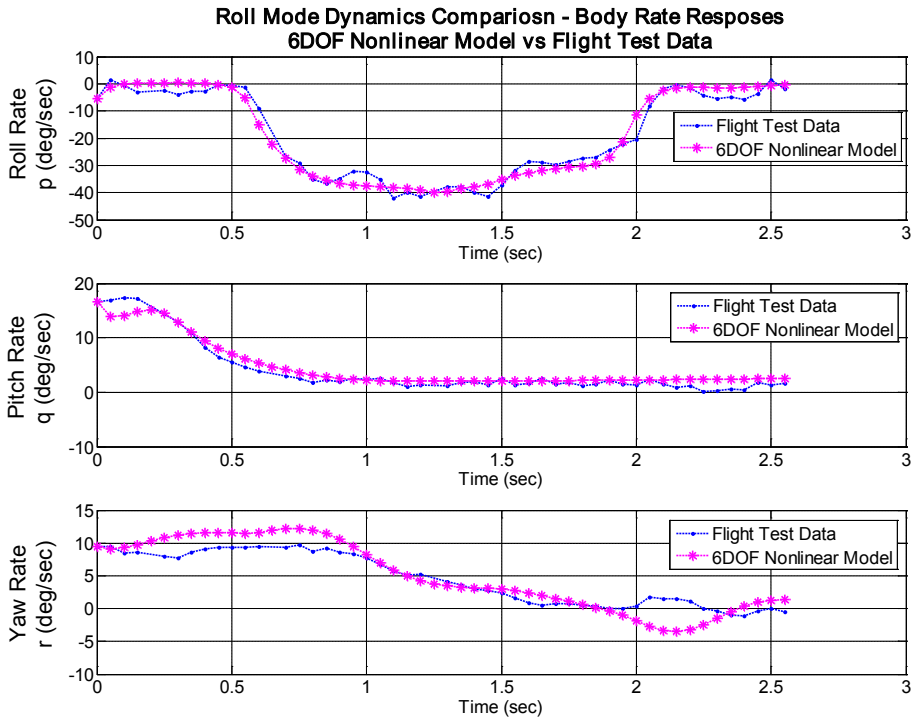

Figure 7-2. Roll Dynamics Comparison – Body Rate Responses

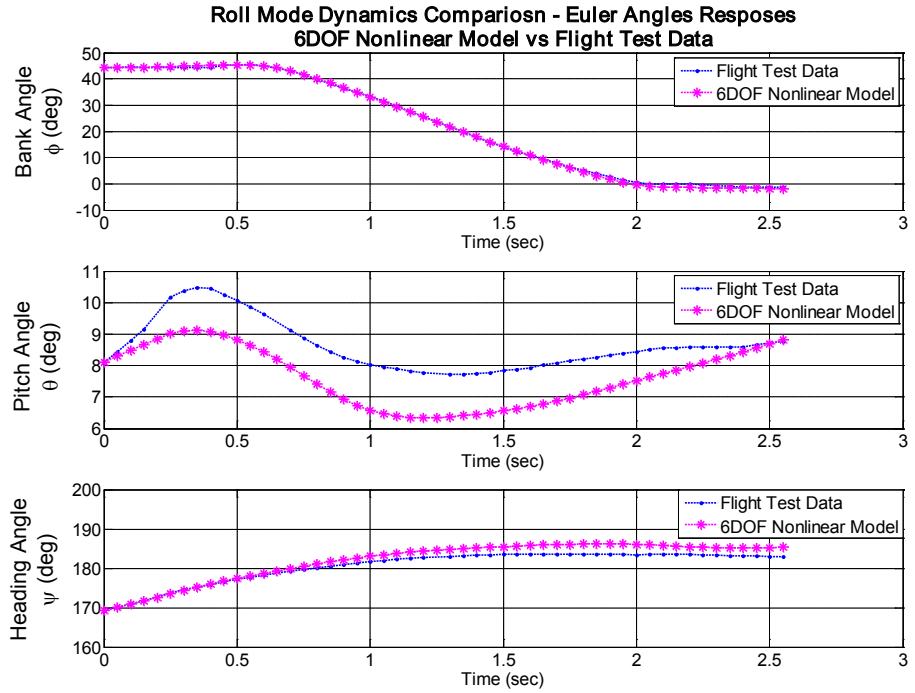

Figure 7-3. Roll Dynamics Comparison – Euler Angles Responses

The pitch rate responses in Figure 7-2 indicate that the 6DOF model closely matches the flight test data. The pitch angle simulation results as shown in Figure 7-3 provide trends similar to the flight test data. Overall, the 6DOF model demonstrates good performance in estimating the coupling effects between the lateral-directional and longitudinal dynamics. The 6DOF model also tracks very well with the flight test data on the heading angle response.

Before proceeding to compare the acceleration data, the interpretation of the acceleration data is explained here. The acceleration data from the flight tests are sensed by the three-axis accelerometer, which measures the three reaction forces applied to the airframe in the X, Y, Z Body-fixed axes. For instance, when on the ground or in steady level flight, the accelerometer would measure a -1 g load (instead of +1 g) applied along the Z-axis in the Earth-fixed coordinate system.

Based on Newton's second law, comparing the acceleration data would validate the force components estimated by the simulation model. Recall that the force components are the major inputs to the 6DOF EOM system. This comparison provides important information that helps to verify and improve the modeling accuracy.

The comparison of the acceleration data in the body-fixed axis from the same roll mode test is shown in Figure 7-4. For the Y-axis acceleration data, the simulation results closely match the flight test data. This indicates that the sideforce estimated by the 6DOF model is very accurate. The Z-axis acceleration

data given from the 6DOF model also tracks the flight test data very well, except at the initial condition where a 0.5 g difference is seen.

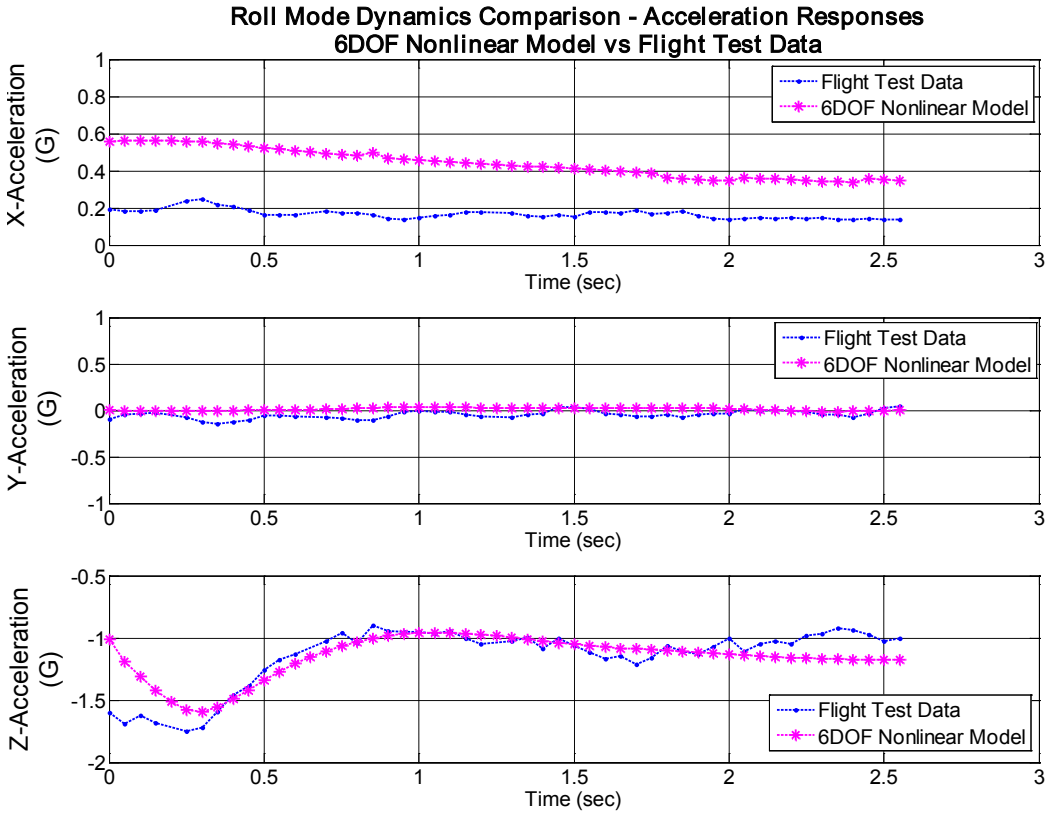

Figure 7-4. Roll Dynamics Comparison – Acceleration Data Responses

Recall that the Z-axis forces (F_{A_z}) in the body frame were computed from Eq. 6-27, which is a function of the angle of attack (AOA). This AOA value is fed back from the simulation outputs through the simulation process. However, an initial condition is required to start the computational process. Since the AOA was not available from the flight test data, an assumption was made that the initial

AOA value for the simulation is same as the trim AOA value from the AAA model. Keep in mind that this trim value is only valid when the aircraft is in a perfect steady level flight condition at 70 knots. Once the simulation process starts, this AOA is constantly updated and corrected. Therefore, the estimate of the Z-axis force can be calculated using the updated AOA value and its accuracy improved.

The thrust force makes a major contribution to the X-axis force. As discussed in Section 6.6, a simplified engine model was used to calculate the thrust forces. Besides, the assumption that the trim AOA value is the initial condition is also applied when calculating the X-axis forces in Eq. 6-27. The X-axis acceleration data reveals that the X-axis force (F_{A_x}) is overestimated in the 6DOF model. This is mostly due to the use of a simplified engine model that produces extra thrust.

7.2 Validation of Dutch Roll Mode Responses

Figure 7-5 shows the comparison of the yaw dynamics responses from a Dutch roll mode test. The flight test data used here is the Dutch roll mode test III data as presented in Figure 5-3. The result indicates that the damping ratio is underestimated by the nonlinear model, which is consistent with the conclusion from the eigenvalues analysis summarized in Table 5-3.

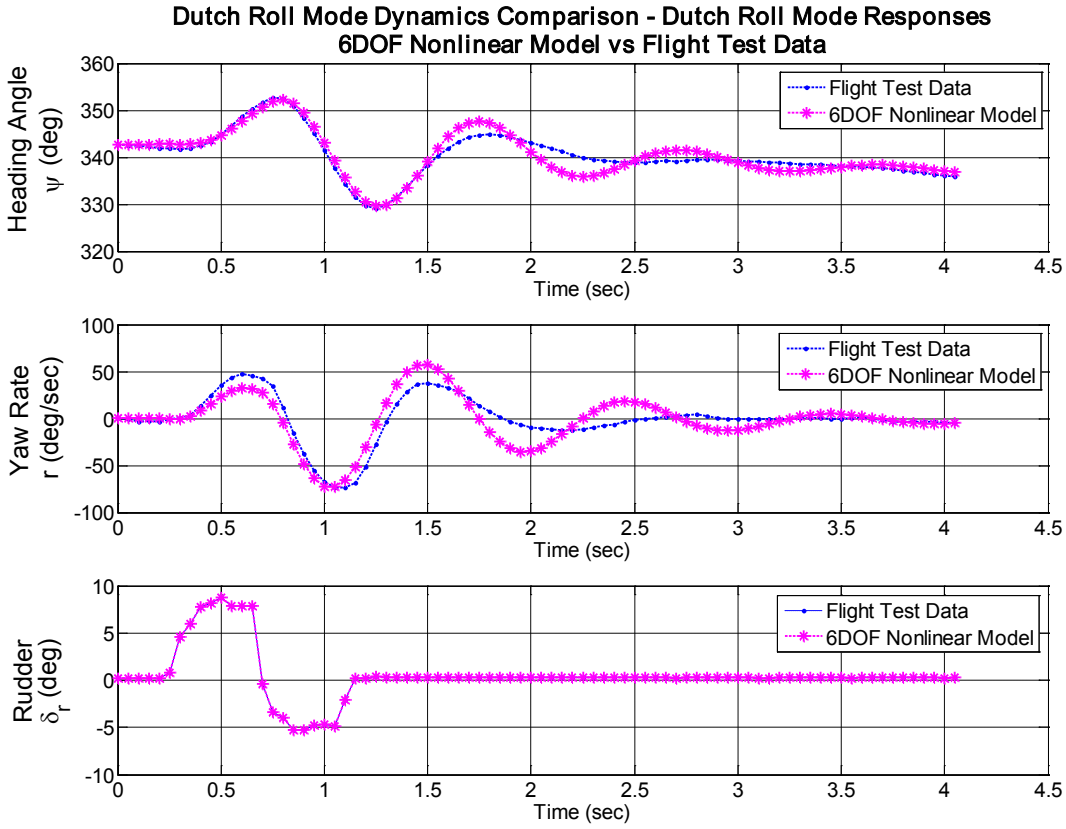

Figure 7-5. Dutch Roll Dynamics Comparison – Yaw Axis Response

Table 7-1 summarizes the peak values of the yaw rate outputs from the simulation and flight test data for the first, second, and third free responses after the rudder inputs were released. These data quantify the discrepancies seen between the flight test and the simulation responses in this Dutch roll mode test comparison. The differences are minor in the first free response but increase dramatically in the second and third free responses.

Table 7-1. Peak Yaw Rate Response Values for the Dutch Roll Mode Comparison

Peak Value of the Yaw Rate Response (deg/sec)			
Time Index (second)	Flight Test Value	6DOF Nonlinear Model Responses	
		Value	% Difference
≈ 1.5	37.16	57.63	55.09
≈ 2.0	-12.36	-35.32	185.76
≈ 2.4	4.515	18.47	309.08

Note: % difference is calculated w.r.t. the flight test value

The percentage difference in the simulation responses is calculated with respect to the flight test values. The formula used for this calculation is shown in Eq. 7-1. It is followed by an example of the calculation for the first peak value indicated at time index 1.5 second.

$$\begin{aligned} \%\ Difference &= \frac{6DOF\ \ Value - Flight\ \ Test\ \ Value}{Flight\ \ Test\ \ Value} \times 100\% \\ &= \frac{57.63 - 37.16}{37.16} \times 100\% \\ &= 55.09\% \end{aligned} \qquad \textbf{Eq. 7-1}$$

A derivative tuning technique is now introduced. Because it is known that some of the derivatives have the greatest impact on specific mode dynamics, it is possible to tune the values of those derivatives to adjust the dynamic responses until performance goals are satisfied. The damping ratio of the Dutch roll mode is most affected by the yaw-damping derivative Cn_r. The value of the Cn_r derivative is -0.1156. To increase the damping, a bigger magnitude for Cn_r is needed so that a greater yawing moment is generated in the opposite direction to

quickly correct the oscillation in the yaw rate. The Cn_r was incrementally changed in a 10% interval to evaluate the new Dutch roll mode responses, and the best modification was achieved when the Cn_r was increased by 80%. The new simulation is shown in Figure 7-6.

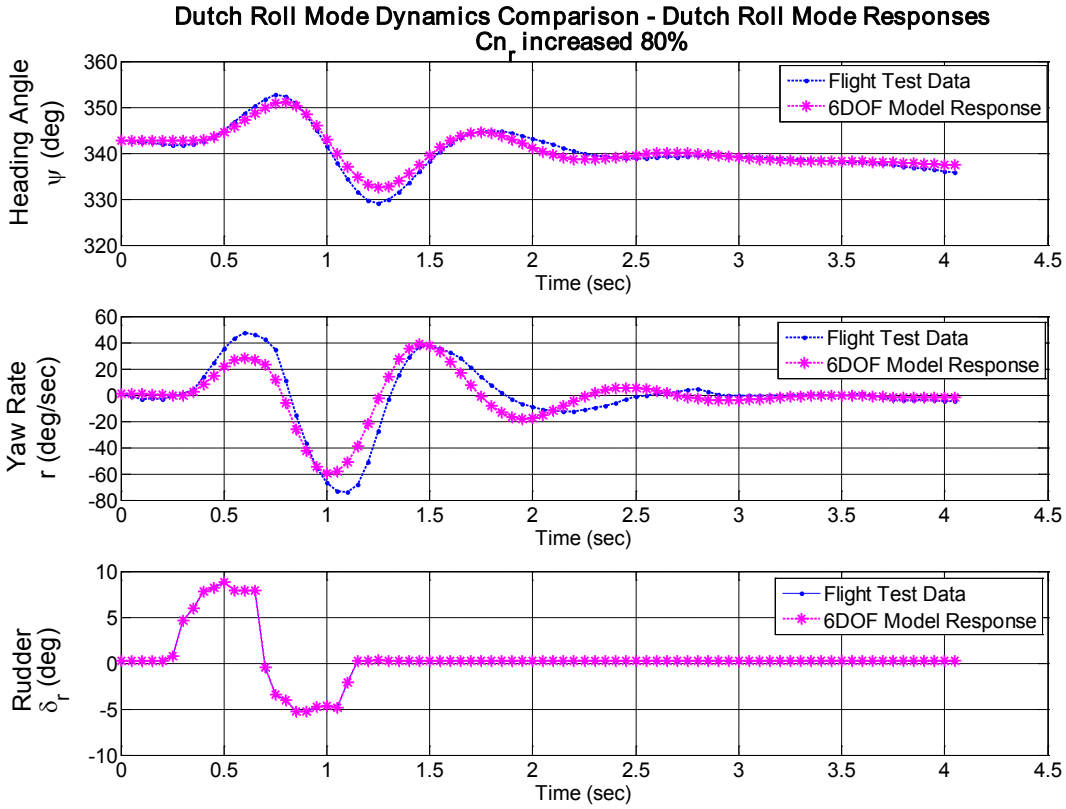

Figure 7-6. Dutch Roll Dynamics Response - with Cn_r Increased

By increasing Cn_r to 80%, the free responses of the yaw rate output given from the 6DOF model now matches the flight test results more closely. However, the magnitudes of the first two oscillations became smaller due to the change in Cn_r. These two responses are driven by the rudder control input when the rudder

is activated, which is most affected by the control power derivative $Cn_{\delta r}$. It needs to be tuned in order to compensate for the change in Cn_r. In fact, different aspects of the yaw rate response are affected by both the Cn_r and $Cn_{\delta r}$ derivatives. Thus an iterative process is required to tune each of these derivatives until satisfactory response performance is achieved.

To proceed with the iterative tuning process, the damping derivative is first adjusted incrementally to match the flight test data. In this case, Cn_r was first increased by 80%. The control derivative, $Cn_{\delta r}$, was then tuned in 10% intervals to correlate the impact of the change in Cn_r on the first two oscillatory responses. However, the change in $Cn_{\delta r}$ then affected the damping ratio of the system so that Cn_r required adjustments in 10% increments to compensate for the change in $Cn_{\delta r}$. Note that the changes in Cn_r and $Cn_{\delta r}$ are always done individually in a sequential manner. As illustrated in Figure 2-1, the tuning cycle repeats for every change in Cn_r and $Cn_{\delta r}$. The new results were compared with the flight test data until the closest match between the simulation responses and the flight test results were obtained.

After several iterative tuning cycles, the best match between the simulation and the flight test data was achieved using values of Cn_r increased by 150% and $Cn_{\delta r}$ increased by 40%. The new simulation responses, as shown in Figure 7-7, indicate that the damping responses of the Dutch roll dynamics have been improved, and the differences in the peak values, as shown in Table 7-2, were reduced significantly. This result successfully demonstrates that by using

this derivative tuning technique, it is feasible to refine the simulation model to achieve better performance.

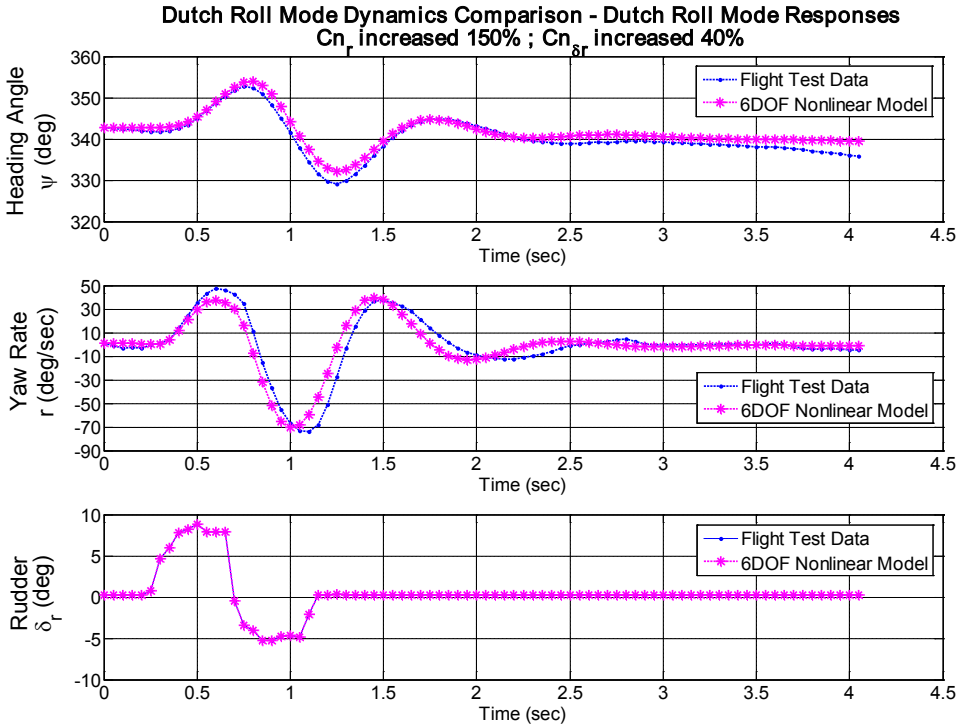

Figure 7-7. Dutch Roll Dynamics Comparison – with Cn_r and $Cn_{\delta r}$ Increased

Table 7-2. Peak Yaw Rate Response Values with the Modified Derivatives

Peak Value of the Yaw Rate Response (deg/sec) ***Cn_r increased 150%; $Cn_{\delta r}$ increased 40%***					
Time Index (second)	Flight Test Value	6DOF Nonlinear Model Responses			
		Before Tuning		After Tuning	
		Value	% Difference	Value	% Difference
≈ 1.5	37.16	57.63	55.09	39.93	7.45
≈ 2.0	-12.36	-35.32	185.76	-13.17	6.55
≈ 2.4	4.515	18.47	309.08	2.844	-37.01

Note: % difference is calculated w.r.t. the flight test value

Through the process of tuning the derivatives, the yaw rate response comparison was completed. The validation process continued to compare other sets of data such as the body rate, Euler angles, and acceleration data. These comparisons were given from the simulation model updated with the modified derivative values. Figure 7-8 shows the comparison of the body rate responses for this Dutch roll mode test.

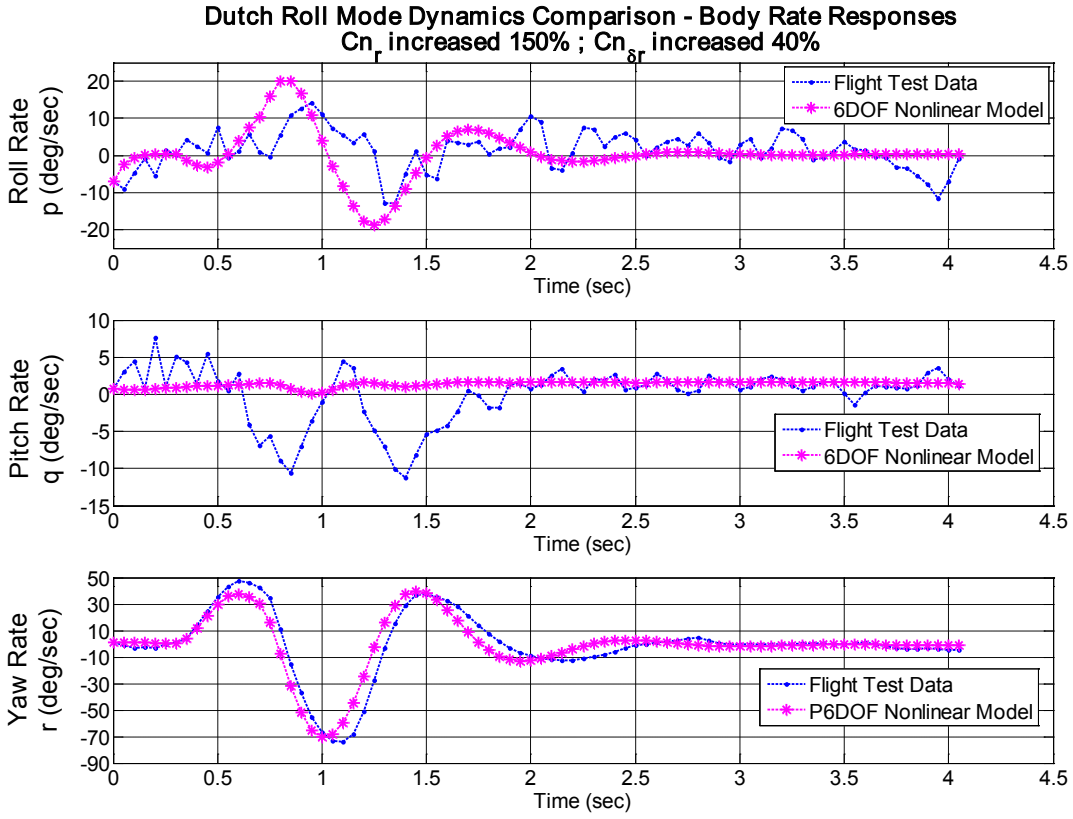

Figure 7-8. Dutch Roll Dynamics Comparison – Body Rate Response

The roll rate responses indicate that the coupling effect on the roll dynamics due to yaw is overestimated by the 6DOF nonlinear model. During a Dutch roll response, a sideslip angle was introduced due to the oscillation in the yaw direction. The roll response was generated due to this sideslip angle effect. Therefore, the roll and yaw coupling dynamics are mainly determined by the dihedral derivative Cl_β.

Using the derivative tuning process, the Cl_β derivative was tuned. Since the response magnitude is overestimated, the magnitude of the derivative should decrease. The Cl_β was adjusted incrementally in 10% intervals, and the best result was reached when Cl_β was decreased by 30%. The new simulation response is shown in Figure 7-9.

The peak values of the roll rate response are compared before and after the change in Cl_β, and the results are summarized in Table 7-3. Note that only the first two oscillations are considered in this comparison, because the flight test data was quite noisy after this point. The comparison shows that the coupling effect between roll and yaw has been reduced successfully using a smaller value of Cl_β. The average improvement is about 30%.

In the ideal case with no disturbances, the pitch rate response in a Dutch roll mode test should remain close to the trim condition. From the Euler angle responses shown in Figure 7-10, the 6DOF nonlinear model successfully demonstrated this performance. The mismatch of the bank angle may be due to disturbances during the flight test.

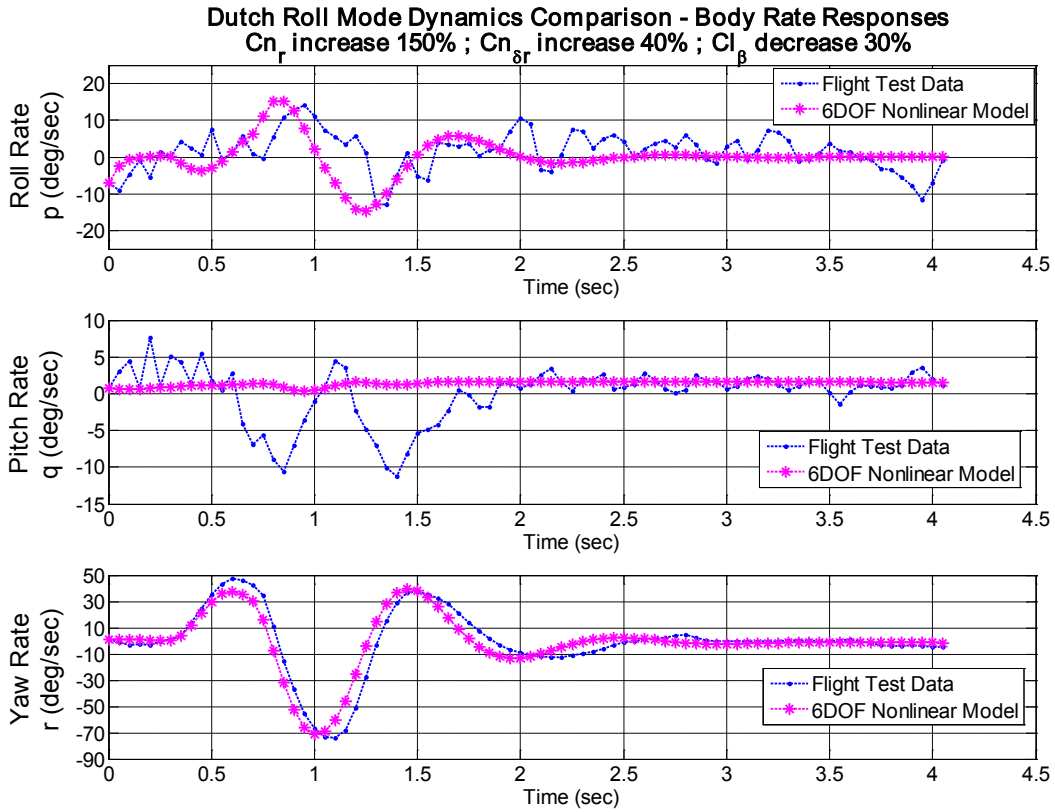

Figure 7-9. Dutch Roll Dynamics Comparison – with Cl_β Decrease

Table 7-3. Comparison of the Roll Rate Response in a Dutch Roll Mode Test

Peak Value of the Roll Rate Response in a Dutch Roll Mode Test (deg/sec) ***Cn_r increased 150%; $Cn_{\delta r}$ increased 40%; Cl_β decreased 30%***					
Time Index (second)	Flight Test Value	6DOF Nonlinear Model Responses			
		Before Tuning the Cl_β		After Tuning the Cl_β	
		Value	% Difference	Value	% Difference
0.85	14.24	20.07	40.94	15.17	6.53
1.25	-12.98	-18.78	44.68	-14.65	12.87

Note: % difference is calculated w.r.t. the flight test value

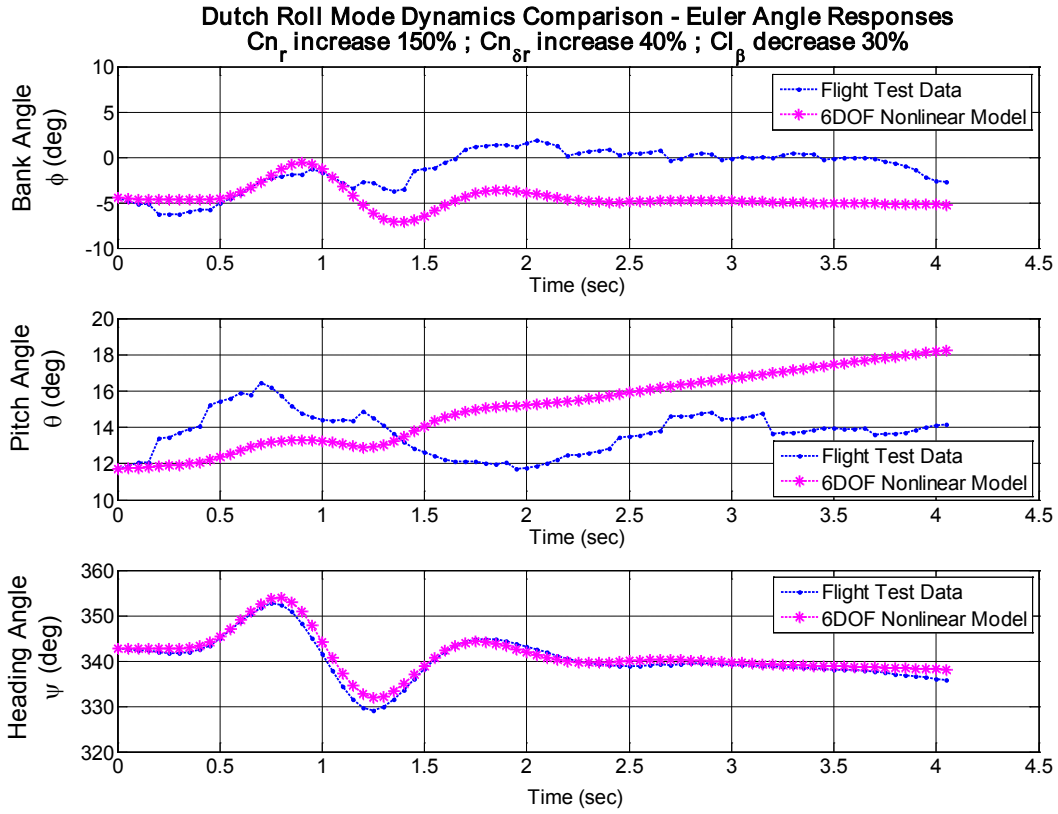

Figure 7-10. Dutch Roll Dynamics Comparison – Euler Angle Responses

Figure 7-11 shows the comparison of the acceleration data for this Dutch roll mode test. Overall, the 6DOF model provides fairly good estimates of the acceleration in each axis. The mismatch between the Z-axis data is seen again at the initial condition due to the assumption w.r.t. the AOA value used for the simulation. The overestimated thrust force issue is also observed in the X-axis acceleration data.

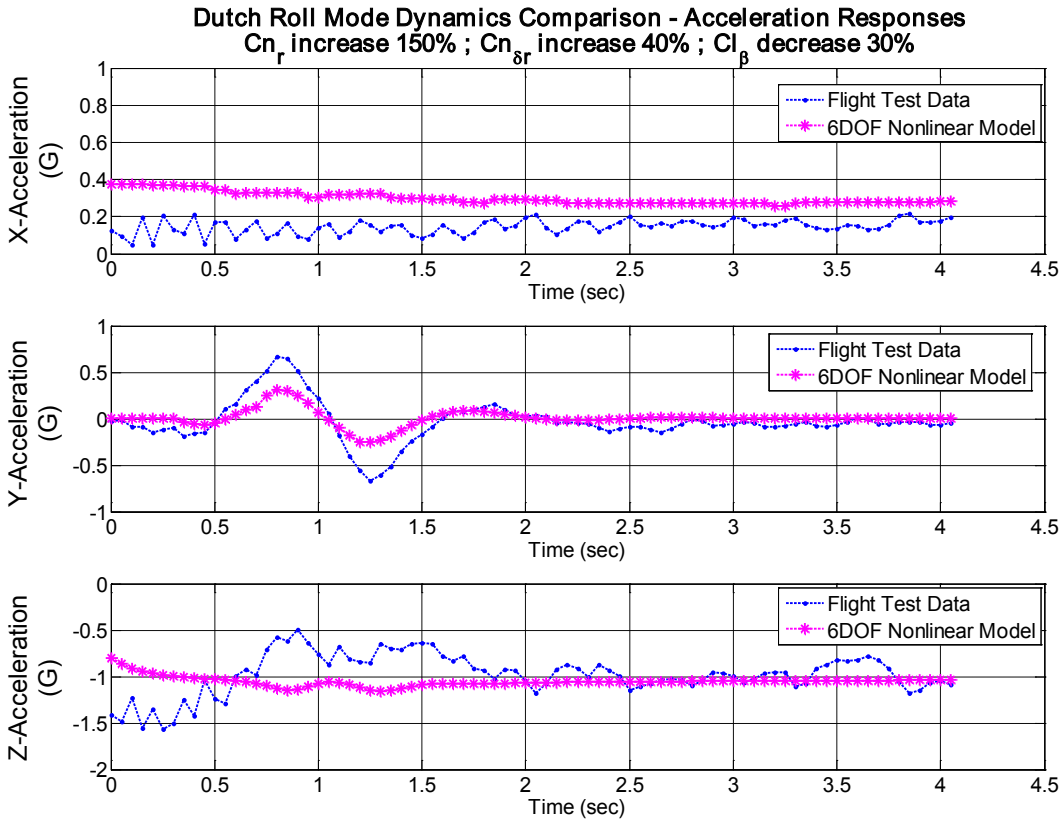

Figure 7-11. Dutch Roll Dynamics Comparison – Acceleration Data Responses

7.3 Validation of Short Period Responses

In this section, the validation of the short period mode's dynamics are presented. The flight test data from the short period Test I, as presented in Figure 5-7, is selected to evaluate the simulation results. The first comparison of the short period dynamics is shown in Figure 7-12.

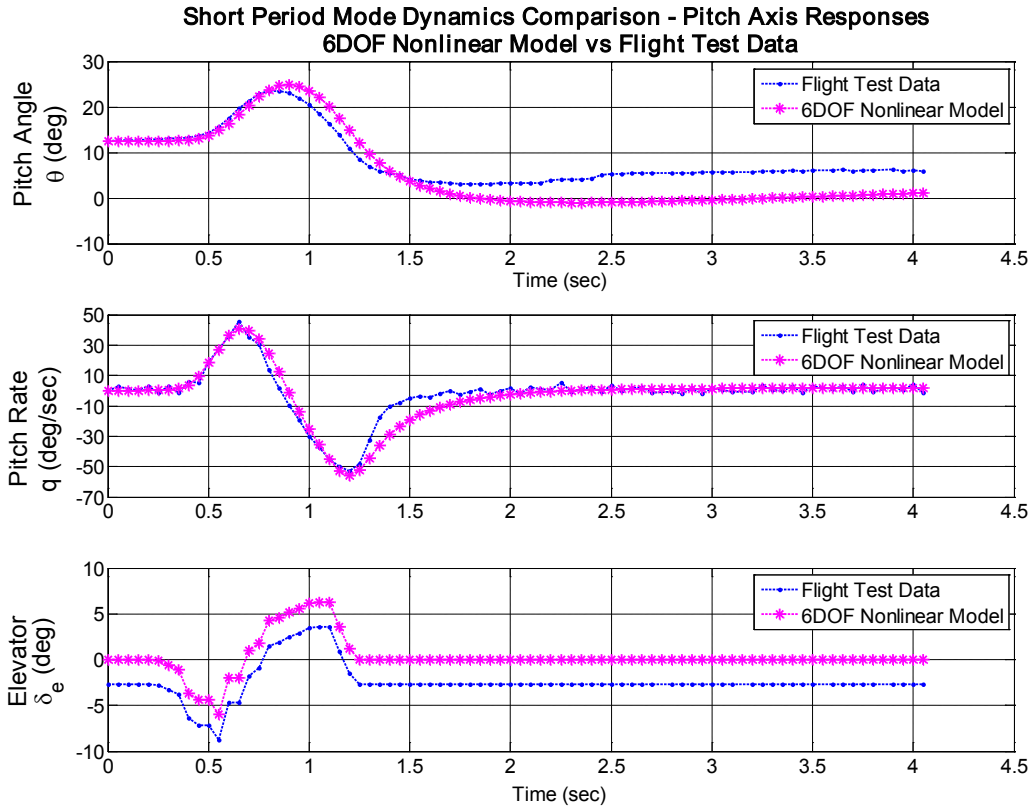

Figure 7-12. Short Period Dynamics Comparison – Pitch Axis Responses

The pitch rate responses shown in Figure 7-12 demonstrate very good damping characteristics using both simulation and flight test data. The damping from the 6DOF nonlinear model, however, was not as great as seen in the flight test responses. In addition, the slope of the first oscillation in response to the elevator input was slightly greater than seen in flight test. As a result, an overshoot in the pitch angle was introduced by the 6DOF model. After the elevator input was released, the pitch angle values drifted away from the flight test data. It is more likely due to the Phugoid mode.

To improve the short period mode dynamics, the derivative tuning technique is applied here. In this case, the pitch damping derivative Cm_q and the control power derivative $Cm_{\delta e}$ are adjusted, as the pitch damping response is most affected by Cm_q. The control derivative $Cm_{\delta e}$ is also required for tuning because the pitch rate response is affected by both the Cm_q and $Cm_{\delta e}$ derivatives. This is similar to the tuning procedures for the Dutch roll mode. Following the iterative tuning process as applied before, the best simulation performance was achieved with Cn_r increased 100% and $Cn_{\delta r}$ increased 40%. The new simulation responses are shown in Figure 7-13.

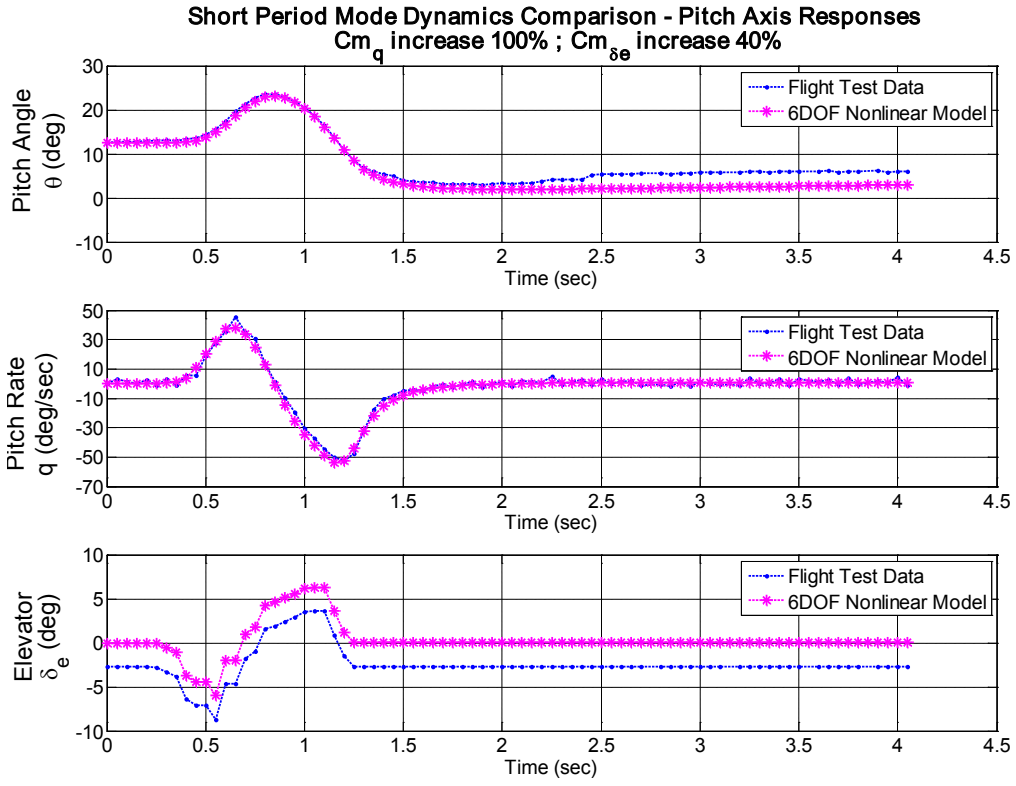

Figure 7-13. Pitch Dynamics Response Comparison – with Cm_q and $Cm_{\delta e}$ Increased

Using the new derivative values, the pitch rate simulation response now more closely matches the flight test data. Its damping action now corresponds to the real flight dynamics. As the accuracy of the pitch rate response improves, so does the pitch angle response. The steady state errors in the pitch angle data are also reduced after tuning the derivative values.

To quantify the change in simulation performance, the peak values from the first two pitch rate responses and the steady state of the pitch angle are compared before and after the modifications to the derivatives. The summary of this comparison is shown in Table 7-4. It reveals that the errors in the simulation results have been reduced effectively after the tuning process.

Table 7-4. Comparison of the Pitch Responses in a Short Period Mode Test

Peak Value of the Pitch Rate Response in a Short Period Mode Test (deg/sec) ***Cm_q increase 100%; $Cm_{\delta e}$ increase 40%***					
Time Index (second)	Flight Test Value	6DOF Nonlinear Model Responses			
		Before Tuning		After Tuning	
		Value	% Difference	Value	% Difference
0.65	45.33	40.65	-10.32	38.15	-15.84
1.2	-52.62	-56.06	6.54	-53.77	2.19
Steady State Value of the Pitch Angle Response (deg)					
4.05	5.964	1.139	-80.90	2.999	-49.71

Note: % difference is calculated w.r.t. the flight test value

The comparison of the body rate and the Euler angle responses are shown in Figure 7-14 and Figure 7-15, respectively, using the simulation model updated with the new derivative values.

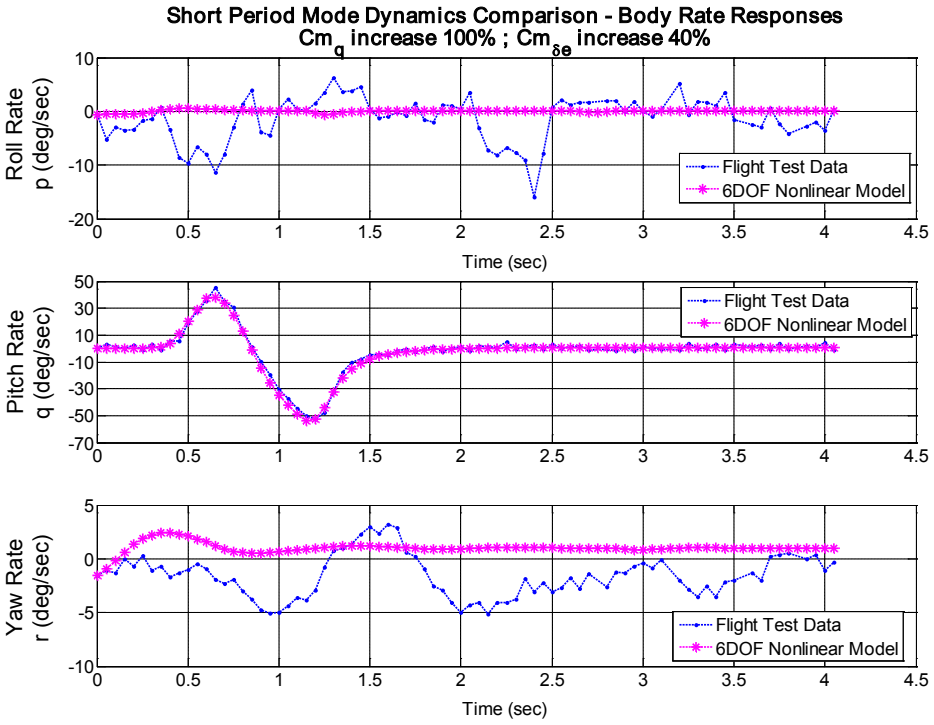

Figure 7-14. Short Period Dynamics Comparison – Body Rate Responses

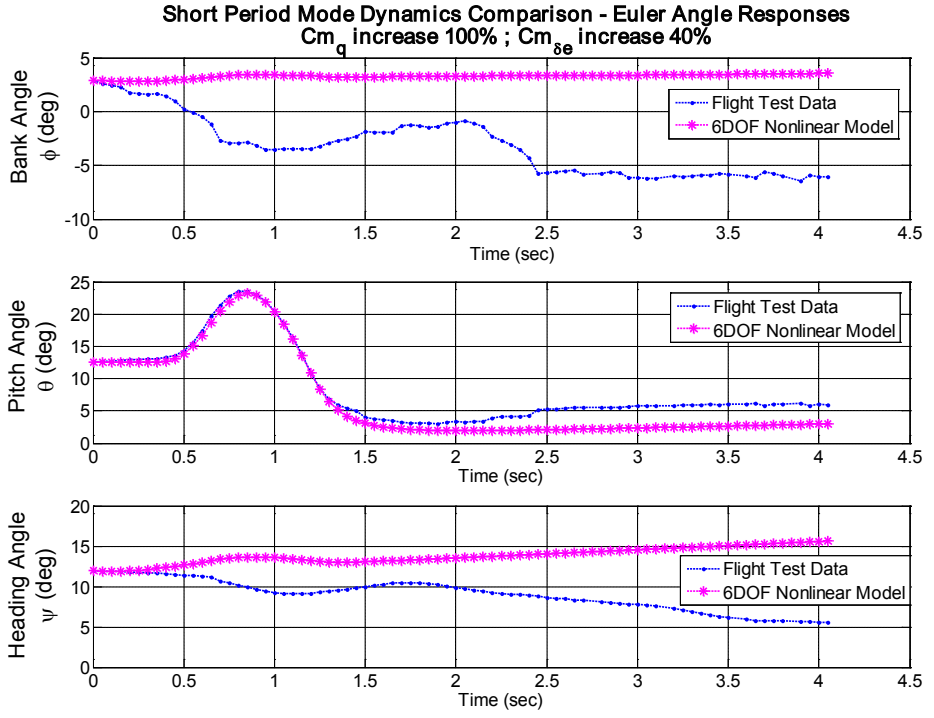

Figure 7-15. Short Period Dynamics Comparison – Euler Angle Responses

A yaw rate oscillation in the flight test data was seen that interacted with the roll dynamics. It was confirmed that no aileron or rudder inputs were commanded during this test. It is reasonable to infer that the lateral-directional responses were most likely caused by the wind, which will not be shown in the simulation responses as the current simulation model does not incorporate any disturbances.

If one assumes a no wind condition, the aircraft should remain in a straight and level flight condition after the short period mode's oscillation has finished. This concurs with the responses obtained from the simulation model. The final validation for the short period mode is the comparison of the acceleration data, shown in Figure 7-16.

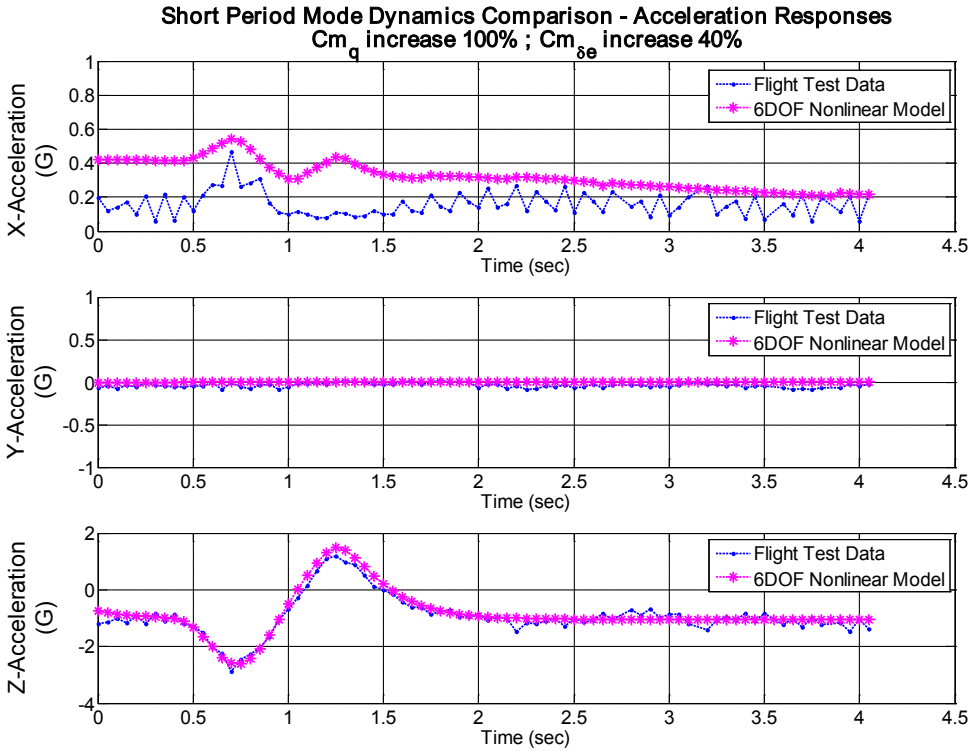

Figure 7-16. Short Period Dynamics Comparison – Acceleration Data Responses

From the comparison of the acceleration data, the Y-axis and Z-axis responses demonstrate an excellent match between the 6DOF simulation model and the flight test data. This implies that the estimates of the lift force and the sideforce are very accurate. The trend in the X-axis response is similar to that seen in flight test, with some offsets seen at the beginning of the response. As discussed before, the error could be introduced by the thrust model and the uncertain values for AOA.

7.4 Validation of Phugoid Mode Responses

As discussed in Section 5.2.4, two incomplete Phugoid mode flight tests were conducted. Although a complete cycle of the Phugoid mode dynamics is not available, the flight test data are used to validate the airspeed and altitude simulation responses over a long simulation time. The 6DOF model is updated with all the recently changed derivative values. The Phugoid mode test I data, presented in Figure 5-10, is chosen to evaluate the Phugoid mode dynamics. Figure 7-17 shows the comparison of the Phugoid mode responses, and its corresponding acceleration responses are shown in Figure 7-18.

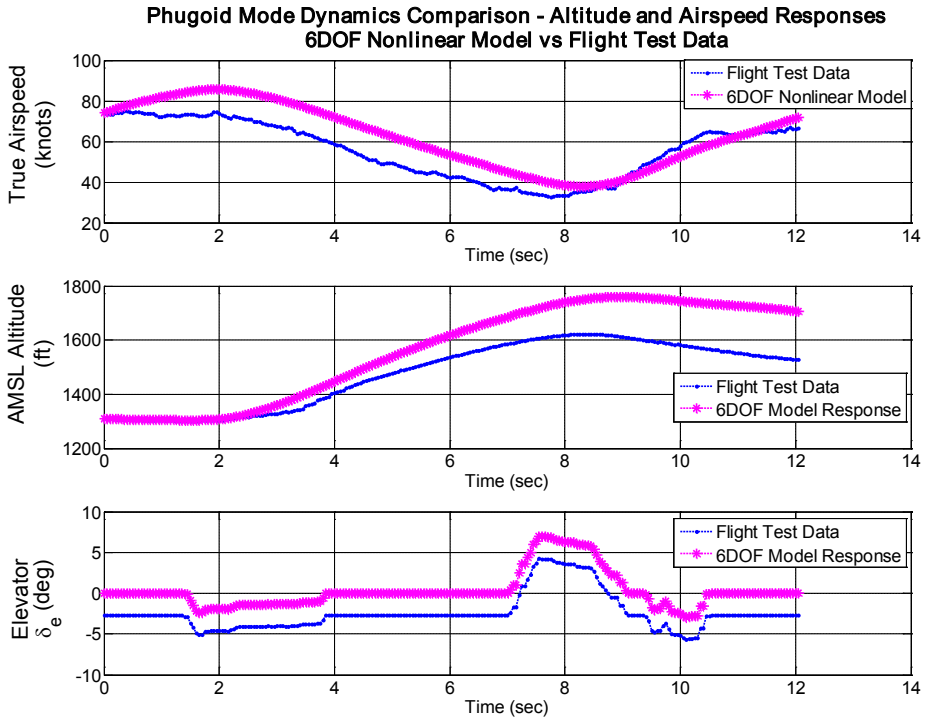

Figure 7-17. Phugoid Dynamics Comparison – Altitude and Airspeed Responses

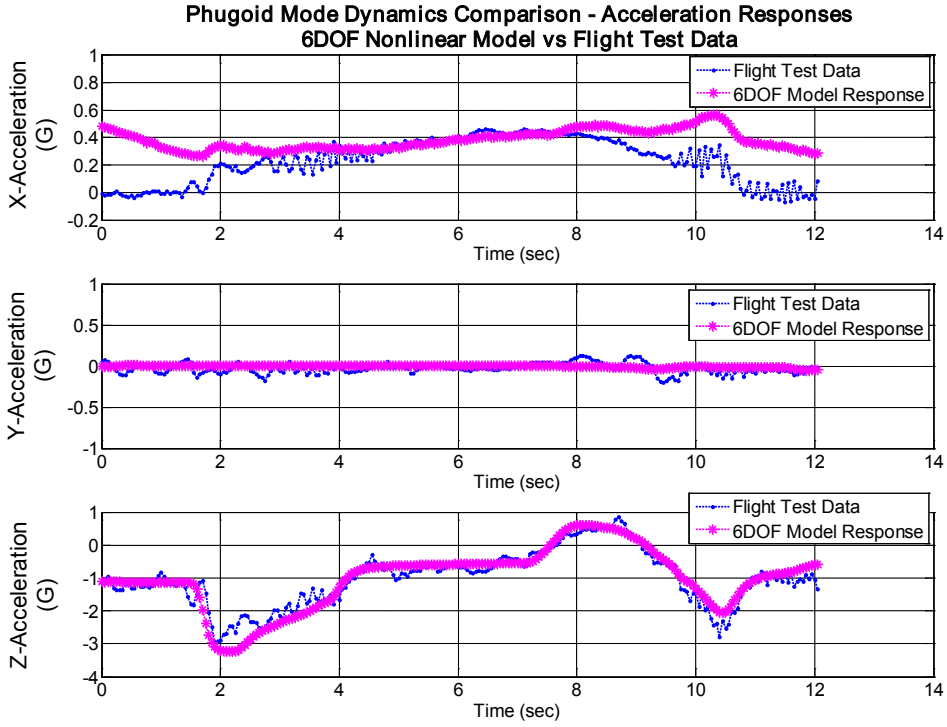

Figure 7-18. Phugoid Dynamics Comparison – Acceleration Data Responses

Overall, the simulation responses tend to follow the trend in the flight test results but with some differences. The current 6DOF model does not provide sufficient accuracy in predicting airspeed and altitude changes. This is due to:

- The variation in airspeed during the Phugoid mode test about the trim speed (70 knots) is too high. Recall that the 6DOF nonlinear model was built using the derivatives calculated at the 70 knot trim speed condition. The simulation model is no longer an accurate way to predict the aircraft's dynamics when the flight condition is far from the trim condition. In this Phugoid mode test, the airspeed varied from 70 knots down to 40 knots.
- The variation in airspeed and altitude are coupled. These dynamics are mainly controlled by the elevator and throttle commands. Currently, a simplified engine model is implemented to estimate the thrust forces. This simplified estimation may result in an inaccurate prediction of airspeed, which will couple with the altitude response and vice versa. This error will build with time, making the simulation response less accurate for a long simulation run time.

7.5 Summary of the 6DOF Model Validation Results

Examining the validation results for each mode's dynamics, the following summary can be made:

- The 6DOF nonlinear model shows very promising performance in duplicating the roll mode, Dutch roll mode, and short period mode dynamics.
- The 6DOF model gives a very accurate prediction of the coupling effects between the longitudinal and lateral-directional dynamics.
- It has been demonstrated that the derivative tuning technique is capable of improving the accuracy of the simulation model.
- The lift and sideforce components estimated by the 6DOF model are shown to be very accurate in every dynamic mode comparison.
- The X-axis force is overestimated by the 6DOF model due to the overestimated thrust forces. This is mostly caused by the use of a simplified engine model.
- Due to the lack of different stability derivatives at the different trim speeds and the low fidelity of the engine model, the current 6DOF nonlinear model does not provide sufficient accuracy to predict the variation in the airspeed and altitude responses.

Throughout the validation process, five derivatives are adjusted in the Dutch roll mode and short period mode comparison. The changes to the derivatives are compared with the initial values estimated from each modeling method and are listed in Table 7-5.

Table 7-5. Summary of Modifications to Derivatives

Derivatives	*AAA*	*AVL [9]*	*Final*	*% Difference w.r.t. AAA*	*% Difference w.r.t. AVL*
Cn_r	-0.1270	-0.1156	-0.2890	130	150
$Cn_{\delta r}$	-0.0996	-0.1003	-0.1404	40	40
Cl_β	-0.0266	-0.0314	-0.0220	-20	-30
Cm_q	-8.0532	-4.3732	-16.1064	100	270
$Cm_{\delta e}$	-0.8778	-0.7572	-1.2289	40	60

It is seen that some of the derivatives have been adjusted for more than 100% in order to match the flight test data. This implies that the estimation errors from the modeling method are quite large for some of the stability derivatives. Table 7-5 shows that the overall estimation errors from the AAA method are smaller than the AVL method. It is especially true for those two longitudinal derivatives Cm_q and $Cm_{\delta e}$. Appendix E shows the prediction accuracy of stability derivatives using the AAA method. The final change in Cl_β is closely matched with the AAA's prediction accuracy. The change in Cn_r and Cm_q, however, is larger than seen in Appendix E. This difference could be introduced due to the operation of the vehicle at a low Reynolds number [54]. The AAA program is

designed to be used at a minimum Reynolds number of 2.96 x 10^6. For the Yak-54 RC model, it is operated at a Reynolds number of 1.09 x 10^6.

The final values of the derivatives are applied to update the state space linear model so that the mode dynamics can be recalculated using eigenvalue analysis. The new modal analysis is then compared with the original results. Additional research using the system identification technique [16] was conducted using the identical flight test data, and the results [55] are listed here for comparison. All the comparisons are summarized in Table 7-6.

Table 7-6. Comparison Between New and Old Models and Flight Test Results

Model &Analysis Method	*Lateral Dynamics*				*Longitudinal Dynamics*			
	Spiral	*Roll*	*Dutch Roll*		*Short Period*		*Phugoid*	
	τ_s *(sec)*	τ_r *(sec)*	ξ	ω_n *(rad/s)*	ξ	ω_n *(rad/s)*	ξ	ω_n *(rad/s)*
AAA Model	-86.96	0.06	0.19	6.88	0.90	9.42	0.42	0.27
Flight Test Results	----	----	0.27	5.70	1.00	16.62	----	< 0.19
New Model Results	-202.83	0.04	0.36	7.04	0.98	11.6	0.53	0.22
System ID Results	----	----	0.30	----	----	----	0.57	----

The new damping ratio for the Dutch roll mode is now identified as 0.36, which is 90% higher than before. This is 33% higher than determined from the flight test data. Figure 7-7 has clearly demonstrated that the new model is closer to the true dynamics. This implies that the data reduction process involves some level of error due to the use of graphical techniques. According to the system

identification analysis results [55], the damping ratio for the Dutch roll mode is determined as 0.30 with 77% accuracy, which closely matches the analysis results given from the new model.

The newly determined damping ratio for the short period mode is 0.98, which is 7.2% higher than before. This is reasonable, as the actual dynamics from the flight test demonstrates a very highly damped response, which could be considered a critically damped response. For a critically damped system, its damping ratio is equal to 1.0 [33].

The new model also shows faster roll dynamics than the initial model. As demonstrated in Figure 7-1, the new model closely matches the flight test roll dynamics. It implies that the roll mode is underestimated using the initial AAA values

For the Phugoid mode dynamics, the new model analysis shows a very close match with the system identification results. A change in the spiral mode dynamics is also introduced by the new model. Because the stability of the spiral mode is mostly affected by both the yaw damping derivative Cn_r and the dihedral derivative Cl_β, the dynamics of the spiral mode is affected by the changes to these two derivatives. The new Yak-54 model has a slower unstable spiral mode than before.

8 Conclusions, Recommendations, and Future Work

8.1 Conclusions

As a result of the modeling, simulation, flight testing, and validation processes on a one-third scale Yak-54 platform documented in this thesis, the following conclusions can be made:

- The AAA method may be used to generate preliminary estimates of the stability and control derivatives.
- Large prediction errors w.r.t. the derivative values may be introduced by AAA when it is used for analysis in the low Reynolds number range.
- Flight tests of open loop dynamics flight tests should be conducted and the flight test data should be used to refine the model dynamics using the derivative tuning technique.
- Errors are introduced from the data reduction process due to the use of graphical techniques.
- Overall, the estimation errors from the AAA method are smaller than the AVL method. It is especially true w.r.t. longitudinal derivatives.

- The 6DOF nonlinear model provides very promising performance in simulating the dynamics of the roll mode, the Dutch roll mode, and the short period mode.

8.2 Recommendations

The following recommendations can be made based on the 6DOF simulation model validation restuls:

- The engine model needs to be improved to increase the accuracy of the thrust force estimates.
- Multiple sets of derivatives at different speeds should be implemented to enhance the nonlinearity of the aerodynamics model to capture variations with flight condition.
- The flight test data should be filtered to minimize noise components before being compared to the simulation data.
- The sum of squared errors method should be used to quantify the performance difference before and after the derivative tuning process.
- A computer program should be developed to automatically tune the derivative values by minimizing the sum of squared errors between the flight test and simulation results.

8.3 Future Work

Based on the current status of this research, suggestions can be made to extend the scope of this research work. These suggestions are:

- The USAF digital DATCOM program [32] should be used as another modeling method to potentially improve the models used in this research.
- The Vortex code written by Professor Chuan-Tau Lan should be evaluated as another modeling technique.
- Wind tunnel testing or a CFD method should be used to enhance the fidelity of the aerodynamics model.
- A complete system identification flight test approach should be developed to identify the derivative values directly from flight test for dynamics model improvement.
- The modeling, flight testing, simulation, and validation process should be duplicated for other RC airplane platforms to investigate the validity of the AAA method for low Reynolds number applications.
- The 6DOF model can be interfaced with other existing autopilot systems to develop a hardware-in-the-loop simulation platform.
- A flight control system can be built using the 6DOF model in MATLAB/Simulink to evaluate the performance of the simulation for flight control system design applications.
- The 6DOF model can also be used in full-size, manned aircraft.

9 References

1. Center of Remote Sensing of Ice Sheets Research Institute, Lawrence, KS, URL: http://www.cresis.ku.edu [cited 19 September 2008].

2. Bernstein, L., Bosch, P., et. al., "Climate Change 2007: Synthesis Report. Summary for Policy Markers," *Intergovernmental Panel on Climate Change* [online publication], URL: http://www.ipcc.ch/pdf/assessment-report/ar4/syr/ar4_syr_spm.pdf [cited 20 August 2008].

3. Donovan, W. R., "The Design of an Uninhabited Air Vehicle for Remote Sensing in the Cryosphere," Master's Thesis, Department of Aerospace Engineering, The University of Kansas, Lawrence, KS, 18 December 2007.

4. Donovan, W. R., "CReSIS UAV Critical Design Review: The Meridian," Technical Report 123, Center for Remote Sensing of Ice Sheets, The University of Kansas, Lawrence, KS, 25 June 2007.

5. Underwood, S., "Performance and Emission Characteristics of an Aircraft Turbo diesel Engine using JET-A Fuel," Master's Thesis, Department of Aerospace Engineering, The University of Kansas, Lawrence, KS, 05 May 2008.

6. Burns, R., "A Low-Cost Modular Avionics and telemetry Software System for the CReSIS Meridian Uninhabited Aerial System," 27th Digital Avionics Systems Conference, St. Paul, MN, 26-31 October 2008

7. Jager, R., "Test and Evaluation of the Piccolo II Autopilot System on a One-Third Scale Yak-54," Master's Thesis, Department of Aerospace Engineering, The University of Kansas, Lawrence, KS, 30 April 2008.

8. Esposito, J., "Time Plotting Framework for Remote Display of Flight Data," 27th Digital Avionics Systems Conference, St. Paul, MN, 26-31 October 2008.

9. Leong, H. I., "Modeling and Simulation for the Yak-54 using a 6DOF Model with Flight Test Validation," Technical Report, Center for Remote Sensing of Ice Sheets, The University of Kansas, Lawrence, KS, 30 November 2008.

10. Ly, U. L., Higashino, S. I., "Development of a UAV Flight-Test Vehicle at The University of Washington," *AIAA Unmanned Unlimited Systems, Technologies, and Operations*, San Diego, CA, 15-18 September 2003.

11. Anderson, J. D., and Wendt, J. F., *Computational Fluid Dynamics: An Introduction*, 2nd ed., Springer-Velag, New York, 1996.

12. Anderson, J. D., *Computational Fluid Dynamics: The Basics with Applications,* McGraw Hill Inc., 1995.

13. Tinoco, E. N., "Validation and Minimizing CFD Uncertainty for Commercial Aircraft Applications," *AIAA Applied Aerodynamics Conference*, Honolulu, HI, 18-21 August 2008.

14. Yuzuru, Y., Mitsuhiro, M., Takeshi, I., and Kazuomi, Y., "Experiment and CFD of a High-lift Configuration Civil Transport Aircraft Model," *AIAA Aerodynamic Measurement Technology and Ground Testing Conference*, San Francisco, CA, 5-8 June 2006.

15. Smetana, F. O., Summey, D. C., and Johnson, W. D., "Flight Testing Techniques for the Evaluation of Light Aircraft Stability Derivatives," NASA CR-2016, NASA, Washington, D.C., May 1972.

16. Jategaonkar, R., *Flight Vehicle System Identification: A Time Domain Methodology*, 1st ed., AIAA Education Series, Reston, VA, 2006.

17. Tishler, M. B., and Remple, R. K., *Aircraft and Rotorcraft System Identification: Engineering Methods with Flight Test Examples*, AIAA Education Series, Reston, VA, 2006.

18. Lee, Y., Kim, S., Suk, J., Koo, H., and Kim, J., "System Identification of an Unmanned Aerial Vehicle from Automated Flight Tests," *AIAA's 1st Technical Conference and Workshop on Unmanned Aerial Vehicles*, Portsmouth, VA, 20-23 May 2002.

19. Bhandari, S., and Colgren, R., "14-DoF Linear Parameter Varying Model of a UAV Helicopter Using Analytical Techniques," *AIAA Modeling and Simulation Technologies Conference and Exhibit,* Honolulu, HI, 18-21 August 2008.

20. Tischler, M. B., and Cauffman, M. G., "Frequency-Response Method for Rotorcraft System Identification: Flight Applications to BO 105 Coupled Rotor/fuselage Dynamics," *Journal of American Helicopter Society*, July 1992.

21. Jung, D., and Tisotras, P., "Modeling and Hardware-in-the-Loop Simulation for a Small Unmanned Aerial Vehicle," *AIAA Infotech Aerospace Conference,* Rohnert Park, CA, 7-10 May 2007.

22. Sadraey, M., and Colgren, R., "UAV Flight Simulation: Credibility of Linear Decoupled vs. Nonlinear Coupled Equations of Motion," *AIAA Modeling and Simulation Technologies Conference,* San Francisco, CA, 15-18 August 2005.

23. Jodeh, N. M., Blue, P. A., and Waldron, A. A., "Development of Small Unmanned Aerial Vehicle Research Platform: Modeling and Simulating with Flight Test Validation," *AIAA Modeling and Simulation Technologies Conference*, Keystone, CO, 22-24 August 2006.

24. Advanced Aircraft Analysis, Software Package, Version 3.1, DAR Corporation, Lawrence, KS.

25. Stevens, B. L., and Lewis, F. L., *Aircraft Control And Simulation*, 2nd edition, John Wiley & Sons, Hoboken, NJ, 2003.

26. Phillips, W. F., *Mechanics of Flight*, John Wiley & Sons, Hoboken, NJ, 2004.

27. Pamadi, B. N., *Performance, Stability, Dynamics, and Control of Airplanes*, 2nd edition, AIAA Education Series, Reston, VA, 2004.

28. Roskam, J., *Aircraft Flight Dynamics and Automatic Flight Controls (Part I)*, DAR Corporation, Lawrence, KS, 2003.

29. Ward, D. T., Strganac, T. W., *Introduction to Flight Test Engineering*, 2nd edition, Texas A&M University, 2001.

30. MATLAB/Simulink, Software Package, Version R2007a, The MathWorks Inc., Natick, MA, 2007.

31. DAR Corporation, Lawrence, KS, URL: http://www.darcrop.com/, [cited 20 August 2008].

32. Willams, J. E., and Vukelich, S. R., "The USAF Stability and Control DATCOM," Tech. Rep., AFFDL-TR-79-3032, McDonnell Douglas Astronautics Company, St Louis, MO, October 1979.

33. Katsuhiko, O., *Modern Control Engineering*, 4th edition, Prentice-Hall, Upper Saddle River, NJ, 2002.

34. AVL Aerodynamic Analysis, Software Package, Version 3.27, MIT, Boston, MA, URL: http://web.mit.edu/drela/Public/web/avl/ [cited 20 August 2008].

35. Roger, R. M., *Applied Mathematics in Integrated Navigation Systems*, 3rd edition, AIAA Education Series, Reston, VA, 2007.

36. McFarland, R. E., "A Standard Kinematic Model for Flight Simulation at NASA-AMES," NASA CR-2497, NASA, Washington, DC, January 1975.

37. "Aerospace Blockset 3 User's Guide," The MathWorks, Inc., Natick, MA, 2007.

38. Tandon, G. K., "Coordinate Transformations," *Spacecraft Attitude Determination and Control*, edited by J.R. Wertz, Kluwer Academic, Dordrecht, The Netherlands, 1978, pp. 760-766.

39. Euler, L., "Formulae Generales pro Translatione Quacunque Corporum Rigidorum," *Novi Commentari Accademiae Scientiraum Imperialis Petropolitance*, Vol. 20, 1775, pp. 189-207.

40. Broucke, R. A., "On the Use of Poincare Surfaces of Section in Rigid Body Motion," *Journal of Astronautical Sciences*, Vol. 41, No. 4, 1993, pp. 593-601.

41. Kolve, D. I., "Describing an Attitude," *Advances in the Astronautical Sciences, Proceedings of the 16th AAS Rocky Mountain Guidance and Control Conference*, Vol. 81, Univelt, pp. 289-303, San Diego, CA, 1993.

42. Cayley, A., "On Certain Results Relating to Quaternions," *Philosophical Magazine,* Vol. 26, No. 1, 1845, pp. 141-145.

43. Hamilton, W. R., "Quaternions: Or a New System of Imaginaries in Algebra," *Philosophical Magazine*, Vol. 25, No. 3, 1844, pp. 489-495.

44. Hamilton, W. R., *Lectures on Quaternions*, Hodges and Smith, Dublin, 1853, pp. 1-736.

45. Hamilton. W. R., *Elements of Quaternions,* Longmans, Green and Co., London, 1866, pp. 1-762.

46. Philips, W. E., and Hailey, C. E., "Review of Attitude Representations Used for Aircraft Kinematics," *AIAA Journal of Aircraft,* Vol. 38 No. 4, Reno, NA, 2008.

47. Cooke, J. M., Zyda, M. J., Pratt, D. R., and McGhee, R. B., "NPSNET Flight Simulation Dynamic Modeling Using Quaternions," *Presence*, Vol. 1, No. 4, pp. 404-420, 25 January 1994.

48. Icker, B. P., "A New Method for Performing Digital Control System Attitude Computations Using Quaternions," *AIAA Guidance, Control, and Flight Dynamics Conference*, Pasadena, CA, 12-14 August 1968.

49. Hitec Web Page, URL: http://www.hitecrcd.com/ [cited 20 August 2008].

50. 3W-Modellmotoren Web Page, URL: http://www.3w-modellmotoren.com/ [cited 01 December 2008].

51. Martin, H., "JavaProp – Design and Analysis of Propellers," Software Package, Version 1.39, URL: http://www.mh-aerotools.de/airfoils/javaprop.htm [cited 20 August 2008]

52. "Department of Defense World Geodetic System 1984, Its Definition and Relationship with Local Geodetic Systems," NIMA TR8350.2, 3rd ed., 3 January 2000.

53. "U.S. Standard Atmosphere, 1976," NASA-TM-X74335, National Oceanic and Atmospheric Administration, National Aeronautics and Space Administration, United States Air Force, Washington, DC, October 1976.

54. Anderson, J. D., *Fundamentals of Aerodynamics*, 4th ed., Mc Graw Hill, New York, 2007.

55. Keshmiri, S., Leong, H., Jager, R., Colgren, R., and Hale, R., "Modeling and Simulation of the Yak-54 Scaled Unmanned Aerial Vehicle Using Parameter and System Identification," *AIAA Atmospheric Flight Mechanics Conference and Exhibit*, Honolulu, HI, 18-21 August 2008.

Appendix A. Moment of Inertia Calculations

Summary of Calculations
Axis Conversion: (+X~upstream ; +Y~right wing; +Z~down)

Item	*Description*	*Means*	*Result*	*Units*
Gross Mass	weight of aircraft with full fuel	measured	26.8400	lbs
Empty Mass		measured		lbs
Xcg	Aircraft C.G. location at X -axis	calculated	-10.8857	in
Ycg	Aircraft C.G. location at Y -axis	calculated	0.0836	in
Zcg	Aircraft C.G. location at Z -axis	calculated	-0.0073	in
Ixx - Roll Inertia	moment of inertia w.r.t roll axis	calculated	1.0886	slug - ft^2
Iyy - Pitch Inertia	moment of inertia w.r.t. pitch axis	calculated	2.1068	slug - ft^2
Izz - Yaw Inertia	moment of inertia w.r.t. yaw axis	calculated	3.0382	slug - ft^2
Ixz Roll & Yaw coupled Inertia	moment of inertia w.r.t. roll and yaw coupleling axis	calculated		

CG Measurement of Fuselage Section
(full fuel, without wing, H-tail, spars, batteries, engine, propeller, spinner & avionics)
Axis Conversion: (+X~upstream ; +Y~right wing; +Z~down)

Item	*Description*	*Value*	*Unit*
W_RHS	weight on RHS wheel	4.58	lbs
W_LHS	weight on LHS wheel	4.64	lbs
W_Tail	weight on tail wheel	1.74	lbs
W_total	Total weight	10.96	lbs
X_MG	distance from main wheel to firewall	-4.50	in
X_TG	distance from tail wheel to firewall	-64.00	in
X C.G_fuselage	X C.G. location of fuselage w.r.t. firewall	-13.95	in

Equations used for the Moment of Inertia Calculations

Model Type	*Equations*	*Description*
Rod mass moment of inertia	$Ixx = m/12*L^2$	L = length
	$Iyy = m*r^2$	r= radius
	$Izz = Ixx = m/12*L^2$	
rectangular block	$Ixx = m/12*(y^2+z^2)$	x = dimension on x axis
	$Iyy = m/12*(x^2+z^2)$	y = dimension of y axis
	$Izz = m/12*(x^2+y^2)$	z = dimension on z axis
circular cone	$Ixx = 3/10*m*r^2$	r = radius
	$Iyy = Izz = 1/4*m*r^2$	

Moment of Inertia w.r.t. the Aircraft C.G.

Equations	*Description*
$Ixx\_c.g. = Ixx + m*(Y\_bar^2 + Z\_bar^2)$	X_bar = component C.M. location w.r.t. aircraft C.G. location on X-axis
$Iyy\_c.g. = Iyy + m*(X\_bar^2 + Z\_bar^2)$	Y_bar = component C.M. location w.r.t. aircraft C.G. location on Y-axis
$Izz\_c.g. = Izz + m*(X\_bar^2 + Y\_bar^2)$	Z_bar = component C.M. location w.r.t. aircraft C.G. location on Z-axis

Aircraft Components	Weight (lbs)	Moment due to Weight w.r.t. Datum			Moment due to Weight w.r.t. Datum		
		X - axis (in)	Y - axis (in)	Z - axis (in)	X - axis (in-lbs)	Y - axis (in-lbs)	Z - axis (in-lbs)
Fuselage Section	10.96	-13.9462	0.0000	0.0000	-152.8500	0.0000	0.0000
Wing_RHS	2.38	-15.3066	28.7118	0.2082	-36.4297	68.3341	0.4955
Wing_LHS	2.32	-15.3066	-28.7118	0.2082	-35.5113	-66.6114	0.4830
H tail_RHS	0.62	-55.1250	13.0000	-1.0000	-34.1775	8.0600	-0.6200
H tail_LHS	0.58	-55.1250	-13.0000	-1.0000	-31.9725	-7.5400	-0.5800
Wing spar	0.43	-10.6250	0.0000	0.7500	-4.5688	0.0000	0.3225
Rear spar of H tail	0.08	-55.8750	0.0000	-0.5000	-4.4700	0.0000	-0.0400
Front spar of H tail	0.04	-52.8750	0.0000	-0.5000	-2.1150	0.0000	-0.0200
Propeller	0.42	5.4375	0.0000	0.0000	2.2838	0.0000	0.0000
Spinner	0.51	5.5993	0.0000	0.0000	2.8556	0.0000	0.0000
Engine	5.76	7.2500	0.0000	0.0000	41.7600	0.0000	0.0000
Servo Battery #1	0.44	-20.5625	0.0000	-0.1875	-9.0475	0.0000	-0.0825
Servo Battery #2	0.44	0.9375	0.0000	-1.2500	0.4125	0.0000	-0.5500
Piccolo Battery #1	0.32	-21.7500	2.3750	0.2188	-6.9600	0.7600	0.0700
Piccolo Battery #2	0.32	-21.7500	-2.3750	0.2188	-6.9600	-0.7600	0.0700
Ingition Battery	0.18	4.3750	0.0000	-0.7500	0.7875	0.0000	-0.1350
Piccolo Unit	1.04	-14.6250	0.0000	0.3750	-15.2100	0.0000	0.3900

Dimension of Components						Components C.M. Location w.r.t. Aircraft C.G. Location		
D_x	D_y	D_z	Length	O.D	Height	X_bar	Y_bar	Z_bar
64.0000	8.0000	10.0000				-3.0604	-0.0836	0.0073
23.0000	41.7000	3.5000				-4.4209	28.6282	0.2155
23.0000	41.7000	3.5000				-4.4209	-28.7954	0.2155
8.2500	17.0000	1.0000				-44.2393	12.9164	-0.9927
8.2500	17.0000	1.0000				-44.2393	-13.0836	-0.9927
			32.7500	1.2500		0.2607	-0.0836	0.7573
			17.3750	0.5000		-44.9893	-0.0836	-0.4927
			7.7500	0.5000		-41.9893	-0.0836	-0.4927
1.0000	26.0000	1.0000		26.0000	1.0000	16.3232	-0.0836	0.0073
				4.0000	4.0000	16.4850	-0.0836	0.0073
9.0000	4.0000	6.5000				18.1357	-0.0836	0.0073
1.6250	2.0000	1.6250				-9.6768	-0.0836	-0.1802
1.6250	2.0000	1.6250				11.8232	-0.0836	-1.2427
4.0000	1.2500	0.8125				-10.8643	2.2914	0.2261
4.0000	1.2500	0.8125				-10.8643	-2.4586	0.2261
1.2500	3.8750	0.6250				15.2607	-0.0836	-0.7427
5.2500	3.8750	2.5000				-3.7393	-0.0836	0.3823

Model Type	Compoments Moment of Inertia w.r.t. Aircraft C.G. Axis (lbs- in^2) Ixx Roll	Iyy Pitch	Izz Yaw
block	149.8638	3935.0019	3902.1979
block	2298.0114	153.9735	2446.9046
block	2262.3421	150.0918	2407.4817
block	119.0317	1217.5894	1335.2959
block	113.8723	1139.0353	1251.6679
cylinder	38.6831	461.4777	38.4657
cylinder	2.0326	186.0934	163.9359
cylinder	0.2102	72.9362	70.7245
block	23.6980	111.9781	135.6060
circular cone	0.6156	139.1049	139.1084
block	28.0005	1953.6507	1941.0906
block	0.2608	41.4095	41.4481
block	0.9260	62.3801	61.7536
block	1.7559	38.2310	39.9189
block	2.0099	38.2310	40.1730
block	0.3316	42.0487	42.1701
block	2.0023	17.6239	18.2388

Total Weight	Aircraft C.G. Location w.r.t. Datum Xcg	Ycg	Zcg
26.84	-10.8857	0.0836	-0.0073
quarter chord location w.r.t. datum	-12.7500		
Xcg w.r.t. quarter chord (+ : ahead / - : behind)	1.8643		

Unit	Aircraft Moment of Inertia w.r.t. Aircraft C.G. Axis Ixx	Iyy	Izz
lbs - in^2	5043.6477	9760.8572	14076.1815
slug - ft^2	1.0886	2.1068	3.0382

Reference : C.G. data measured from Weight and Balance

Configuration	Weight (lbs)	w.r.t. Firewall (in)
gross weight (full fuel)	28.12	10.3
empty weight (without fuel)	27.18	10.4

Appendix B. Dutch Roll Mode Flight Test Data Reduction

Data Reduction of Dutch Roll Mode Flight Test I (TPR Method)

	$Time_{Peak}$ (sec)	$Period_{b/w\ Peak}$ (sec) (e.g. (T_2-T_1) x 2)	$Value_{Peak}$ (deg/sec)	Delta Peak - ΔP (e.g. P_1 - SS)	Peak Ratio (e.g. P_2 / P_1)
$Peak_1$	1081.90	1.10	-43.17	-43.17	0.45
$Peak_2$	1082.45	0.90	19.26	19.26	0.50
$Peak_3$	1082.90	1.20	-9.59	-9.59	0.48
$Peak_4$	1083.50		4.65	4.65	
		Steady State Value	0.00		
	Period $_{avg}$ (sec)	1.07		Peak Ratio $_{avg}$	0.48
	Freq (Hz)	0.94		**Damping Ratio**	**0.22**
	ω_{damp} (rad/sec)	5.89		**ω_n (rad/sec)**	**6.04**

Date Reduction of Dutch Roll Mode Flight Test II (TPR Method)

	$Time_{Peak}$ (sec)	$Period_{b/w\ Peak}$ (sec) (e.g. (T_2-T_1) x 2)	$Value_{Peak}$ (deg/sec)	Delta Peak - ΔP (e.g. P_1 - SS)	Peak Ratio (e.g. P_2 / P_1)
$Peak_1$	1122.10	1.00	53.92	56.92	0.30
$Peak_2$	1122.60	0.90	-20.11	-17.11	0.28
$Peak_3$	1123.05	1.40	1.74	4.74	0.56
$Peak_4$	1123.75		-5.65	-2.65	
		Steady State Value	-3.00		
	Period $_{avg}$ (sec)	1.10		Peak Ratio $_{avg}$	0.38
	Freq (Hz)	0.91		**Damping Ratio**	**0.28**
	ω_{damp} (rad/sec)	5.71		**ω_n (rad/sec)**	**5.95**

Data Reduction of Dutch Roll Mode Flight Test III (TPR Method)

	$Time_{Peak}$ (sec)	$Period_{b/w\ Peak}$ (sec) (e.g. (T_2-T_1) x 2)	$Value_{Peak}$ (deg/sec)	Delta Peak - ΔP (e.g. P_1 - SS)	Peak Ratio (e.g. P_2 / P_1)
$Peak_1$	1129.50	1.30	37.16	37.16	0.33
$Peak_2$	1130.15	1.30	-12.36	-12.36	0.37
$Peak_3$	1130.80		4.52	4.52	
		Steady State Value	0.00		
	Period $_{avg}$ (sec)	1.30		Peak Ratio $_{avg}$	0.35
	Freq (Hz)	0.77		**Damping Ratio**	**0.32**
	ω_{damp} (rad/sec)	4.83		**ω_n (rad/sec)**	**5.10**

Appendix C. Short Period Mode Flight Test Data Reduction

Data Reduction of Short Period Flight Test I (TR Method)

	Pitch Rate (deg/sec)	***Time (sec)***	***Time Increments (Δt)***
Δx	52.62	1211.20	----
0.736Δx	38.728	1211.28	0.08 (Δt_1)
0.406Δx	21.364	1211.34	0.14 (Δt_2)
0.199Δx	10.471	1211.42	0.22 (Δt_3)

	Time Ratio	***ξ***	***$\omega_n\Delta t$***	***ω_n (rad/sec)***
$\Delta t_2 / \Delta t_1$	1.75	0.5	1.0 ($\omega_n\Delta t_1$)	12.50
$\Delta t_3 / \Delta t_1$	2.75	0.9	2.0 ($\omega_n\Delta t_2$)	14.29
$(\Delta t_3 - \Delta t_2) / (\Delta t_2 - \Delta t_1)$	1.33	1.5	3.0 ($\omega_n\Delta t_3$)	13.64
Average	***ξ = 0.97***		***ω_n = 13.47 (rad/sec)***	

Data Reduction of Short Period Flight Test II (TR Method)

	Pitch Rate (deg/sec)	***Time (sec)***	***Time Increments (Δt)***
Δx	46.11	1215.20	----
0.736Δx	33.937	1215.25	0.05 (Δt_1)
0.406Δx	18.721	1215.29	0.09 (Δt_2)
0.199Δx	9.176	1215.37	0.17 (Δt_3)

	Time Ratio	***ξ***	***$\omega_n\Delta t$***	***ω_n (rad/sec)***
$\Delta t_2 / \Delta t_1$	1.8	0.8	1.0 ($\omega_n\Delta t_1$)	20.00
$\Delta t_3 / \Delta t_1$	3.4	1.2	2.0 ($\omega_n\Delta t_2$)	22.22
$(\Delta t_3 - \Delta t_2) / (\Delta t_2 - \Delta t_1)$	2.0	----	3.0 ($\omega_n\Delta t_3$)	17.65
Average	***ξ = 1.0***		***ω_n = 19.96 (rad/sec)***	

Data Reduction of Short Period Flight Test III (TR Method)

	Pitch Rate (deg/sec)	***Time (sec)***	***Time Increments (Δt)***
Δx	52.640	1220.55	----
0.736Δx	38.007	1220.61	0.06 (Δt_1)
0.406Δx	20.966	1220.68	0.13 (Δt_2)
0.199Δx	10.276	1220.74	0.19 (Δt_3)

	Time Ratio	***ξ***	***$\omega_n\Delta t$***	***ω_n (rad/sec)***
$\Delta t_2 / \Delta t_1$	2.17	1.20	1.05 ($\omega_n\Delta t_1$)	17.50
$\Delta t_3 / \Delta t_1$	3.17	1.08	2.05 ($\omega_n\Delta t_2$)	15.77
$(\Delta t_3 - \Delta t_2) / (\Delta t_2 - \Delta t_1)$	0.86	0.82	3.05 ($\omega_n\Delta t_3$)	16.05
Average	***ξ = 1.03***		***ω_n = 16.44 (rad/sec)***	

Appendix D. The Layout of the 6DOF Nonlinear Model in MATLAB/Simulink

Layout for the 6DOF Nonlinear Model

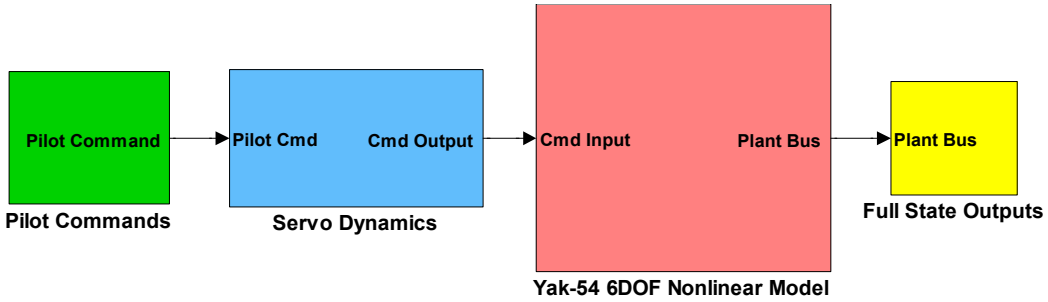

Layout for the Subsystem "Pilot Commands"

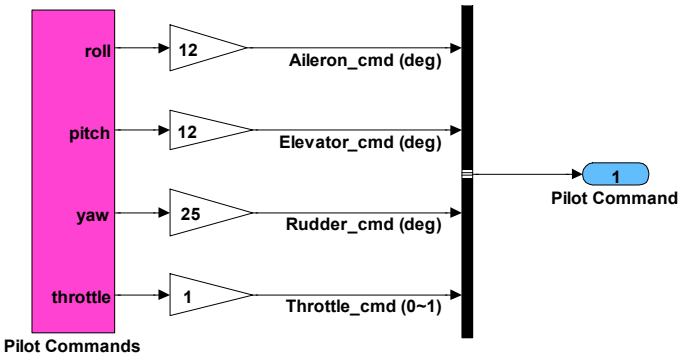

Layout for the Subsystem "Servo Dynamics"

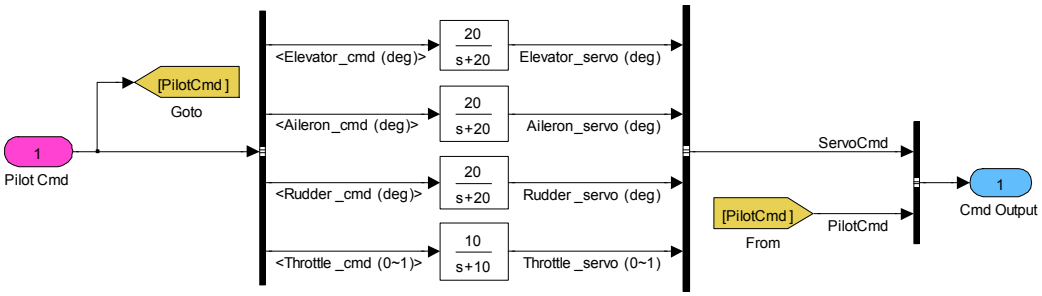

Layout for the Subsystem “Yak-54 6DOF Nonlinear Model”

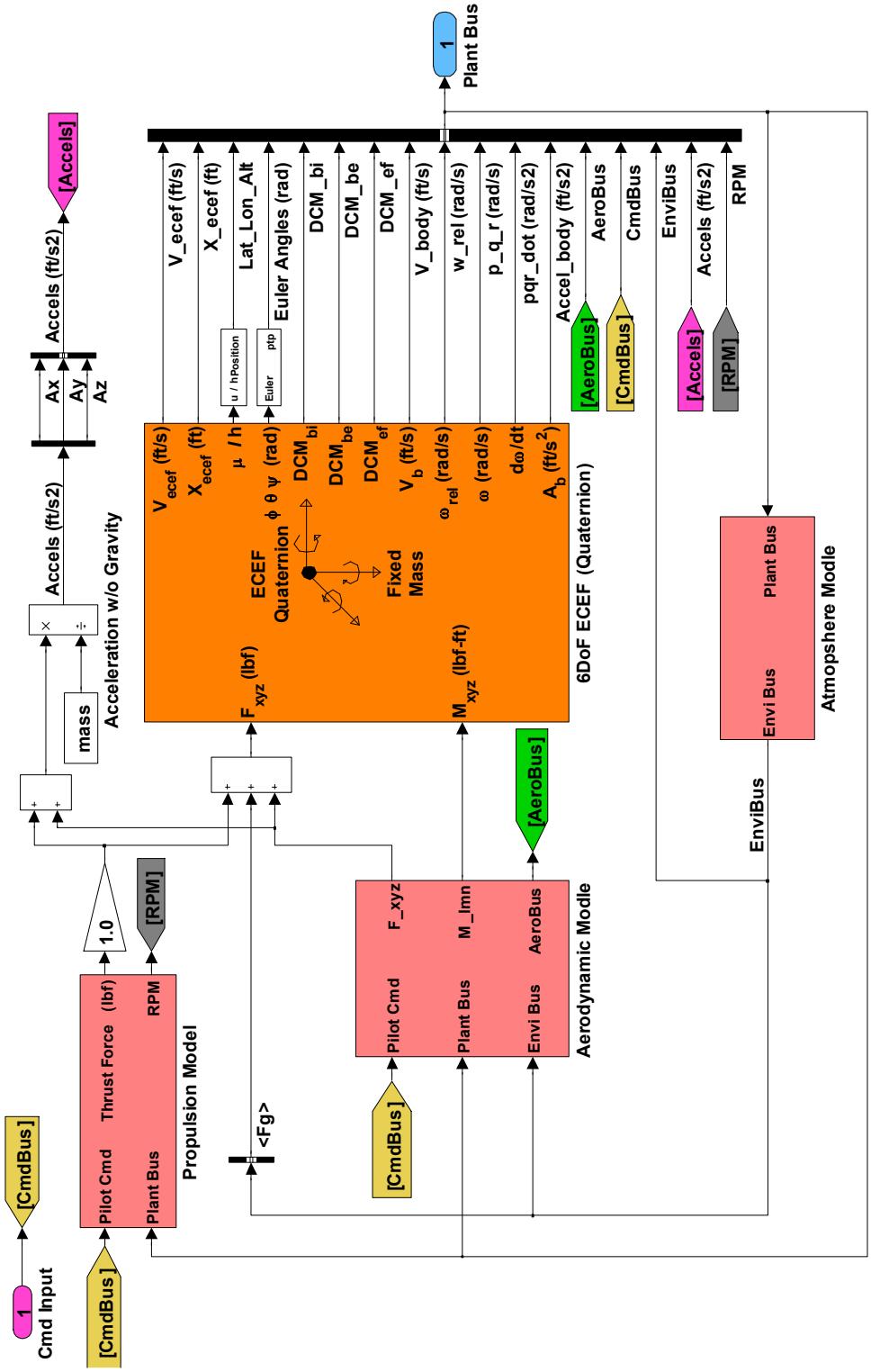

Layout for the Subsystem “Propulsion Model”

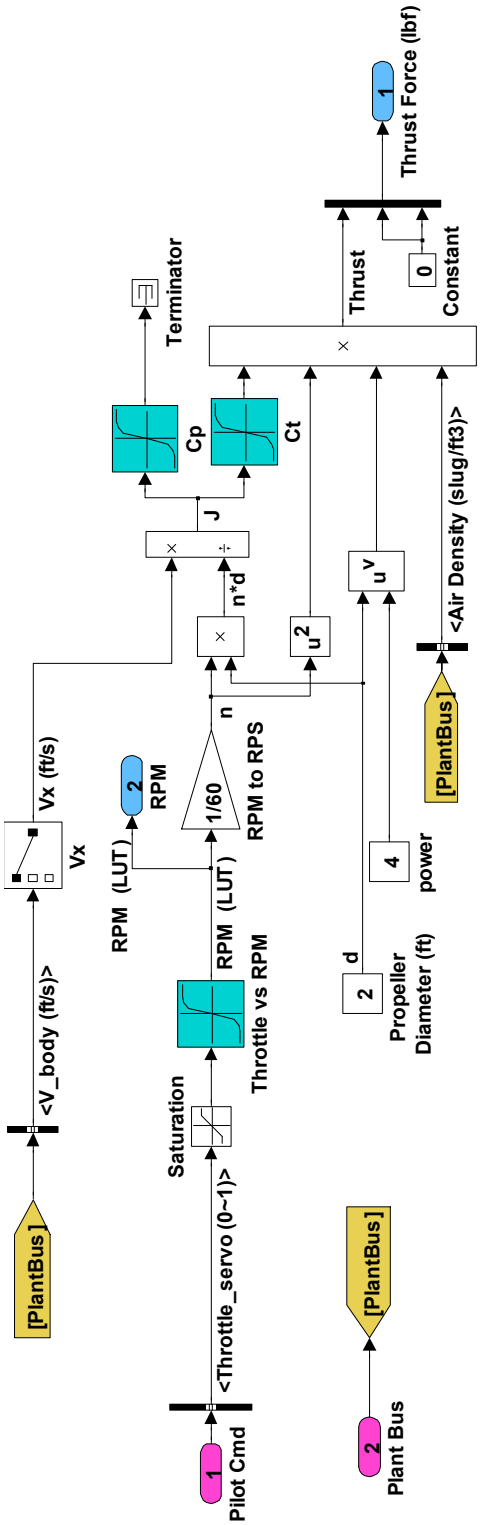

Layout for the Subsystem “Aerodynamic Model”

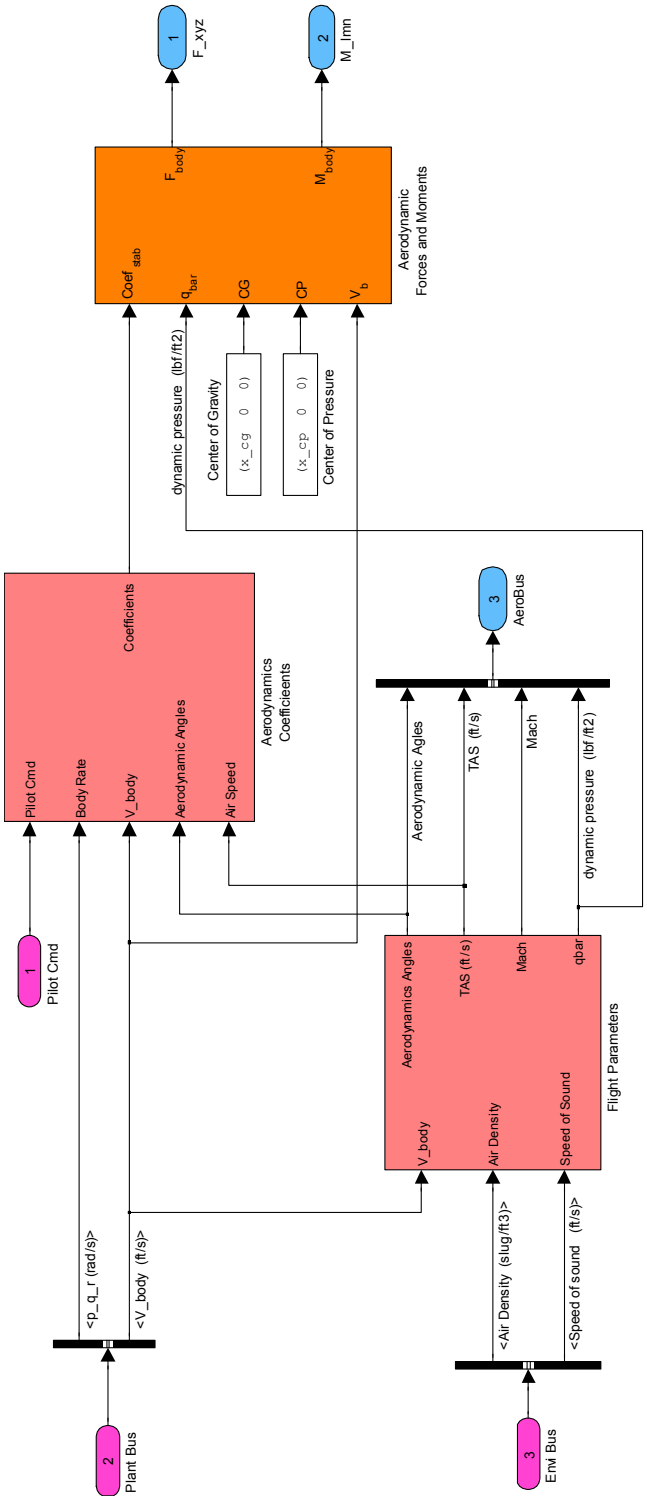

Layout for the Subsystem “Atmosphere Model”

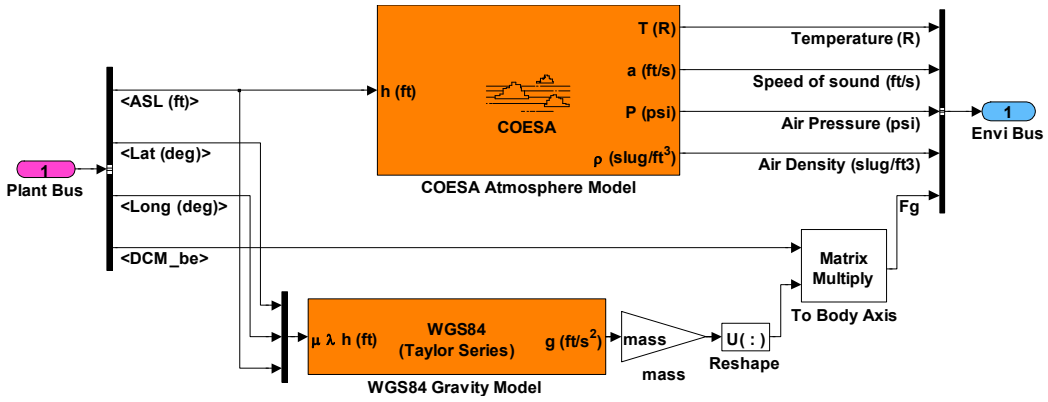

Layout for the Subsystem “Flight Parameters”

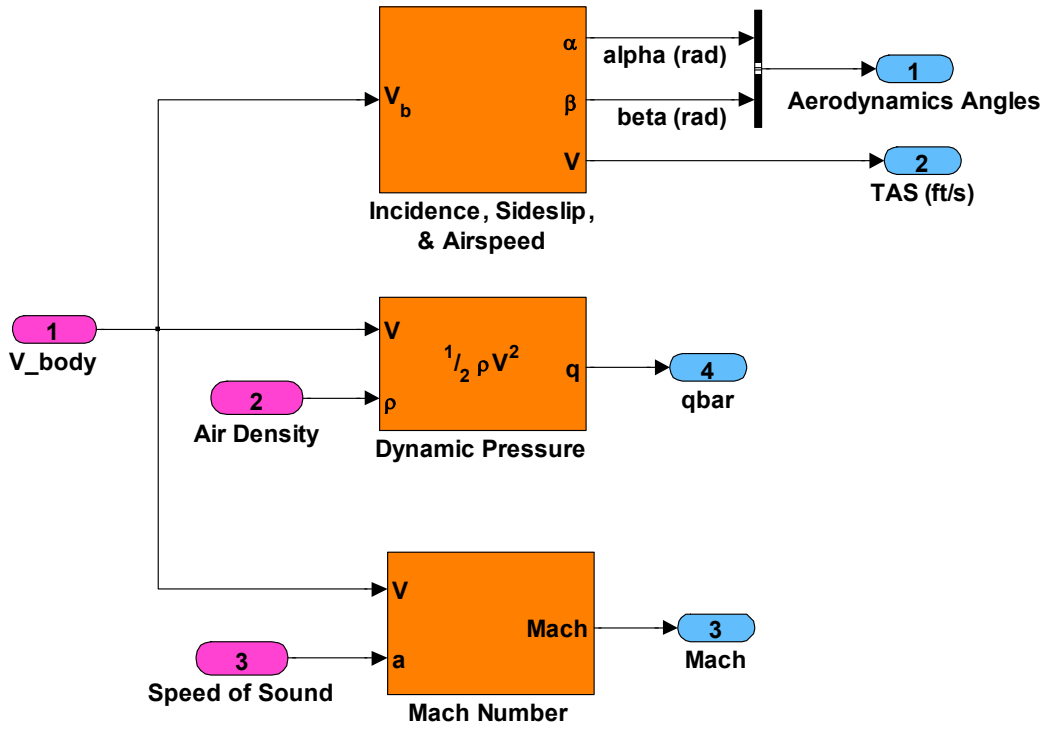

Layout for the Subsystem “Aerodynamics Coefficients”

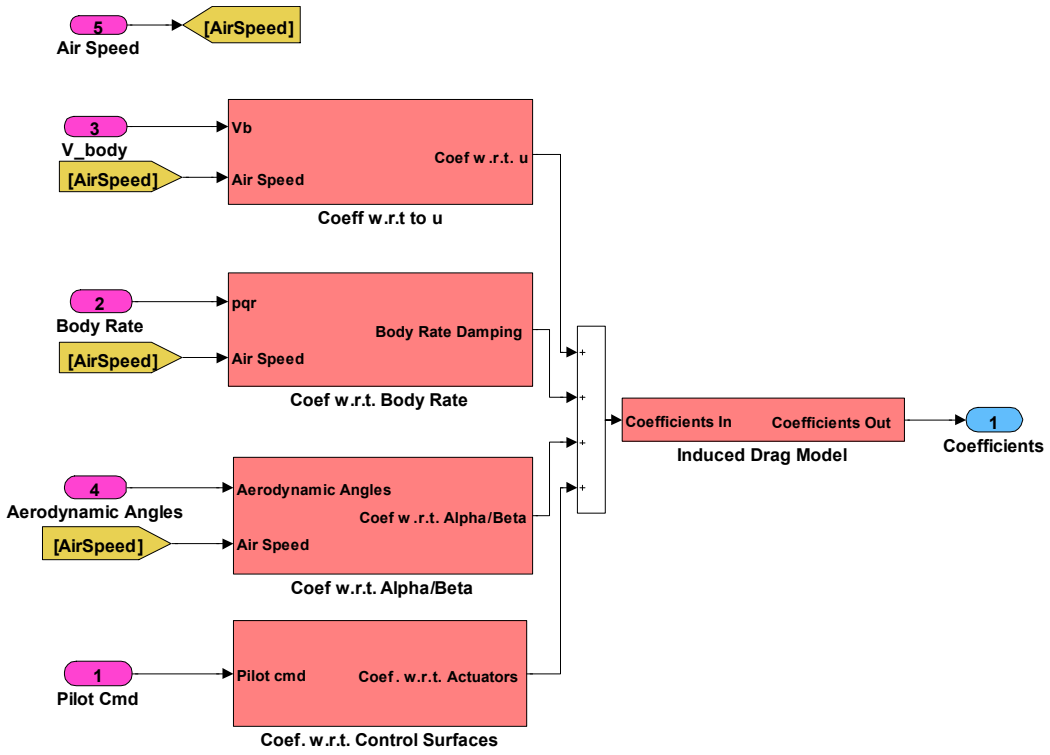

Layout for the Subsystem “Induced Drag Model”

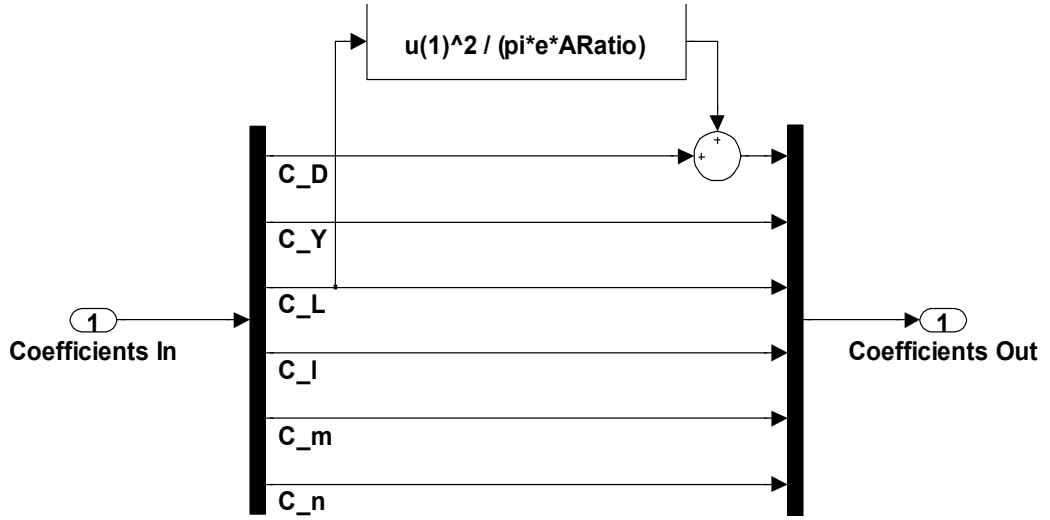

Layout for the Subsystem “Coeff w.r.t. to u”

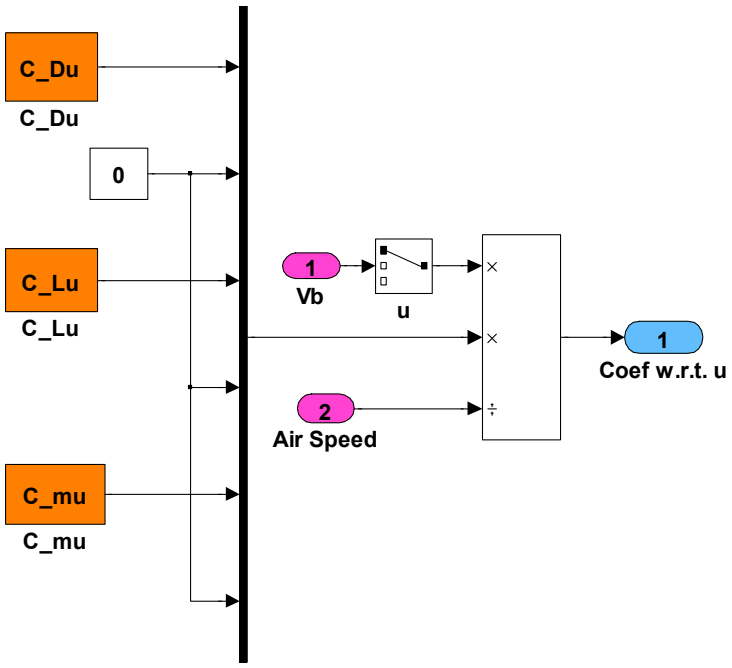

Layout for the Subsystem “Coef w.r.t. Body Rate”

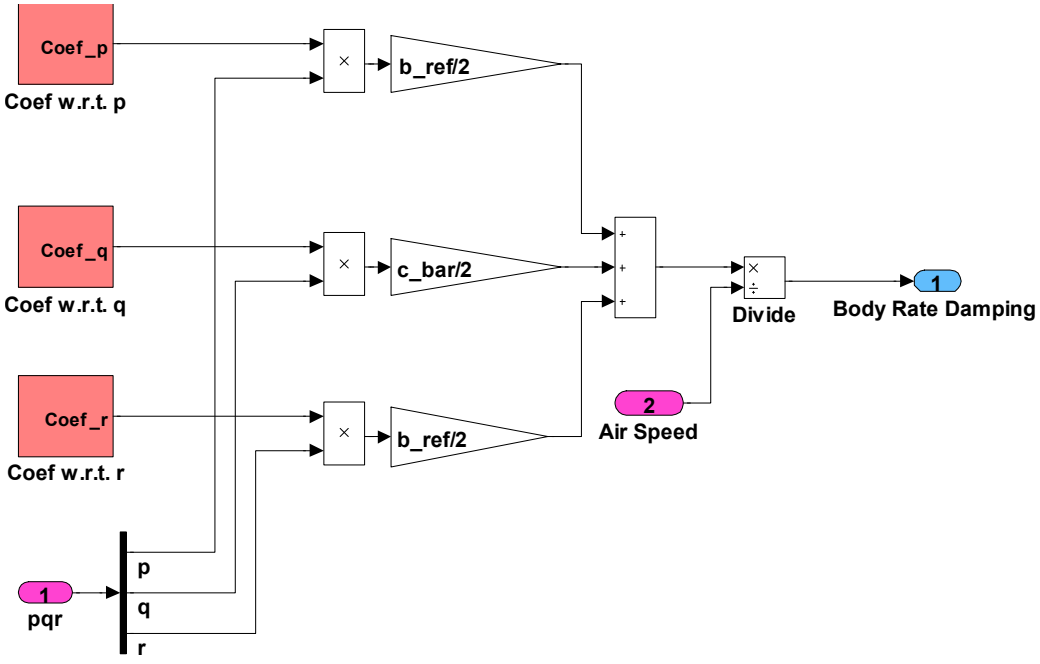

Layout for the Subsystem “Coef w.r.t. p”

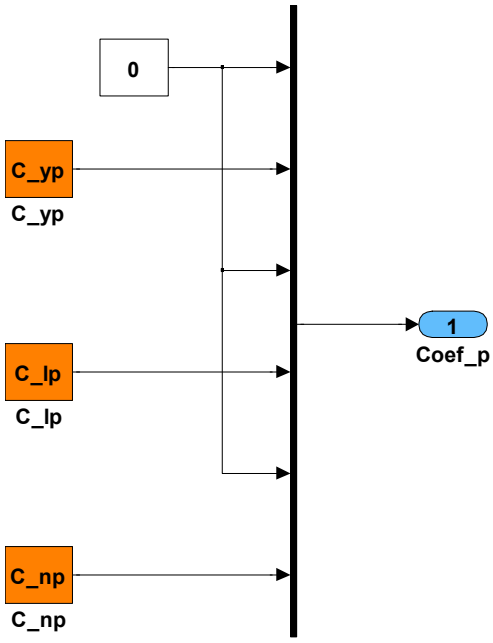

Layout for the Subsystem “Coef w.r.t. q”

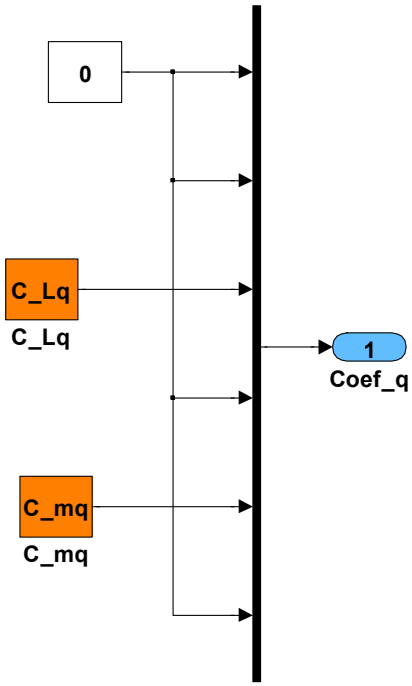

Layout for the Subsystem “Coef w.r.t. r”

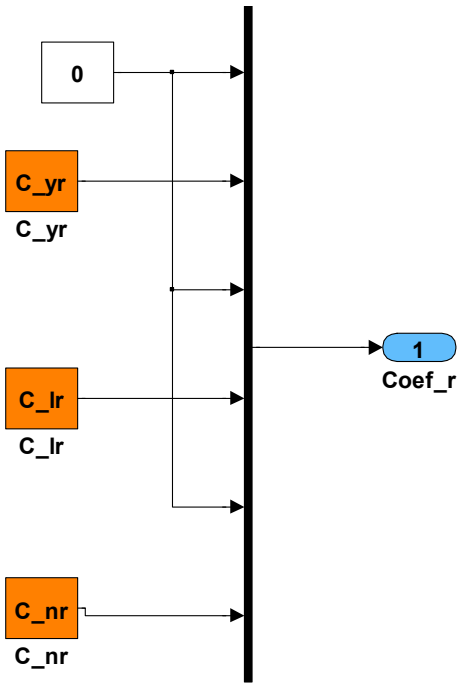

Layout for the Subsystem “Coef w.r.t. Alpha/Beta”

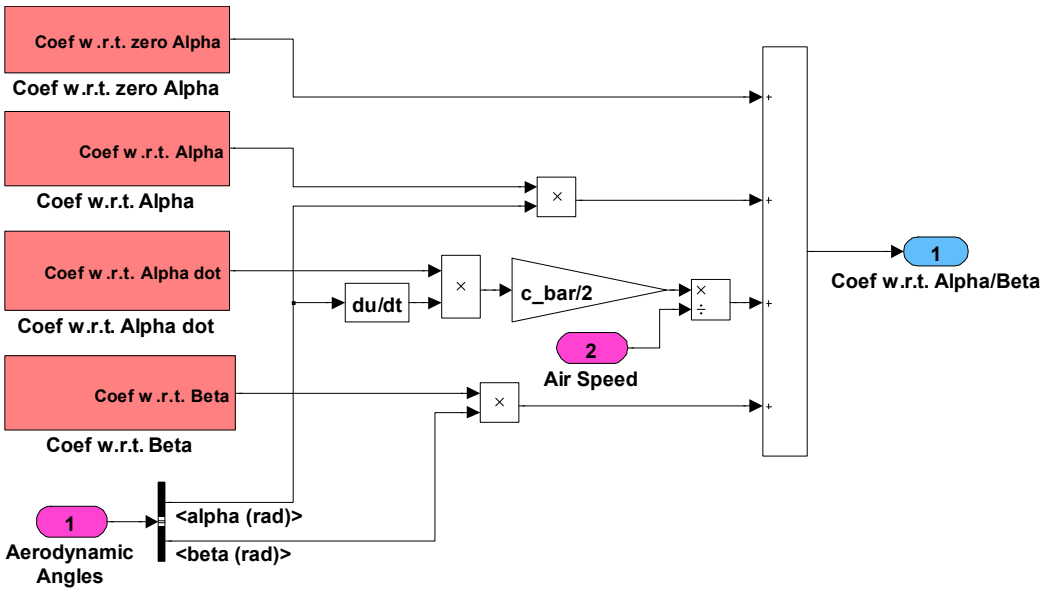

Layout for the Subsystem “Coef w.r.t. zero Alpha”

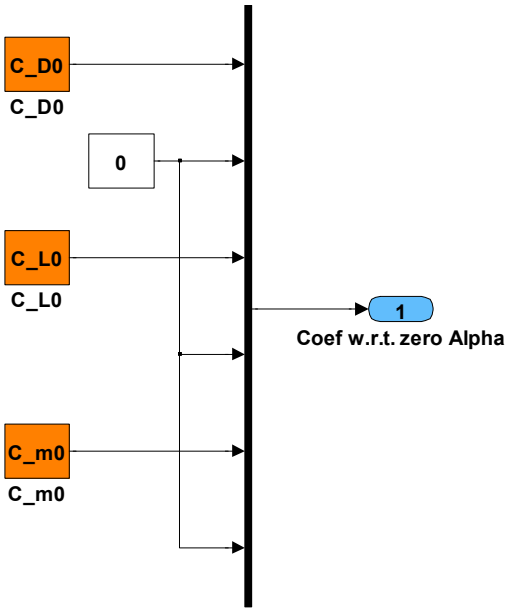

Layout for the Subsystem “Coef w.r.t. Alpha”

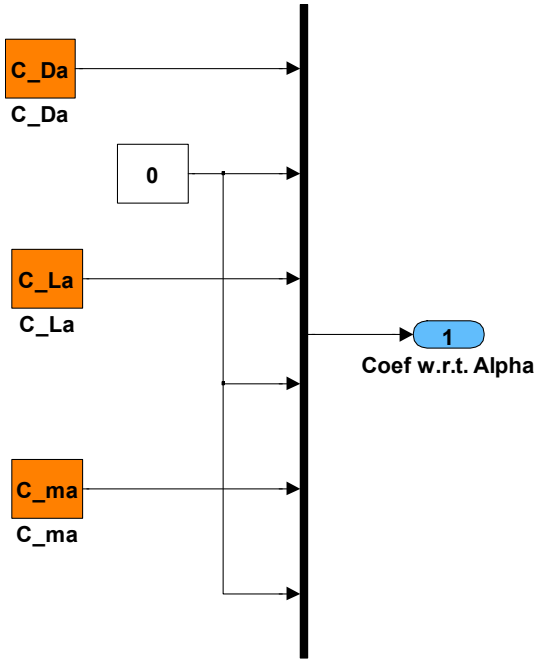

Layout for the Subsystem “Coef w.r.t. Alpha dot”

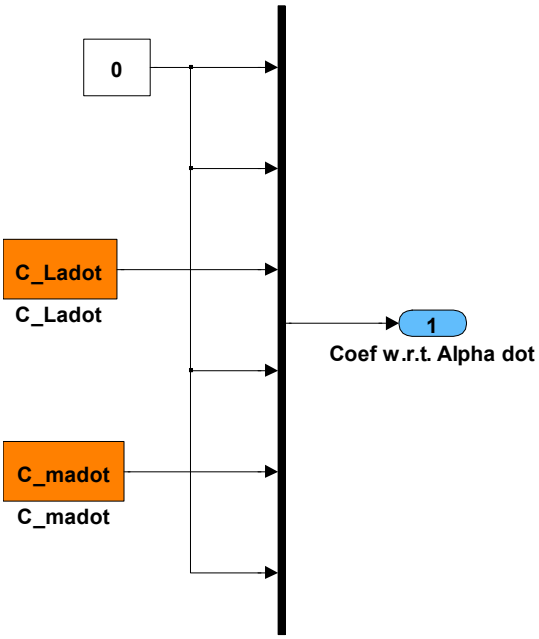

Layout for the Subsystem “Coef w.r.t.Beta”

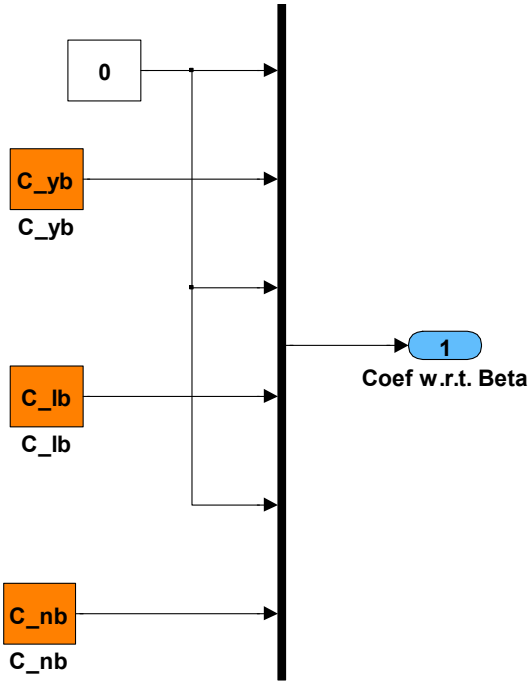

Layout for the Subsystem “Coef w.r.t. Control Surfaces”

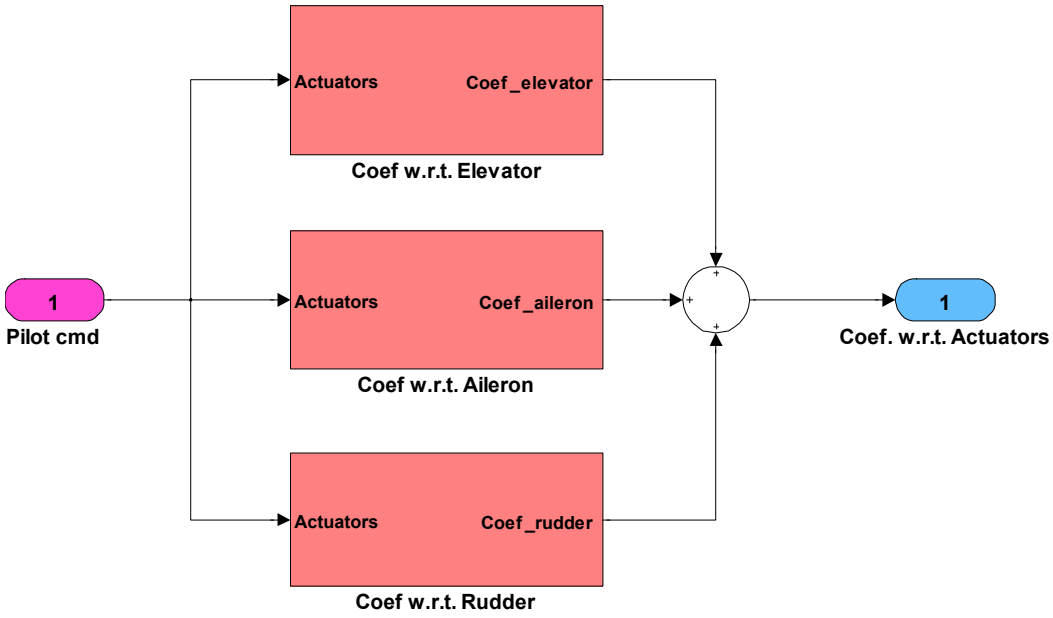

Layout for the Subsystem “Coef w.r.t. Elevator”

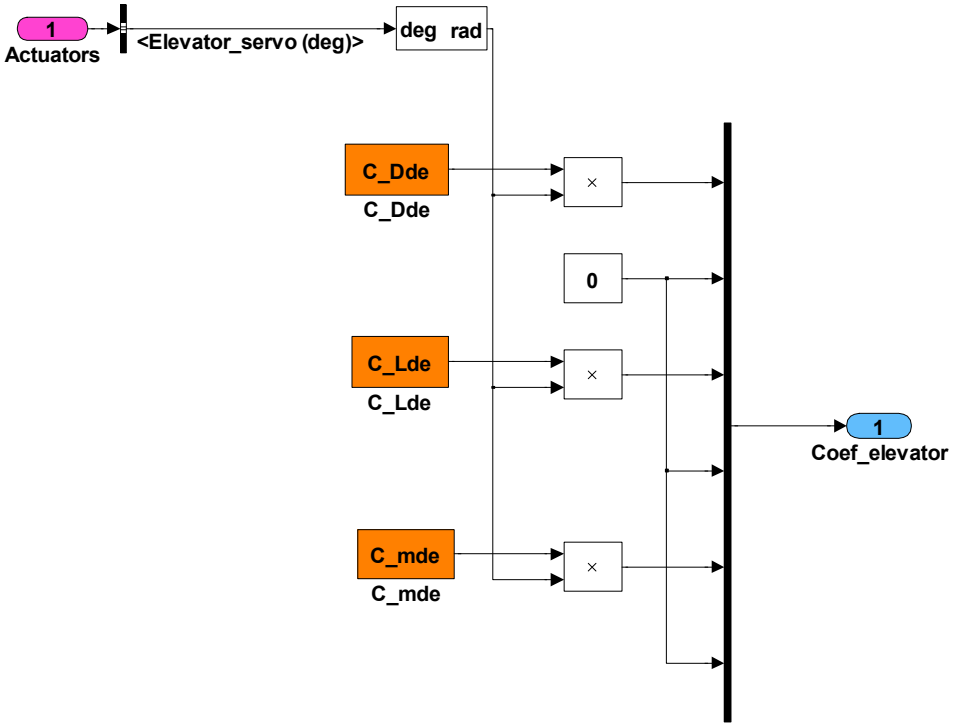

Layout for the Subsystem “Coef w.r.t. Aileron”

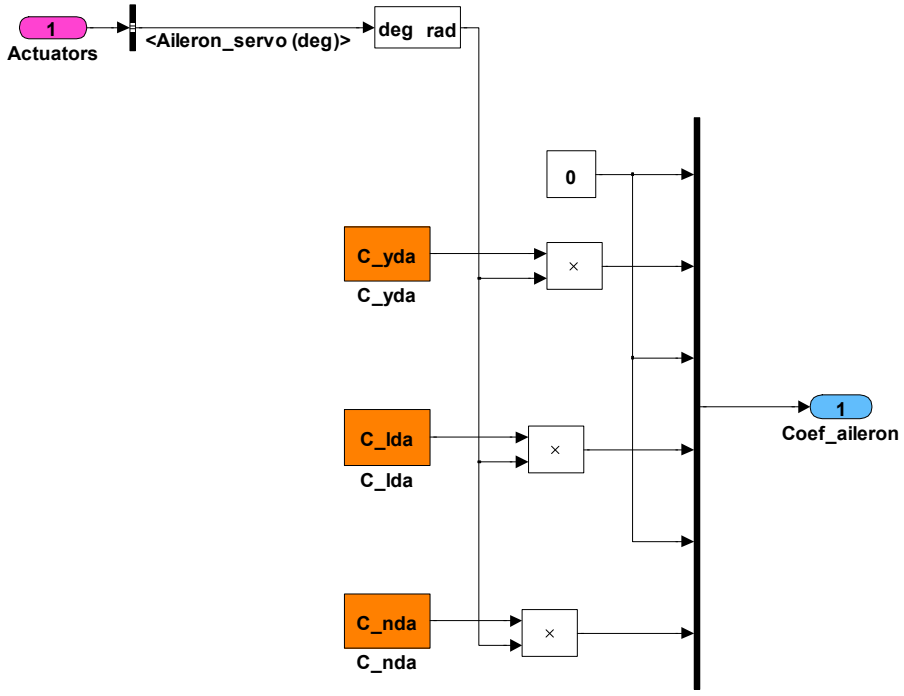

Layout for the Subsystem “Coef w.r.t. Rudder”

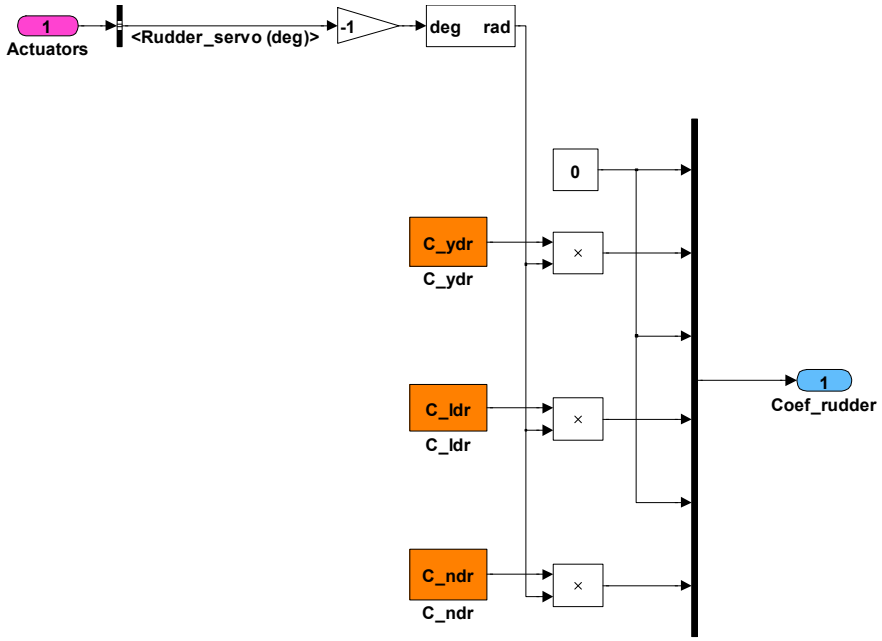

Appendix E. Prediction Accuracy of Stability Derivatives from AAA

Stability Derivative Relative Importance & Prediction Accuracy

Longitudinal			Lateral-Directional		
Derivative	Relative Importance*	Estimated Accuracy	Derivative	Relative Importance*	Estimated Accuracy
C_{L_M}	10	±5%	C_{Y_β}	7	±20%
C_{M_α}	10	±10%	C_{l_β}	10	±20%
C_{D_α}	5	±10%	C_{n_β}	10	±15%
$C_{L_{\dot\alpha}}$	4	±40%	$C_{Y_{\dot\beta}}$	2	±60%
$C_{M_{\dot\alpha}}$	7	±40%	$C_{l_{\dot\beta}}$	2	±60%
$C_{D_{\dot\alpha}}$	1	±50%	$C_{n_{\dot\beta}}$	4	±60%
C_{L_w}	5	±20%	C_{Y_p}	4	±50%
C_{M_w}	8	±20%	C_{l_p}	10	±15%
C_{D_w}	6	±20%	C_{n_p}	8	±90%
C_{L_q}	3	±20%	C_{Y_r}	4	±30%
C_{M_q}	9	±20%	C_{l_r}	7	±40%
C_{D_q}	1	±30%	C_{n_r}	9	±25%

Importance Scale: 10 = major, 5 minor, 0 = negligible

Reference: Roskam, J., *Airplane Flight Dynamics and Automatic Flight Controls - Part I*, Roskam Aviation and Engineering Corporation, Ottawa, KS, 1979.